

ν_μ $\text{CC1}\pi^+$ Events Produced in the T2K Beam at
Super-Kamiokande

by

Sophie Sattell Berkman

B. A., Reed College, 2010

A THESIS SUBMITTED IN PARTIAL FULFILLMENT
OF THE REQUIREMENTS FOR THE DEGREE OF

Doctor of Philosophy

in

THE FACULTY OF GRADUATE AND POSTDOCTORAL
STUDIES

(Physics)

The University of British Columbia
(Vancouver)

April 2018

© Sophie Sattell Berkman, 2018

Abstract

T2K is an experiment designed to make precision measurements of neutrino oscillation parameters. Neutrinos produced in the Japan Proton Accelerator Complex are sent 295 km across Japan to the far detector Super-Kamiokande. Charged current quasi-elastic neutrino interactions in which the neutrino produces a lepton and a nucleon are dominant at T2K beam energies, and these are the signal events used in the measurement of muon disappearance parameters θ_{23} and Δm_{32}^2 . The second most dominant neutrino interaction mode at T2K is the charged current single pion interaction ($\text{CC}1\pi^+$) in which both a lepton and a charged pion are produced in addition to the nucleon. This thesis presents a method to identify charged pions and $\text{CC}1\pi^+$ neutrino interactions at Super-Kamiokande. This is used to develop a selection method for muon neutrino $\text{CC}1\pi^+$ interactions at Super-Kamiokande in the T2K beam. There are 93 events expected based on Monte Carlo predictions which would increase the number of muon neutrino events in the T2K analysis by 40%. Methods developed to evaluate the systematic errors associated with explicitly selecting charged pions at Super-Kamiokande for the first time are also discussed.

Lay Abstract

At the beginning of the universe equal parts matter and anti-matter were created, but if this were the full story nothing in the universe would exist today. It is possible that the pervasive tiny neutral particles called neutrinos could contribute to this discrepancy if neutrinos and anti-neutrinos act differently. The T2K experiment hopes to measure the extent that neutrinos and anti-neutrinos are different. To do this it sends a beam of neutrinos produced in an accelerator from one side of Japan to the other and measures the neutrinos produced in a 50 kTon tank of pure water. Neutrinos can interact in the water in several ways, but until now only the dominant interaction was used in T2K measurements. This thesis presents a method to identify the second most dominant neutrino interaction which is predicted to increase the total number of neutrinos used in the analysis by 40%.

Preface

As the member of two large collaborations, T2K and Super-Kamiokande (SK), the work presented in this thesis is ultimately the culmination of years of effort on behalf of many people.

Chapter 1 summarizes the history, formalism and current state of neutrino oscillation physics, as well as discusses future open questions the field hopes to address. None of the work is original, but the summary is my own.

Chapter 2 describes the T2K experiment. I worked to update the model used to simulate charged pions in the SK detector simulation, mentioned briefly in Section 2.5.5, and described in more detail in [1] [2], and participated in detector calibrations and shifts throughout my time as a PhD student. The summary of the existing methods and literature is my own.

I led the work on the PICCOLO detector described in Chapter 3, including detector design, construction, operation, and analysis. All of the results presented are my own.

Chapter 4 describes the fitQun reconstruction algorithm for SK. The algorithm described in Sections 4.1-4.6 was generally adapted from the MiniBooNE experiment, and coded and developed for SK by Shimpei Tobayama, Michael Wilking, Patrick de Perio and Andrew Missert [3] [4]. The work presented from 4.7 onward describes my implementation of a technique to identify charged pions originally used at MiniBooNE and that I adapted for SK [5]. Although not discussed elsewhere in this thesis, I was the first person to look at the fitQun algorithm on the T2K data in preparation for the addition of a π^0 rejection cut which reduced the background and contributed to the observation of electron neutrino appearance made by the

T2K experiment in 2013 [6] [7].

Chapter 5 describes a selection of ν_μ CC1 π^+ events for T2K at SK. All of the work is my own.

Chapter 6 describes the systematic errors associated with CC1 π^+ events in T2K. The multi-dimensional weights used in 6.1.2 to analyze the correlated differences between the neutrino generator output were calculated by Cris Vilela. The multi-pion and deep inelastic scattering weights used in 6.1.3 were calculated by Christophe Bronner. I applied these weights to the selected CC1 π^+ samples, and otherwise, the work presented in 6.1 on neutrino interactions is my own. The fit to the world pion hadronic interaction data described in 6.2 was done by Elder Pinzon [8]. The method for evaluating the systematic errors associated with pion final state and secondary interactions using fixed hadronic interaction variations was initially developed by Patrick de Perio and myself. The method for evaluating the systematic errors using covariance matrix throws was developed by Elder Pinzon. The work to evaluate the effect of the pion final state and secondary interaction systematic uncertainties on the selected CC1 π^+ samples is my own. The hybrid CC1 π^+ sample was developed by Guang Yang, Shunichi Mine and Thomas Mueller [9].

The conclusions presented in Chapter 7 are my own.

This analysis is blind. There has recently been continued development of the reconstruction algorithm described in Chapter 4 in the context of several SK analyses. These have not yet been applied to T2K. After they are incorporated and new Monte Carlo is generated for T2K this analysis will be unblinded. The exact timescale for this is unknown, but is estimated to be sometime in 2019. Work has been done to ensure that the developments presented in this thesis will be fully integrated into the new framework so that they can be used in the future.

Table of Contents

Abstract	ii
Lay Abstract	iii
Preface	iv
Table of Contents	vi
List of Tables	x
List of Figures	xii
Glossary	xxi
Acknowledgments	xxiv
1 Neutrinos	1
1.1 Standard Model	1
1.2 Neutrinos	2
1.3 Neutrino Oscillations	4
1.3.1 Evidence of Oscillations	4
1.3.2 Formalism	6
1.4 Neutrino Oscillation Measurements	12
1.5 Open Questions	14
2 T2K Experiment	17

2.1	Neutrino Beam	17
2.2	Near Detector	20
2.2.1	INGRID	20
2.2.2	ND280	21
2.3	Super-Kamiokande	25
2.3.1	Detector Design	26
2.3.2	Cherenkov Radiation	28
2.3.3	Calibration	30
2.4	Neutrino Interactions at SK	35
2.4.1	Charged Current Quasi Elastic	35
2.4.2	Charged Current Single Pion	37
2.4.3	Deep Inelastic Scattering	37
2.4.4	Neutral Current Interactions	38
2.5	Simulation	39
2.5.1	Flux Prediction	39
2.5.2	Neutrino Interaction Generators	39
2.5.3	NEUT	40
2.5.4	ND280 Detector Simulation	42
2.5.5	SK Detector Simulation	42
3	PICCOLO	44
4	SK Reconstruction	51
4.1	Likelihood Function	51
4.2	Charge Likelihood	53
4.2.1	Predicted Charge	55
4.2.2	Calculation of Charge Likelihood	61
4.3	Time Likelihood	64
4.3.1	Time Likelihood from Direct Light	65
4.3.2	Time Likelihood from Indirect Light	66
4.4	Sub-Event Algorithm	67
4.4.1	Vertex Pre-Fitter	68
4.4.2	Subevents	68

4.5	One Ring Fits	69
4.5.1	Upstream π^+ Fit	69
4.6	Generic Multi-Ring Fit	71
4.7	Scattered Charged Pion Fit	74
4.7.1	Method	74
4.7.2	Fit Performance	79
4.8	ν_μ CC1 π^+ Reconstruction	90
4.8.1	Performance	97
5	ν_μ CC1π^+ Event Selection	103
5.1	Neutrino Energy Calculation	104
5.2	Visible Event Topologies	106
5.3	Selection Cuts	109
5.3.1	One Ring ν_μ CC1 π^+ Events	110
5.3.2	Multi-Ring ν_μ CC1 π^+ Events	115
5.4	Summary of CC1 π^+ Samples	134
5.5	Background from $\bar{\nu}_\mu$, ν_e and $\bar{\nu}_e$ Interactions	134
5.6	Neutrino Energy Calculation Resolution	135
5.7	Oscillation Variations	140
6	Charged Pion Systematic Error Evaluation	148
6.1	Neutrino Interaction Uncertainties	148
6.1.1	Generator Comparisons of Visible CC1 π^+ Signal	149
6.1.2	Reweighting to Different Signal Models	150
6.1.3	Multi-Pion Variations	156
6.2	Pion Hadronic Interactions	161
6.2.1	Fit to World Data	161
6.3	Pion FSI and SI Cross Section Variations	163
6.3.1	Covariance Matrix Throws	164
6.4	Detector Response Uncertainties	168
6.4.1	Hybrid CC1 π^+ Sample	168
6.5	Systematic Error Summary	169
7	Conclusions	171

Bibliography 174

List of Tables

Table 1.1	Best fit parameters for neutrino oscillations [10].	14
Table 2.1	Cherenkov thresholds for particles in water. Calculated using masses from [10].	28
Table 4.1	Fraction that the μ ring is better matched to the higher or lower energy ring of the two ring pion fit.	94
Table 4.2	Fraction that the μ ring is correctly assigned in the best fit configuration when the likelihood cut is used to select the best fit.	97
Table 5.1	Oscillation parameters used in this section.	110
Table 5.2	One ring μ -like events, after each selection cut	116
Table 5.3	Percent of one ring μ -like events after each selection cut	118
Table 5.4	Number of two ring signal $CC1\pi^+$ events broken up across the possible two ring fit configurations.	120
Table 5.5	Number of two ring events after each selection cut.	122
Table 5.6	Sample purity after each selection cut.	122
Table 5.7	Efficiency of the two ring $CC1\pi^+$ samples relative to the FCFV and the two ring cut.	122
Table 5.8	Number of three ring events after each selection cut	129
Table 5.9	Efficiency of selecting three ring events from the FCFV and the three ring cut.	130
Table 5.10	Percent of sample, 3 ring events, after each selection cut	133
Table 5.11	Number of events in each of the $CC1\pi^+$ samples.	135

Table 5.12	Number of events in each of the $CC1\pi^+$ samples below 1.33 GeV in true neutrino energy.	135
Table 5.13	Background from non- ν_μ beam neutrino interactions.	136
Table 5.14	Mean and standard deviations of the neutrino energy resolution when the Δ formula is used compared to when the $CC1\pi^+$ formula is used to calculate neutrino energy.	137
Table 6.1	Number of events when the total multi-ring signal sample is reweighted in one dimension for each kinematic variable separately.	152
Table 6.2	Variations in the number of events as a result of changing the multi-pion DIS cross section to that of new models.	159
Table 6.3	Variations in the number of events as a result of changing the multi-pion DIS kinematics to that of new models.	161
Table 6.4	Best fit values of for the parameters in the FSI fit.	164
Table 6.5	Fractional RMS of each of the samples from covariance matrix throw variations.	166
Table 6.6	Systematic error summary for sum of multi-ring samples and total $CC1\pi^+$ samples as a fraction of the nominal number of events.	169

List of Figures

Figure 1.1	Kamland result showing neutrino interaction measurements of the neutrino energy spectrum as a function of L_0/E . The ratio of the best fit to the energy spectrum given oscillation, decay and decoherence hypotheses are plotted. The data best match the oscillation hypothesis. Figure from [11].	7
Figure 1.2	Latest Kamland result showing $\bar{\nu}_e$ oscillations. Figure from [12].	13
Figure 1.3	Contours of allowed fit regions for Δm_{32}^2 and $\sin^2 \theta_{23}$. Data from T2K [13], NOvA [14], SK [15], MINOS+ [16], and IceCube [17] are compared. Figure from [15].	13
Figure 1.4	Illustration of the normal mass hierarchy.	15
Figure 2.1	Path that T2K neutrino travels from production to detection. Figure from [18].	17
Figure 2.2	The T2K beamline. Protons enter from the bottom right. They are then sent into the primary beam line which bends them left towards the secondary beam line. Figure from [18].	18
Figure 2.3	An illustration of the probability of ν_μ survival (top), ν_e appearance (middle), and neutrino flux from the T2K beamline as a function of neutrino energy for several off axis angles (bottom). Figure from [6].	20

Figure 2.4	An illustration of the INGRID detector. The beam passes straight through the center of the module at the center of the cross. Figure from [18].	21
Figure 2.5	An illustration of the ND280 detector. The neutrino beam passes from left to right through the center of the detector. Figure from [18].	22
Figure 2.6	An illustration of the SK detector. Figure from [6].	26
Figure 2.7	Simulated Cherenkov rings produced by an electron, muon and charged pion.	29
Figure 2.8	Illustration of the five vertical slices B1-B5 that the SK tank is broken up into to calibrate the properties of the water. The sixth corresponds to the PMTs on the top of the tank. Figure from [19].	33
Figure 2.9	World neutrino interaction cross section data. Figure from [20].	35
Figure 2.10	Feynman diagrams of common neutrino interactions at T2K neutrino energies.	36
Figure 3.1	Momentum distribution of true $CC1\pi^+$ events in the T2K-SK Monte-Carlo.	45
Figure 3.2	The PICCOLO detector.	45
Figure 3.3	Schematic of the PICCOLO detector.	46
Figure 3.4	M11 beam composition at each of a range of momentum settings based on particle time of flight. The time difference between the accelerator and a scintillator in front of the PICCOLO detector is plotted. Because of the way the difference is taken, electrons appear as the peak at the highest times, muons in the middle and pions at the shortest time.	47
Figure 3.5	The muon lifetime as measured in the PICCOLO detector.	48
Figure 3.6	Time that light emission begins for muons in PICCOLO.	48
Figure 3.7	PICCOLO results.	50

Figure 4.1	Charge probability distribution functions $f_q(q; \mu)$ at a variety of predicted charges μ . The data points are the output of the simulation, and the line is the fitted function used to evaluate the likelihood. Diagram from [4].	54
Figure 4.2	Variables used in calculation of predicted charge. The initial particle production is indicated by the white dot, and the point of light emission, s , is indicated by a black dot. Diagram from [4].	56
Figure 4.3	Example charge profiles for electrons (left) and muons (right) as a function of the position at which light is emitted s , and the Cherenkov angle. Figure adapted from [4].	58
Figure 4.4	PMT acceptance output from SKDETSIM. The vertical axis has arbitrary units, and the normalization is set so that $\epsilon(\cos \eta = 1) = 1$. Diagram from [4].	60
Figure 4.5	Variables used to parameterize the six dimensional scattering table for PMTs on the walls of the detector. Diagram is the same for PMTs on the top and bottom of the tank except that R_{PMT} , which is not illustrated, is used instead of z_{PMT} . Diagram from [4].	61
Figure 4.6	Time likelihood from direct light for 450 MeV/ c muons and a range of predicted charge. The data points indicate the raw simulation output and the red curve is the final fit output assuming that the likelihood depends only on the predicted charge and particle momentum. Diagram from [4].	67
Figure 4.7	Pion hadronic scatter.	70
Figure 4.8	Cartoon of the three configurations of the charge likelihood for the upstream pion fit. The blue cones represent the Cherenkov light emitted by each charge likelihood configuration. The red dot indicates the pion scatter point.	72
Figure 4.9	Comparison of muon and pion ranges in water at low energy.	77

Figure 4.10	Vertex resolution for the scattered pion fit. The left column shows the production point and the right column shows the scatter point. All charged pions are shown in this plot.	81
Figure 4.11	Kinematic resolution of scattered pion fitter for the upstream pion track. All charged pions are shown in this plot.	82
Figure 4.12	Kinematic resolution of scattered pion fitter for the downstream pion track. All charged pions are shown in this plot.	83
Figure 4.13	Vertex resolution for the scattered pion fit. The left column shows the production point and the right column shows the scatter point. Charged pions that scatter exactly once are shown in this plot.	84
Figure 4.14	Kinematic resolution of the scattered pion fitter for the upstream pion track. Charged pions that scatter exactly once are shown in this plot.	85
Figure 4.15	Kinematic resolution of the scattered pion fitter for the downstream pion track. Charged pions that scatter exactly once are shown in this plot.	86
Figure 4.16	Vertex resolution for the scattered pion fit on NC1 π^+ events in the T2K-SK MC for all outgoing pions. The left column shows the neutrino interaction vertex and the right column shows the scatter point.	87
Figure 4.17	Kinematic resolution of the scattered pion fitter on NC1 π^+ events in the T2K-SK MC for all outgoing pions.	88
Figure 4.18	Vertex resolution for the scattered pion fit on NC1 π^+ events in the T2K-SK MC with outgoing pions that scatter exactly once. The left column shows the neutrino interaction vertex and the right column shows the scatter point vertex.	89
Figure 4.19	Kinematic resolution of the scattered pion fitter on NC1 π^+ events in the T2K-SK MC with outgoing pions that scatter exactly once.	90

Figure 4.20	Cartoon of the $CC1\pi^+$ hypothesis.	91
Figure 4.21	Pion and muon momentum distributions for samples used to study the $CC1\pi^+$ fitter.	93
Figure 4.22	$CC1\pi^+$ particle gun broken into samples in which the muon is better matched to the higher energy ring from the generic two ring fit (top) and the lower energy ring from the generic two ring fit (bottom). The muon/pion PID is the black line.	95
Figure 4.23	T2K-SK MC broken into samples in which the muon is better matched to the higher energy ring from the generic two ring fit (left row) and the lower energy ring from the generic two ring fit (right row). The top row shows the unoscillated MC and the bottom row shows the oscillated MC. The muon/pion PID is the black line.	96
Figure 4.24	Example event display outputs from the $CC1\pi^+$ fit. The top row is the true PMT hit distribution, the middle row is the seed charge distribution, and the bottom row is the charge distribution after the $CC1\pi^+$ fit is run. The post-fit charge distribution is visibly the same as the true distribution of hit PMTs in both of these events.	98
Figure 4.25	Vertex resolution for the $CC1\pi^+$ fit on the $CC1\pi^+$ particle gun, oscillated and unoscillated T2K-SK MC. The left column shows the neutrino interaction vertex and the right column shows the scatter point vertex.	99
Figure 4.26	Fit resolution of the muon kinematics compared for $CC1\pi^+$ particle gun sample, unoscillated $CC1\pi^+$ events from the T2K-SK MC, and oscillated $CC1\pi^+$ events from the T2K-SK MC.	100
Figure 4.27	Fit resolution of the upstream pion kinematics compared for $CC1\pi^+$ particle gun sample, unoscillated $CC1\pi^+$ events from the T2K-SK MC, and oscillated $CC1\pi^+$ events from the T2K-SK MC.	101

Figure 4.28	Fit resolution of the downstream pion kinematics compared for CC1 π^+ particle gun sample, unoscillated CC1 π^+ events from the T2K-SK MC, and oscillated CC1 π^+ events from the T2K-SK MC.	102
Figure 5.1	Flow chart describing CC1 π^+ event selection.	109
Figure 5.2	Initial quality cuts performed for ν_μ CC1 π^+ selection on the T2K-SK MC as a function of true (left) and reconstructed (right) neutrino energy.	111
Figure 5.3	Number of rings for all events passing the FCFV and minimum energy cuts.	112
Figure 5.4	Cut sequence for preliminary event quality cuts.	112
Figure 5.5	Number of decay electrons for one ring muon-like events.	114
Figure 5.6	Cut sequence for one ring muon-like events after the preliminary quality cuts.	115
Figure 5.7	One ring events after ring counting (a,b) and PID cuts (c,d).	116
Figure 5.8	One ring μ -like events with two decay electrons.	117
Figure 5.9	Ring PID of best multi-ring fit output for two ring events.	119
Figure 5.10	Number of decay electrons for two ring pion-like events.	121
Figure 5.11	Cut sequence for two ring events. The black line indicates the final samples	123
Figure 5.12	Two ring events after ring counting (a, b) and PID cuts (c, d).	124
Figure 5.13	Two ring π^+ -like events with one decay electron.	125
Figure 5.14	Two ring π^+ -like events with two decay electrons.	126
Figure 5.15	Ring PID of best multi-ring fit output for three ring events.	127
Figure 5.16	Number of decay electrons for three ring events.	128
Figure 5.17	Cut sequence for three ring CC1 π^+ events. The black arrow indicates the final samples.	129
Figure 5.18	Three ring events after ring counting (a, b) and PID cuts (c, d).	130
Figure 5.19	Three ring one decay electron π^+ -like events.	131

Figure 5.20	Three ring two decay electron π^+ -like events.	132
Figure 5.21	Energy resolution using Δ formula and CC1 π^+ formula for selected two ring samples.	138
Figure 5.22	Energy resolution using Δ formula and CC1 π^+ formula for selected three ring samples.	139
Figure 5.23	Number of events in the four multi-ring samples as a func- tion of reconstructed neutrino energy. Each plot is at a fixed value of $\sin^2 \theta_{23}$, and illustrates each of the Δm_{32}^2 variations.	142
Figure 5.24	Number of events in all five ν_μ CC1 π^+ samples as a func- tion of reconstructed neutrino energy. Each plot is at a fixed value of $\sin^2 \theta_{23}$, and illustrates each of the Δm_{32}^2 variations.	143
Figure 5.25	Number of events in the multi-ring samples and all sam- ples illustrated in the grid of calculated oscillation param- eters.	144
Figure 5.26	Number of events in the multi-ring samples and all sam- ples illustrated in the grid of calculated oscillation pa- rameters for events with true neutrino energy below 1.33 GeV.	145
Figure 5.27	CC1 π^+ efficiency in the multi-ring samples and all sam- ples illustrated in the grid of calculated oscillation param- eters.	146
Figure 5.28	CC1 π^+ efficiency in the multi-ring samples and all sam- ples illustrated in the grid of calculated oscillation pa- rameters for events with true neutrino energy below 1.33 GeV.	147
Figure 6.1	Comparisons between different generators in muon and pion kinematics for signal events with one muon and one pion.	151

Figure 6.2	Ratio of different generators in muon and pion kinematics for signal events with one muon and one pion to the default NEUT. NEUT is black, Genie default is pink, Genie alternate is red and NUWRO is blue.	153
Figure 6.3	Sum of true signal events in the four multi-ring samples varied to match the kinematics of other neutrino interaction generators. NEUT is black, NUWRO is blue, Genie Default is red and Genie Alternate is pink.	154
Figure 6.4	Sum of true signal events in the total $CC1\pi^+$ sample varied to match the kinematics of other neutrino interaction generators. NEUT is black, NUWRO is blue, Genie default is red and Genie alternate is pink.	155
Figure 6.5	Error from neutrino interaction variations.	156
Figure 6.6	Weights applied to total multipion cross section. M0 is red, M1 is black and M2 is blue [21]. The plot is zoomed in so that the differences between M0 and M2 are visible.	158
Figure 6.7	Variations in $CC1\pi^+$ samples when the different multipion cross section models are applied.	158
Figure 6.8	Weights applied to leading pion momentum and invariant hadronic mass for M0 [21].	160
Figure 6.9	Variations in $CC1\pi^+$ samples when the different multipion models are applied.	160
Figure 6.10	Comparison of FSI fit results to π^+ -C external cross section measurements as a function of pion momentum. FSI fit best fit is indicated by the black line, and the 1σ error band is indicated in red. The dashed line and the blue error band are the result of an earlier fit to the external pion cross section data. Figure from [22].	163
Figure 6.11	Covariance matrix between the parameters in the FSI fit. Figure from [22].	164
Figure 6.12	Visualization of 1000 covariance matrix throw variations of FSI and SI parameters.	166
Figure 6.13	Error from FSI and SI covariance matrix throws.	167

Figure 6.14 Relation between the five $CC1\pi^+$ samples in terms of the
FSI and SI variations. 167

Glossary

CC1 π^+ Charged current single charged pion neutrino interaction

CCOther Other charged current neutrino interactions

CCQE Charged current quasi-elastic neutrino interaction

CMB Cosmic microwave background

CP Charge-parity

CSDA Continuous slowing down approximation for particle range calculation

CX Charge exchange

Δ Delta baryon

DIS Deep inelastic scattering neutrino interaction

ECAL Electromagnetic calorimeter

FC Fully contained

FCFV Fully contained within the Super-Kamiokande fiducial volume

FGD Fine grained scintillating detectors

fiTQun Maximum likelihood reconstruction algorithm used at Super-Kamiokande

FSI Final state interactions pions undergo in a nucleus

INGRID Interactive Neutrino GRID

J-PARC Japan Proton Accelerator Research Complex

LINAC Linear accelerator

MC Monte-Carlo

MPPC Multi-pixel photon counter

MR sum Multi-ring sum. Sum of two and three ring CC1 π^+ events.

NC Neutral current neutrino interaction

NC1 π^+ Neutral current single charged pion neutrino interaction

NC1 π^0 Neutral current single neutral pion neutrino interaction

ND280 T2K off axis near detector located 280 m from the target

NEUT Neutrino interaction generator used by the T2K experiment

ot Over Cherenkov threshold

P0D Neutral pion (π^0) Detector

PDG Particle Data Group

p.e. Photo-electrons

PICCOLO Pion Integrating Cylinder for Cherenkov Optics and Light Observation

PID Particle identification

PMT Photo-multiplier tube

POT Protons on target

RMS Root mean squared

SI Secondary interactions pions undergo in a detector

SK Super-Kamiokande

SKDETSIM SK Detector Simulation

SMRD Side muon range detector

sub-GeV Below 1.33 GeV in true neutrino energy

T2K Tokai to Kamioka

T2K-SK MC Simulated neutrino interactions with the T2K beam flux at the SK detector

TPC Time projection chamber

ut Under Cherenkov threshold

1R+2de One ring $CC1\pi^+$ events with two decay electrons

2R+1de Two ring $CC1\pi^+$ events with one decay electron

2R+2de Two ring $CC1\pi^+$ events with two decay electrons

3R+1de Three ring $CC1\pi^+$ events with one decay electron

3R+2de Three ring $CC1\pi^+$ events with two decay electrons

Acknowledgments

I am grateful to the many people who have made this work possible.

As a supervisor, Hiro Tanaka has been an extraordinary example of what it means to be a scientist. I have always appreciated his insights as well as his careful and deliberate approach to problem solving. He has given me incredible opportunities and independence.

Mike Wilking has been an amazing source of information and encouragement. I am appreciative that he was always willing to talk about pions with me.

Akira Konaka has an infectious joy about physics and it has been a pleasure to get to share many productive discussions with him.

Kendall Mahn has always made the time to talk with me about physics and otherwise. I was lucky to get to sit across the trailer from her.

Thanks to Christophe Bronner for his help with the deep inelastic scattering uncertainties and to Cris Vilela for his help with the neutrino interaction uncertainties.

The SKanada group was a special place to work thanks to: Eric Zimmerman, John Martin, Andy Missert, Shimpei Tobayama, Corina Nantais, Xiaoyue Li, Patrick de Perio, Roman Tacik, and Trevor Towstego.

I have also been fortunate to work within the T2K-Canada group and I would like to thank everyone who has been a part of it, in particular: Sampa Bhadra, Scott Oser, Thomas Lindner, Tom Feusels, Elder Pinzon, Mark Scott, Khalid Gameil, Jiae Kim, John Walker and Christine Nielsen.

The T2K and Super-Kamiokande collaborations have given me many extraordinary colleagues, and I am glad to have had the opportunity to work

with all of them. Thanks in particular to Roger Wendell, Okumura-san and Hayato-san for their many useful comments over the years.

Thanks to my PhD committee who have all been incredibly helpful and supportive: Janis McKenna, John Behr, and David Morrissey.

Thank you to my friends who have kept me grounded and stuck by me, no matter which continent I happened to be on.

And finally, thank you to my family, for your love, support, and everything else.

Chapter 1

Neutrinos

What are we made of, and why? Particle physics is one of the ways that we address these fundamental questions. We know that the universe is made of matter, as described by the standard model of particle physics, as well as dark matter and dark energy. The nature of dark matter and dark energy is currently unknown. This chapter will introduce neutrinos and their place in particle physics, give a brief overview of the history of neutrino measurements, describe the current understanding of the field today, and finally mention the open questions that still need to be addressed.

1.1 Standard Model

The Standard Model of particle physics describes the known matter in the universe and what we currently believe to be its fundamental building blocks. There are two categories of particle in the Standard Model: bosons with integer spins and fermions with half integer spins.

The vector bosons with spin 1 mediate the forces of nature. The electromagnetic force is mediated by the photon. The strong force is mediated by gluons. The weak force is mediated by the W^\pm and the Z^0 . The Higgs boson is a spin 0 particle that mediates the mechanism that gives the other particles mass.

The fermions contain three generations and are separated into two cat-

egories: quarks, which interact strongly, and leptons which do not. The quarks are fractionally charged and not observed freely. The strong force gluons bind them into mesons like pions, which are made of quark-antiquark pairs, or baryons like protons and neutrons, which are made up of three quarks. Only the up and down quarks are prevalent in ordinary matter; the other quarks are made, for example, in colliders.

Leptons only interact electromagnetically or through the weak interaction. The charged leptons are electrons, muons and taus. Each charged lepton has a corresponding neutrino (ν_e, ν_μ, ν_τ), which are neutral massless leptons. The neutrinos are related to the charged leptons by their flavor, as indicated by the subscript above. In charged current interactions neutrinos are produced in a given flavor state. For example, in the decay of a positively charged pion decay, an anti-muon and muon neutrino are produced. Neutrinos can be produced in many ways: in the sun, the atmosphere, reactors, and supernovas among others. It is now known that while neutrinos have masses that are much smaller than those of the other standard model particles, they are not massless as was formerly assumed [23]. Neutrinos will be discussed in more detail in the following section.

For the most part the Standard Model agrees incredibly well with experimental measurements, however there are several missing pieces. In particular the standard model does not include gravity, or describe neutrinos correctly. It also neglects dark matter and dark energy.

1.2 Neutrinos

Neutrinos were initially postulated by Pauli to solve the problem that energy was apparently not conserved in beta decay measurements.

As understood at the time, beta decay occurred when a nucleus decayed to produce a lighter nucleus and an electron. As this is a two body decay, using conservation of energy and momentum it is possible to calculate the energy of the electron based on the masses of the three particles. This means that because the masses are constant, beta decay was expected to produce mono-energetic electrons. In 1918 Chadwick measured the energy

of outgoing electrons produced by beta nuclear decays and instead observed a spectrum of electron energies [24]. To explain these results some suggested that perhaps energy was not conserved.

In 1930 Pauli wrote a letter addressed to his colleagues attending a conference in which he suggested that a third particle might also be produced in beta decay. This would make it possible to maintain conservation of energy in light of the experimental measurements of the electron energy spectrum [25]. Based on this proposal Fermi reformulated beta decay as:

$$n \rightarrow p + e^- + \bar{\nu}_e, \quad (1.1)$$

in which both the neutron and proton remain bound within the nucleus [26].

Neutrinos were first detected in 1956 by Reines and Cowan using a source of reactor neutrinos from the Savannah River reactor. They placed a 400 L liquid scintillator detector comprised of water doped with 40 kg of CdCl₂ nearby. It was instrumented with phototubes to observe the scintillation light produced. They detected the reactor electron anti-neutrinos using the inverse beta decay signal:

$$\bar{\nu}_e + p \rightarrow e^+ + n. \quad (1.2)$$

The CdCl₂ made it possible to observe a delayed coincidence signal between the positron and a photon produced by neutron capture on cadmium [27].

The muon neutrino was discovered by Lederman *et al.* in 1962. They used a proton accelerator to produce pions, and looked at the beam of neutrinos produced when those pions decayed. Charged pions decay to produce a muon and a muon neutrino. This is similar to the neutrino beam technique used in modern experiments such as T2K, and which will be discussed in more detail in Chapter 2. At the end of the beam they placed a detector that could distinguish electrons and muons, and as they saw muons instead of electrons in their detector they could determine that the neutrinos observed were different than those that Reines and Cowan had seen [28].

The tau neutrino was discovered in 2000 by the DONUT collaboration.

They used the Fermilab Tevatron to produce D_s mesons and looked for them to decay into a τ and ν_τ with a detector that could separately detect electron, muon, and tau leptons. With this detector they could identify the τ leptons produced by ν_τ charged current interactions [29].

1.3 Neutrino Oscillations

As neutrinos travel over a distance they “oscillate”, or change flavor. This means that a beam of neutrinos that begins as one flavor can be detected with a different composition when observed at a distance L away from production. This can result in observing fewer of the initial flavor of neutrinos than expected, which is called “disappearance”, or detecting neutrinos of additional flavors than were initially produced, which is called “appearance”.

1.3.1 Evidence of Oscillations

This section describes the evidence for neutrino oscillations.

Solar Neutrinos

The first indications for neutrino oscillations came from solar neutrino measurements. Neutrinos are produced through fusion reactions in the sun. Solar models give a precise prediction of the neutrino flux from the sun based on the relative frequency of these fusion reactions, and experiments set out to measure these.

The first experiment to measure solar neutrinos was the Homestake experiment performed by Ray Davis in 1968. This detector was made of a 390 kL tank of C_2Cl_4 and located 1.5 km underground. It measured neutrino capture on the chlorine:



To measure the neutrino interactions the number of argon atoms in the chlorine were counted. The overall rate of solar neutrinos was found to be about 30% that of the expected flux [30].

Discrepancies between the number of expected and measured neutrinos were also observed in the GALLEX and Sage experiments which looked for neutrino capture on gallium, as well as in the Kamiokande water Cherenkov experiment [31] [32] [33] [34].

The SNO experiment ultimately solved the solar neutrino problem. SNO was a 1 kTon Cherenkov experiment filled with heavy water. It could detect three types of neutrino interactions from solar neutrinos:

$$\text{Charged Current : } \quad \nu_e + d \rightarrow p + p + e^- \quad (1.4)$$

$$\text{Neutral Current : } \quad \nu_x + d \rightarrow p + n + \nu_x \quad (1.5)$$

$$\text{Elastic Scattering : } \quad \nu_x + e^- \rightarrow \nu_x + e^-. \quad (1.6)$$

The neutral current and elastic scattering interactions are both sensitive to all flavors of neutrinos. The charged current interactions are only sensitive to electron neutrinos because any ν_μ or ν_τ would not be high enough energy to produce the corresponding μ or τ .

By looking at the neutral current and elastic scattering channels it was possible for the SNO experiment to measure the total neutrino flux of solar neutrinos, independent of neutrino flavor. These measurements were found to agree with the solar models. Then, using the charged current channel it was possible for them to measure the ratio of the electron neutrino flux to the total solar flux. This was found to be smaller than the total flux, which indicated that neutrinos were oscillating as they travelled from the sun [35].

Atmospheric Neutrinos

Neutrino oscillations were first observed in atmospheric neutrinos by the Super-Kamiokande (SK) experiment. Neutrinos are produced in the Earth's atmosphere when the charged pions and muons that are created by high energy protons decay. Muon neutrinos are produced by pion and muon decays and electron neutrinos are produced by muon decays. SK is a 50 kTon water Cherenkov detector, which has good particle direction resolution and electron/muon particle identification which means that they are sensitive

to ν_e and ν_μ charged current interactions. The detector is described in more detail in Chapter 2. SK measured atmospheric neutrino oscillations by separating the atmospheric neutrinos that they observed into upward going and downward going electron-like and muon-like samples. The upward going sample consisted of neutrinos that were produced in the atmosphere on the other side of the earth and had traveled approximately 13,000 km to reach the detector. The downward going neutrinos were produced in the atmosphere above the detector at an average distance of approximately 15 km. The SK collaboration found that there were fewer upward going muon neutrinos than downward going, which indicated that the muon neutrinos that had travelled through the Earth had disappeared. Only the muon neutrinos were affected, and a relative surplus of electron neutrinos was not observed, which suggested that muon neutrinos were changing into tau neutrinos as they travelled through the Earth [36].

Reactor Neutrinos

One of the clearest pictures of neutrino oscillations comes from the Kamland experiment in 2005. This experiment measured the reactor anti-neutrinos produced by 53 nuclear reactors at varying distances from the detector. The data were compared to the hypotheses of neutrino oscillation, neutrino decay and neutrino decoherence, each of which have a different dependence on the ratio of production distance to neutrino energy. The neutrino oscillation dependence on the L/E ratio will be discussed more explicitly in the following section on oscillation formalism. As illustrated in Fig. 1.1 the data best fit the neutrino oscillation hypothesis, with the oscillatory behavior directly observed [11].

1.3.2 Formalism

This section describes the formalism of neutrino oscillations, which come about because the flavor states that undergo weak interactions are linear combinations of the neutrino mass states.

The three neutrinos can be described in one of two ways, either as definite

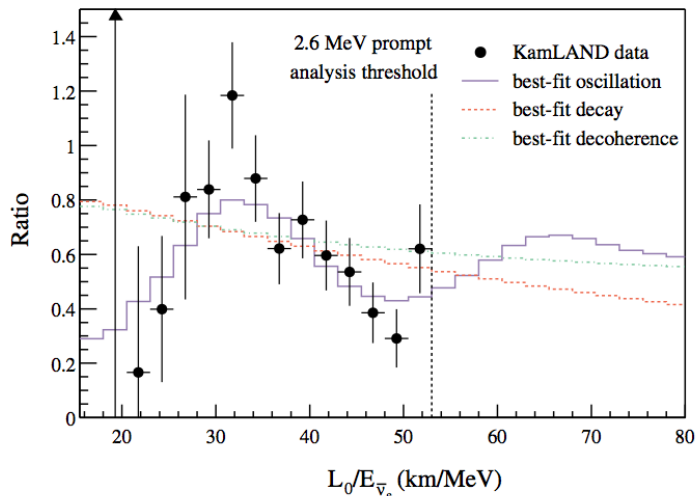


Figure 1.1: Kamland result showing neutrino interaction measurements of the neutrino energy spectrum as a function of L_0/E . The ratio of the best fit to the energy spectrum given oscillation, decay and decoherence hypotheses are plotted. The data best match the oscillation hypothesis. Figure from [11].

mass states, called $|\nu_i\rangle$ where $i = 1, 2, 3$, or as definite flavor states $|\nu_f\rangle$ where $f = e, \mu, \tau$. Both the flavor and mass states can be written as a superposition of the other, and they are related by a unitary matrix U . The flavor states are written in terms of the mass states as:

$$|\nu_f\rangle = \sum_i U_{fi}^* |\nu_i\rangle \quad (1.7)$$

As a neutrino that begins in a definite flavor state propagates the mass states will interfere so that the neutrino is in a mixed flavor state. When the mixed neutrino flavor state is measured it is forced to be in a definite flavor state. These transitions from definite flavor state to mixed flavor states are called neutrino oscillations. The probability of one neutrino of flavor f created at $(x, t) = (0, 0)$ will be measured as another flavor g at (x, t) can

be calculated as:

$$\mathcal{P}(\nu_f \rightarrow \nu_g) = |\langle \nu_g | \nu_f(x, t) \rangle|^2. \quad (1.8)$$

Here it is assumed that $\hbar = c = 1$.

The flavor states in Eq. 1.7 evolve in time according to the Schrodinger equation:

$$|\nu_f(x, t)\rangle = \sum_i U_{fi}^* e^{-i(E_i t - p_i x)} |\nu_i\rangle. \quad (1.9)$$

This means that the probability can be written as:

$$\begin{aligned} \mathcal{P}(\nu_f \rightarrow \nu_g) &= \left| \sum_i \sum_j \langle \nu_j | U_{gj} U_{fi}^* e^{-i(E_i t - p_i x)} |\nu_f\rangle \right|^2 \\ &= \left| \sum_i U_{gi} U_{fi}^* e^{-i(E_i t - p_i x)} \right|^2 \\ &= \sum_i \sum_j U_{gi} U_{fi}^* U_{gj}^* U_{fj} e^{-i((E_i - E_j)t - (p_i - p_j)x)}. \end{aligned} \quad (1.10)$$

The momentum of the i th mass state p_i can be calculated in terms of the neutrino energy as:

$$p_i = \sqrt{E_i^2 - m_i^2} \quad (1.11)$$

$$= E_i \left(1 - \frac{m_i^2}{E_i^2} \right)^{\frac{1}{2}}. \quad (1.12)$$

Assuming that the neutrino's mass is much less than its momentum Eq. 1.12 can be Taylor expanded as:

$$p_i \approx E_i + \frac{m_i^2}{2E_i}. \quad (1.13)$$

For ultra-relativistic particles like the neutrino the time t , and distance traveled x are approximately the same. The distance the neutrino travels will from here be denoted as L . It is assumed that all of the initial neutrino states have the same energy E . Using these assumptions the oscillation

probability in Eq. 1.10 can be written as:

$$\mathcal{P}(\nu_f \rightarrow \nu_g) = \sum_i \sum_j U_{gi} U_{fi}^* U_{gj}^* U_{fj} e^{\frac{-i\Delta m_{ji}^2 L}{2E}} \quad (1.14)$$

where $\Delta m_{ji}^2 = m_i^2 - m_j^2$ is the difference in the squares of the i th and j th mass states.

By expanding these sums the probability that a neutrino will oscillate is typically written as:

$$\begin{aligned} \mathcal{P}_{\alpha \rightarrow \beta} &= |\langle \nu_\beta(x) | \nu_\alpha(0) \rangle|^2 \\ &= \delta_{\alpha\beta} - 4 \sum_{i>j} \text{Re}[U_{\beta i} U_{\alpha i}^* U_{\beta j}^* U_{\alpha j}] \sin^2 \left(\frac{\Delta m_{ij}^2 L}{4E} \right) \\ &\quad + 2 \sum_{i>j} \text{Im}[U_{\beta i} U_{\alpha i}^* U_{\beta j}^* U_{\alpha j}] \sin \left(\frac{\Delta m_{ij}^2 L}{2E} \right). \end{aligned} \quad (1.15)$$

The probability for anti-neutrinos to oscillate is the same except that the sign of the last term is flipped. This term is the one that makes it possible for neutrinos and anti-neutrinos to oscillate differently, which may give rise to charge-parity (CP) violation in the lepton sector. It is of note that the oscillation probability depends only on the differences in the squares of the mass states, which means that they are not sensitive to the absolute scale of the neutrino masses.

The matrix U is called the Pontocorvo-Maki-Nakagawa-Sakata (PMNS) matrix and is traditionally written as the product of three unitary transformations which are parameterized in terms of three mixing angles $(\theta_{12}, \theta_{13}, \theta_{23})$,

and one overall phase (δ_{CP}),

$$\begin{aligned}
U &= \begin{pmatrix} e1 & e2 & e3 \\ \mu1 & \mu2 & \mu3 \\ \tau1 & \tau2 & \tau3 \end{pmatrix} & (1.16) \\
&= \begin{pmatrix} 1 & 0 & 0 \\ 0 & c_{23} & s_{23} \\ 0 & -s_{23} & c_{23} \end{pmatrix} \begin{pmatrix} c_{13} & 0 & s_{13}e^{-i\delta_{CP}} \\ 0 & 1 & 0 \\ -s_{13}e^{i\delta_{CP}} & 0 & c_{13} \end{pmatrix} \begin{pmatrix} c_{12} & s_{12} & 0 \\ -s_{12} & c_{12} & 0 \\ 0 & 0 & 1 \end{pmatrix},
\end{aligned}$$

where $c_{ij} = \cos(\theta_{ij})$ and $s_{ij} = \sin(\theta_{ij})$, for $i, j = 1, 2, 3$ and δ_{CP} is responsible for CP violation in the neutrino sector. θ_{23} in the first term was originally measured using atmospheric neutrinos, and now measurements can also be made using accelerator produced neutrinos. θ_{13} in the second term was originally measured using reactor neutrinos and is currently measured with reactor neutrinos and using accelerator produced neutrino beams. θ_{12} is measured using solar and reactor neutrinos. The mass splittings can be fully described by just two differences in the mass states: Δm_{21}^2 , Δm_{32}^2 , where $\Delta m_{31}^2 = \Delta m_{21}^2 + \Delta m_{32}^2$. An overview of the measurements of these parameters will be discussed in Section 1.4.

Current accelerator-based neutrino oscillation experiments, like T2K which will be discussed in more detail in Chapter 2, typically begin with a beam initially comprised of ν_μ and measure either neutrino appearance or disappearance, where the oscillation probability is approximated with the leading order terms. One type of appearance corresponds to finding a neutrino of flavor ν_e in a beam comprised of ν_μ , and this occurs with probability

$$\begin{aligned}
\mathcal{P}(\nu_\mu \rightarrow \nu_e) &\approx \sin^2(2\theta_{13}) \sin^2(\theta_{23}) \sin^2\left(\frac{\Delta m_{31}^2 L}{4E}\right) \\
&+ \sin(2\theta_{12}) \sin(2\theta_{13}) \sin(2\theta_{23}) \cos \theta_{13} \sin\left(\frac{\Delta m_{21}^2 L}{4E}\right) \sin\left(\frac{\Delta m_{31}^2 L}{4E}\right) \\
&\times \left[\cos\left(\frac{\Delta m_{32}^2 L}{4E}\right) \cos \delta_{CP} - \sin\left(\frac{\Delta m_{32}^2 L}{4E}\right) \sin \delta_{CP} \right] & (1.17)
\end{aligned}$$

+ solar and matter effect terms.

Disappearance corresponds to finding fewer ν_μ than predicted by the neutrino flux alone because they have oscillated into other neutrino flavors, and to first order the probability of seeing a ν_μ after oscillations is:

$$\mathcal{P}(\nu_\mu \rightarrow \nu_\mu) \approx 1 - [\cos^2 \theta_{13} \sin^2(2\theta_{23}) + \sin^4 \theta_{23} \sin^2 \theta_{23}] \sin^2 \left(\frac{\Delta m_{32}^2 L}{4E} \right) + \text{solar and matter effect terms.} \quad (1.18)$$

For antineutrinos Eq. 1.17 is the same except that, as mentioned earlier, the term that is sensitive to δ_{CP} switches signs. The survival probability for muon neutrinos is the same for neutrinos and anti-neutrinos. These oscillation probability formulas also show that oscillations can only occur if neutrinos have non-zero mass.

Oscillations in Matter

Neutrino oscillations often do not actually occur in a vacuum as assumed in the formalism described above. Solar neutrinos travel through the sun, atmospheric neutrinos travel through the atmosphere, and perhaps through the Earth as in the Super-Kamiokande oscillation measurement, and beams of accelerator neutrinos travel through the Earth's crust. Interactions the neutrinos undergo as they travel in matter affect the properties of the oscillations. The formalism to describe these effects was developed by Wolfenstein, Mikheev and Smirnov [37] [38]. Most charged current neutrino interactions produce a lepton, not a neutrino, and these do not affect the oscillation physics except through a small reduction in the overall expected neutrino flux. Neutral current interactions affect all neutrino flavors equally and so acts as an overall phase shift that can be factored out of the oscillation physics. Charged current scattering interactions of an electron neutrino off of an electron in matter can impact the oscillations. This is because matter contains electrons, but not muons or taus, which means that only electron neutrinos can undergo these interactions. These interactions add an extra term to the electron neutrino Hamiltonian: $V_{CC} = \pm\sqrt{2}G_F N_e$, where G_F is the Fermi coupling constant, N_e is the electron density of the material

and the sign depends on whether neutrinos or anti-neutrinos are described. This means that the measured flavor and mass states are slightly different than the ones described above and the interactions in matter can mimic the signature of CP violation. Similarly the oscillation probabilities in matter depend on the mass states squared, Δm^2 s, which gives experiments sensitivity to the neutrino mass hierarchy [10]. Experiments with longer distances between production and detection, such as the Super-Kamiokande atmospheric neutrino measurement, are more sensitive to the mass hierarchy because neutrinos travel from one side of the Earth to the other which increases the size of the matter effects.

1.4 Neutrino Oscillation Measurements

This section describes the current world measurements of the neutrino oscillation parameters. As illustrated in the oscillation probability formulas above, all of the parameters are highly correlated and fits are done to the existing experimental data by phenomenologists and the Particle Data Group (PDG) to extract as much information from the data as possible.

θ_{12} and Δm_{21}^2 are measured using a fit to experiments that measure solar neutrinos, like SNO, Super-Kamiokande, Borexino, and Kamland with long baseline reactor neutrinos at a distance of 180 km on average [12] [39] [40] [41]. The latest results for the Kamland experiment is shown in Fig. 1.2.

θ_{23} and Δm_{32}^2 can be measured using accelerator neutrinos such as in MINOS, NOvA and T2K, as well as with atmospheric neutrinos such as in IceCube and SK [13] [14] [15] [16] [17]. The world measurements of these parameters by each experiment are compared in Fig. 1.3.

θ_{13} and Δm_{31}^2 can be measured with short baseline reactor neutrinos with a baseline of about 1 km like Daya Bay, Double Chooz and Reno, or with accelerator neutrinos like with T2K and NOvA [13] [14] [42] [43] [44].

The best fit parameters as measured by the PDG fit are given in Table 1.1. This result assumes that $\Delta m_{31}^2 \approx \Delta m_{32}^2$ because Δm_{21}^2 has been measured to be much smaller than Δm_{31}^2 or Δm_{32}^2 .

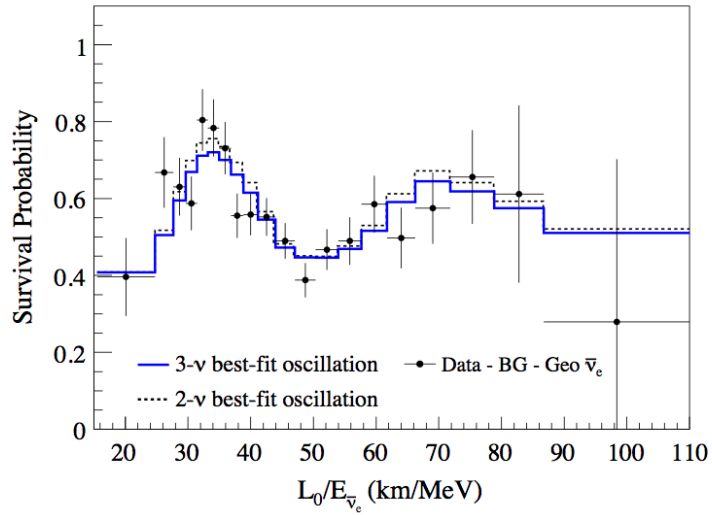


Figure 1.2: Latest Kamland result showing $\bar{\nu}_e$ oscillations. Figure from [12].

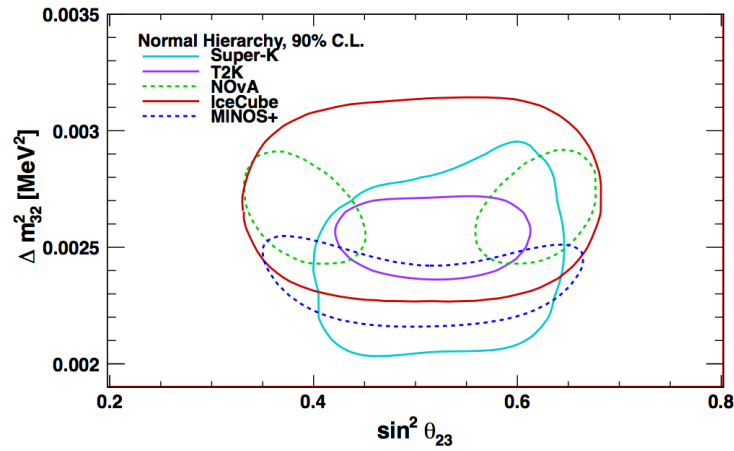


Figure 1.3: Contours of allowed fit regions for Δm_{32}^2 and $\sin^2 \theta_{23}$. Data from T2K [13], NOvA [14], SK [15], MINOS+ [16], and IceCube [17] are compared. Figure from [15].

Table 1.1: Best fit parameters for neutrino oscillations [10].

Parameter	Normal Hierarchy	Inverted Hierarchy
$\sin^2 \theta_{12}$	$0.307^{+0.013}_{-0.012}$	$0.307^{+0.013}_{-0.012}$
$\sin^2 \theta_{13} (\times 10^{-2})$	$2.10^{+0.11}_{-0.11}$	$2.10^{+0.11}_{-0.11}$
$\sin^2 \theta_{23}$	$0.51^{+0.04}_{-0.04}$	$0.50^{+0.04}_{-0.04}$
$\Delta m_{21}^2 (\times 10^{-5} \text{ eV}^2)$	$7.53^{+0.18}_{-0.18}$	$7.53^{+0.18}_{-0.18}$
$\Delta m_{32}^2 (\times 10^{-3} \text{ eV}^2)$	$2.45^{+0.05}_{-0.05}$	$2.52^{+0.05}_{-0.05}$
δ_{CP}/π	0-2	0-2

1.5 Open Questions

Although at this point all of the neutrino mixing angles and mass splittings have been measured there are still many important open questions.

First, there has, to this point, been no statistically significant observation of δ_{CP} , so it is unknown to what extent there is CP violation in neutrinos, and to what extent this might explain the CP violation necessary to create the universe we have today given our models of the Big Bang and early universe. There are some hints from the T2K experiment that there may be CP violation in neutrinos, because the CP conserving values of $\delta_{CP} = 0$ and $\delta_{CP} = \pi$ are excluded at the two sigma level [45]. Confirmation and precision measurements of δ_{CP} will require more data, such as proposed in continued running of the T2K experiment as T2K-II [46] and the NOvA experiment [14], or in future experiments such as DUNE [47] [48] or Hyper-Kamiokande [49]. These measurements will also require continued effort to precisely measure the other mixing parameters because, as mentioned earlier, δ_{CP} dependence is a second order oscillation effect, and any uncertainty in the first order term will make the measurements more difficult.

Another open question is if θ_{23} is exactly maximal at 45° , and if not, which octant the angle is in. At this point, as illustrated in Fig. 1.3, the

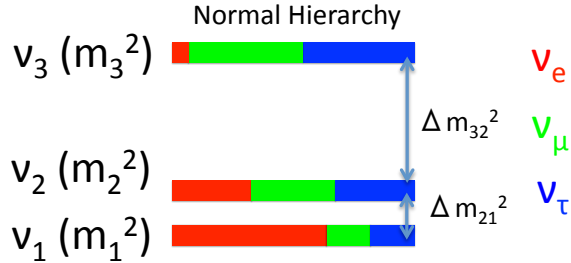


Figure 1.4: Illustration of the normal mass hierarchy.

NOvA experiment has excluded maximal mixing at 2.6 sigma [14], but the latest results from other experiments are still consistent with maximal mixing.

There are also many open questions associated with neutrino mass. As mentioned earlier, oscillations are only sensitive to the differences in the mass states squared, not the absolute scale of the neutrino masses. There is a limit on the neutrino mass from cosmological measurements of the cosmic microwave background (CMB) because the mass of the neutrinos would affect the early universe. These measurements indicate that the sum of the three neutrino mass states must be less than 0.23 eV [50]. The fact that neutrinos oscillate mean that at least two mass states must be nonzero [51]. The ordering of the mass states, referred to as the neutrino mass hierarchy, is also unknown. Neutrinos could follow the normal hierarchy ($m_1 < m_2 < m_3$) or the inverted hierarchy ($m_3 < m_1 < m_2$). An illustration of the normal hierarchy is shown in Fig. 1.4. The neutrino mass hierarchy will be measured by oscillation experiments. As shown earlier in the PDG global fit values of the neutrino mixing parameter measurements are currently degenerate without knowing the neutrino mass hierarchy [10].

Neutrinos may be Majorana fermions which would mean that they are their own anti-particles. This type of particle has never before been observed. It is possible to measure if neutrinos are Majorana by looking for neutrino-less double beta decay:

$$(A, Z) \rightarrow (A, Z + 2) + e^- + e^-. \quad (1.19)$$

Experiments are searching for this process. If the neutrino mass hierarchy is inverted then the predicted decay rates will be high enough that these current or next generation experiments will be sensitive to neutrino-less double beta decay. If the mass hierarchy is normal then the decay rates can be almost two orders of magnitude lower which makes the process more difficult to detect. Measurements of the neutrino mass hierarchy will inform the future of these experiments [51].

Chapter 2

T2K Experiment

T2K is a “long baseline” neutrino experiment designed to perform precision measurements of the neutrino mixing parameters and neutrino cross sections. The experiment consists of three main components: the neutrino beam, a near detector complex located 280 m away from the target in the neutrino beam line (ND280 and INGRID), and a far detector Super-Kamiokande (SK) located 295 km from the target, as illustrated in Fig. 2.1 [18].

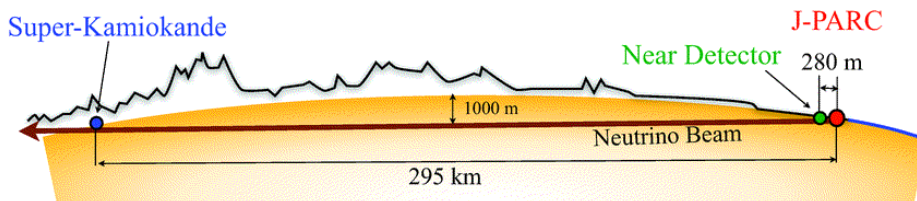


Figure 2.1: Path that T2K neutrino travels from production to detection. Figure from [18].

2.1 Neutrino Beam

The T2K experiment measures neutrinos that are produced in a neutrino beam at the Japan Proton Accelerator Research Complex (J-PARC) in Tokai, Ibaraki, Japan. Protons are accelerated through a series of accel-

erators and then sent to create a neutrino beam as illustrated in Fig. 2.2.

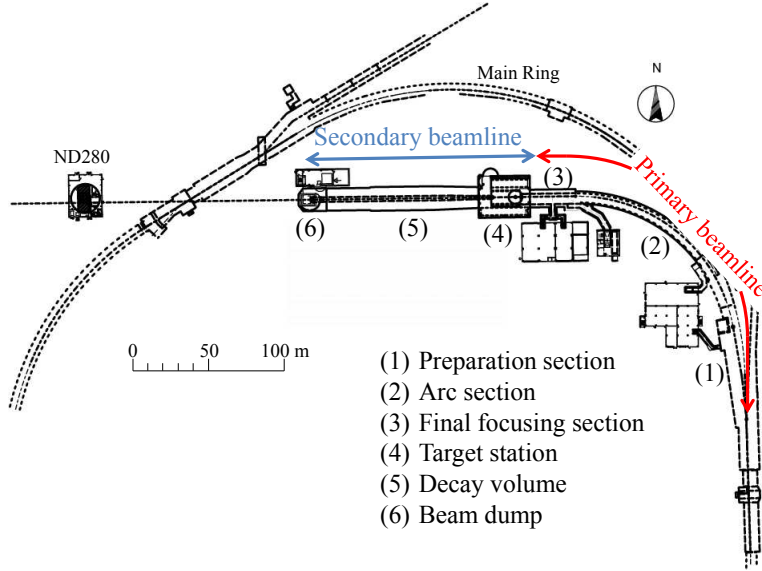


Figure 2.2: The T2K beamline. Protons enter from the bottom right. They are then sent into the primary beam line which bends them left towards the secondary beam line. Figure from [18].

First, a linear accelerator (LINAC), accelerates negative hydrogen ions (H^-) up to 400 MeV in kinetic energy. Then charge stripping foils are used to change it to a H^+ beam. These protons are then accelerated up to 3 GeV in a rapid cycling synchrotron, and finally to the main ring synchrotron in which they are accelerated to 30 GeV in eight bunches. Five kicker magnets eject the eight proton bunches, called a spill, from the main ring within a single turn. Spills happen every 2-3 seconds and there are about 3×10^{14} protons per spill at the current J-PARC beam power of 475 kW.

These protons are sent to the primary neutrino beamline in which the protons are pointed towards Super-Kamiokande. First the beam is tuned with a series of 11 magnets called the preparation section. This beam is then curved towards SK at an angle of 80.7° with a radius of 104 m using a series of 14 additional magnets, which is called the arc section. Finally the protons are focused onto a graphite target using a series of ten magnets in

the final focusing section.

The secondary neutrino beamline begins with the graphite target, which is a cylindrical graphite rod of 2.6 cm diameter and 91.4 cm long located in the target station. As the protons from the primary beamline interact in the target they produce charged pions, which are focused using a series of three electromagnetic horns. The polarity of these horns can be switched to focus either positively or negatively charged pions which makes it possible to create either a neutrino or anti-neutrino beam. The pions are then sent into a 96 m long steel decay volume where they decay into muons and muon neutrinos. At the end of the beam line is shielding, called a beam dump, which consists of 75 tons of graphite followed by 2.4 m of iron plates. This stops most remaining decay products except the neutrinos. The primary and secondary beamlines are illustrated in Fig. 2.2.

The neutrino beam is directed 2.5° off-axis from SK to position the peak of the neutrino energy spectrum at $E_\nu = 0.6$ GeV where the neutrino oscillation effect is largest for a baseline of 295 km [18]. This off-axis technique makes it possible to “focus” the energy of the neutrino beam because the neutrinos are produced in two body pion decay [52]. The neutrino energy can be calculated in terms of the pion kinematics as:

$$E_\nu = \frac{m_\pi^2 - m_\mu^2}{2(E_\pi - p_\pi \cos \theta_{\nu\pi})} \quad (2.1)$$

where m_π and m_μ are the masses of the pion and muon, E_π and p_π are the energy and momentum of the pion, and $\theta_{\nu\pi}$ is the angle between the neutrino and pion directions. For $\theta_{\nu\pi} = 0$ neutrino energy is proportional to the pion momentum, but for larger off axis angles the energy dependence on pion momentum almost disappears.

Fig. 2.3 shows that the chosen 2.5° off-axis angle for T2K corresponds with maximum oscillation at the peak of the neutrino flux [6].

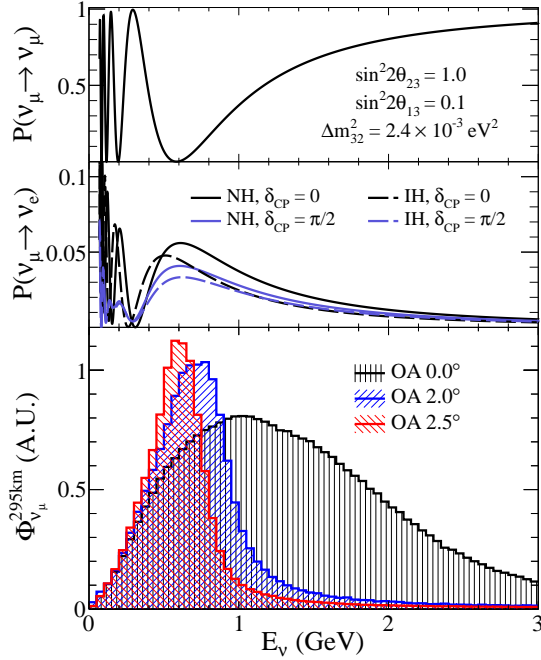


Figure 2.3: An illustration of the probability of ν_μ survival (top), ν_e appearance (middle), and neutrino flux from the T2K beam-line as a function of neutrino energy for several off axis angles (bottom). Figure from [6].

2.2 Near Detector

The T2K near detector consists of an on-axis and an off-axis component, both located 280 m from the target. The on-axis part of the detector measures the neutrino beam direction and profile as well as the neutrino rate per protons on target. The off-axis part of the detector measures the neutrino flux and energy spectrum, as well as neutrino cross sections.

2.2.1 INGRID

The INGRID detector (Interactive Neutrino GRID) is the on-axis part of the near detector that measures the beam direction and profile. It is made of 16 identical modules which each consist of nine iron plates of $1.24 \times 1.24 \text{ m}^2$ interspersed with 11 tracking scintillator plates. Fourteen of these

modules are stacked and arranged as a cross as illustrated in Fig. 2.4, where the center of the cross corresponds to the center of the neutrino beam. This allows INGRID to measure a 10 m by 10 m section of the beam. Two additional modules are also placed off-axis on either side of the cross to measure the beam symmetry. INGRID measures the beam center to within 10 cm [53].

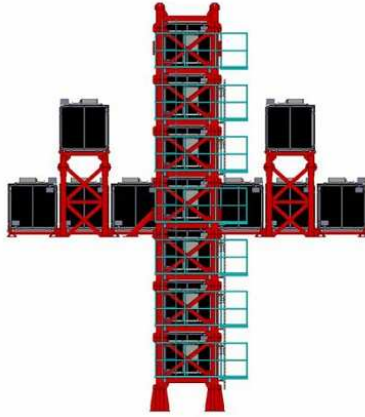


Figure 2.4: An illustration of the INGRID detector. The beam passes straight through the center of the module at the center of the cross. Figure from [18].

2.2.2 ND280

ND280 is the off-axis component of the T2K near detector, positioned 2.5° away from the beam center. This detector is used to measure the neutrino energy spectrum as well as the beam contamination from electron neutrinos. Many cross section measurements can also be made in this detector. ND280 is made up of multiple sub-detectors as illustrated in Fig 2.5 [18]. The center of the detector contains two fine grained scintillating detectors (FGDs), sandwiched with three time projection chambers (TPCs). A π^0 detector (P0D) is located on the upstream end of the first TPC, and an electromagnetic calorimeter (ECAL) is located downstream of the tracking detectors. These detectors are surrounded by barrel ECALs and a magnet.

Scintillator was attached to the magnet to act as a side muon range detector (SMRD).

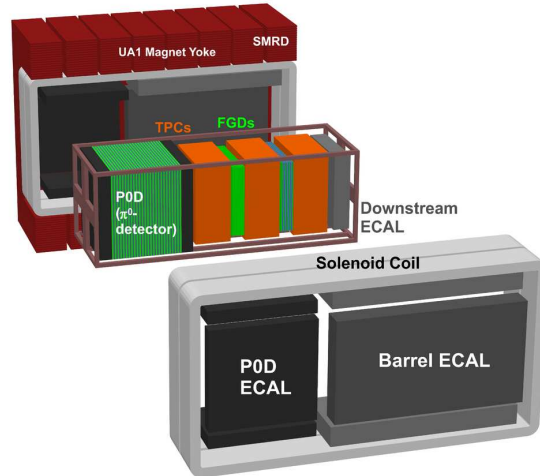


Figure 2.5: An illustration of the ND280 detector. The neutrino beam passes from left to right through the center of the detector. Figure from [18].

Magnet

The magnet that surrounds the ND280 detector was first used in the CERN UA1 and NOMAD experiments. It was refurbished and shipped to Tokai for T2K. The magnet is made of water cooled aluminum coils. This inner volume is surrounded by eight magnet yokes. The total magnet dimensions are $7.6 \text{ m} \times 5.6 \text{ m} \times 6.1 \text{ m}$. A current of 2900 A is used to produce a dipole magnetic field of 0.2 T. The field is constant to within 10^{-3} of the nominal value. The magnet makes it possible to measure particle momentum and determine the sign of charged particles from neutrino interactions in ND280. This is because the charged particles bend in the magnetic field.

Fine Grained Detectors

The FGDs are at the center of the ND280 detector. They are made of long narrow scintillator bars ($9.61 \text{ mm} \times 9.61 \text{ mm} \times 1.8643 \text{ m}$) with wavelength shifting fibers in the center. One end of the fiber has a mirror to reflect the light back along the fiber, and the other is attached to a multi-pixel photon counter (MPPC). The MPPCs are photon counters that work in high magnetic fields. They each contain 667 pixels arranged in a $1.3 \times 1.3 \text{ mm}^2$ active region. Each of the pixels is a Geiger micro-counter which creates a signal when electron-hole pairs are created by exciting electrons in a semiconductor above the band gap. These pixels are binary devices, but the sum of the total charge from each of the pixels is proportional to the number of incident photons assuming that the number of photons is small compared to the total number of pixels [54].

The scintillating bars are arranged into layers by placing 192 of them beside each other. Then 192 more bars are glued perpendicularly to the bars of the first layer to make a module. This design makes it possible to track particles granularly in both x and y . When neutrinos interact in the detector they produce charged particles. As these charged particles travel through the scintillator bars light is produced in each of the scintillator bars through which the particle passes. Using the information from the MPPCs to read out which bars have collected scintillation light and how much light there is, it is possible to reconstruct the path of the particle in the detector.

The first FGD is made of 15 scintillator modules. The second FGD alternates six water modules that are 2.5 cm thick with seven scintillator modules. This makes it possible to measure neutrino interactions on water as well as on carbon, which is important as the far detector, Super-Kamiokande, is water [54].

Time Projection Chambers

The three TPCs are positioned around the FGDs within the ND280 detector. They are made of two concentric boxes. The inner box is filled with argon gas and has copper-clad G10 walls instrumented with twelve micromegas

detectors on either end. There is a central cathode in the middle to provide an electric field. The outer box contains CO₂ to insulate the inner box. As a charged particle travels through the TPC it ionizes and produces electrons which drift away from the central cathode, which is connected to a high voltage, and towards the readout planes. Information from the readout planes combined with timing information and the ionization drift velocity makes it possible to reconstruct the three dimensional path of the particles. The TPC is used to determine the number of particles produced in a neutrino interaction as well as their momenta, which is possible because of the surrounding magnetic field. Particle identification can be done in the TPC using the energy loss of charged particles along the track. The TPCs typically measure neutrino interactions with vertices in the more massive surrounding detectors such as the FGDs [55].

P0D

The π^0 detector (P0D) was designed to measure neutral current single π^0 (NC1 π^0) cross sections on water and carbon. The NC1 π^0 neutrino interaction is defined as: $\nu + n/p \rightarrow \nu + \pi^0 + n/p$. This is one of the main backgrounds for a ν_e appearance measurement. This detector contains three regions. The center region is made of alternating scintillator modules and water modules with brass sheets which can produce electromagnetic showers. The scintillator modules are made of perpendicular arrays of triangular scintillator bars read out by a wavelength shifting fiber and MPPC. The water modules each contain two bags that can either be filled with water or be empty. On either end of this central detector are alternating scintillator plates and lead sheets. This outer region is designed to produce electromagnetic showers in the lead as well as provide a veto. Neutrinos will interact in the scintillator and metal as well as the water, so to determine a cross section, the P0D is operated with and without water so that a subtraction method can be used [56].

ECal

The ECal surrounds the P0D, TPC and FGD in 13 separate modules. Each module is made of layers of scintillator interspersed with 1.75 mm of lead. The scintillator is read out with a wavelength shifting fiber and MPPC. There are six modules parallel to the beam around the FGD and TPC. These complement the FGD and TPC by reconstructing π^0 and photons produced in the FGD and TPC, that the FGD and TPC are not well designed to reconstruct because photons are not charged. Each of the modules along the beam direction contain 31 layers of lead and scintillator. The module farthest downstream along the beam direction is made of 34 layers of lead and scintillator. Six dedicated ECal modules surround the P0D parallel to the beam. These have only six layers of lead and scintillator each because they are primarily used to reconstruct energy missed by the P0D, or as a veto [57].

SMRD

The SMRD instruments the magnet surrounding the ND280 detectors. Each of the eight magnet yokes is made of 16 iron plates with 1.7 cm of air between them. The SMRD contains 440 scintillator modules placed in these gaps. The first five magnet yokes contain three layers of scintillator, the sixth yoke contains four layers of scintillator and the final two yokes contain six layers of scintillator. The scintillator is in all cases placed in the innermost gaps to measure particles escaping from the inner detectors. This detector can be used to measure muons escaping from the inner detector, as a trigger for a cosmic muon control sample, and as a way to identify beam interactions in the magnet [58].

2.3 Super-Kamiokande

Super-Kamiokande is a 50 kTon cylindrical water Cherenkov detector located in the Mozumi mine 1 km under Mt. Ikenoyama in Gifu, Japan. It has been operating since April 1996. Over the years the detector has changed, which has lead to several distinct analysis periods. As the T2K

experiment is taking place during the SK period that began in 2008 and has continued to the present, this is the detector configuration that will be described here.

2.3.1 Detector Design

The SK detector is composed of optically separated inner and outer detectors that fill a cylindrical stainless steel tank 41.4 m tall, and 39.3 m in diameter as illustrated in Fig. 2.6 [59]. It is designed to detect Cherenkov radiation produced in the inner detector water.

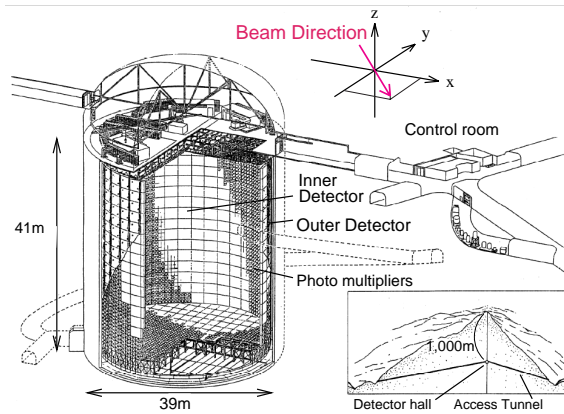


Figure 2.6: An illustration of the SK detector. Figure from [6].

The inner detector is 36.2 m tall, and 33.8 m in diameter, which corresponds to 32 kTon of water. This means that the diagonal is approximately 50 m, or on the order of the attenuation and scattering lengths for ultra-pure water. It is lined with 11,129 photo-multiplier tubes (PMTs) with a 20 inch diameter, which corresponds to 40% photocathode coverage by area. These PMTs have 20% quantum efficiency and 70% collection efficiency at the first dynode [19]. They are protected by fiber reinforced plastic covers with acrylic front windows which have 96% transparency for photons. The PMTs are mounted in modules composed of 3 by 2 PMTs which are placed in rows to cover the inner detector. The space between the tubes is covered with black plastic sheet to prevent reflections [59].

The outer detector is designed to veto backgrounds from cosmic muons and radioactivity in the mountain rock surrounding the tank. It is 2.6 m thick on the top and bottom, and 2.7 m wide on the sides, which corresponds to 18 kTon of water. It has 1885 outward facing 20 inch photo tubes attached to wavelength shifting plates, which corresponds to 20% photocathode coverage by area. The wavelength shifting plates, along with white Tyvek coating on the walls between the PMTs maximizes the light collection and veto efficiency of the detector [59]. The PMTs and wavelength shifting fibers in the outer detector were previously used in the IMB experiment. The outer detector has almost 100% efficiency for rejecting entering muons.

There is a dead region of about 55 cm between these two detector regions due to the support structure that holds the PMTs in place. This space is optically separated from the inner and outer detectors so that light will not escape into the active regions.

The entire detector is filled with ultra-pure water which is constantly being processed by a water system to maintain the transparency of the water and minimize background from naturally occurring radiation.

The registered charges, and associated hit times are sent from each PMT to custom boards in electronics huts located on top of the SK tank. The threshold for recording a signal is 0.25 photo electrons (p.e.) which corresponds to -0.69 mV [19]. The boards generate a square wave that begins at the first time light is recorded at the PMT, with the length of the square wave proportional to the integrated PMT charge. Then it uses a time to digital converter to digitize the analog signals and is sent by ethernet to computers that process the data with a software trigger. Each board can accommodate 8 PMT channels [18].

These hits are sorted into event candidates using a series of computers and software triggers. For T2K beam data all times and charges within a 1 ms time window of the T2K beam spill time, as determined by GPS, are recorded. Events in these time windows are categorized in one of three ways. Fully contained (FC) events are above 30 MeV in reconstructed electron energy, and contain tracks that begin and end in the SK inner detector and have fewer than 16 hits in the outer detector. Outer detector events have 16

Table 2.1: Cherenkov thresholds for particles in water. Calculated using masses from [10].

Particle	Mass (MeV/ c^2)	Threshold (MeV/ c)
e	0.511	0.583
μ	105.7	120.5
π^+	139.6	159.2
p	938.3	1070

or more hits in the outer detector. Low energy events are defined as events that are fully contained within the detector, but are too low energy to fall in the fully contained sample. Typically only the fully contained events are used in physics analyses [18].

2.3.2 Cherenkov Radiation

Cherenkov radiation is produced when charged particles move faster than the speed of light in a medium [60]. The speed of light in a medium is related to the index of refraction of the medium, n . In the SK detector, charged particles produce light when they have velocity

$$v > \frac{c}{n}, \quad (2.2)$$

where $n = 1.33$ for water.

This limit is often expressed in terms of the minimum momentum a charged particle must have in order to produce Cherenkov light. This is referred to as the Cherenkov threshold, and calculated in terms of the index of refraction, n , and the particle's mass m as

$$p_{\min} = \frac{mc}{\sqrt{n^2 - 1}}. \quad (2.3)$$

Cherenkov thresholds for some typical particles in the SK detector are given in Table 2.1.

As a particle travels in the water, Cherenkov light is produced as a cone of light around the trajectory of the particle, so in the SK tank particles

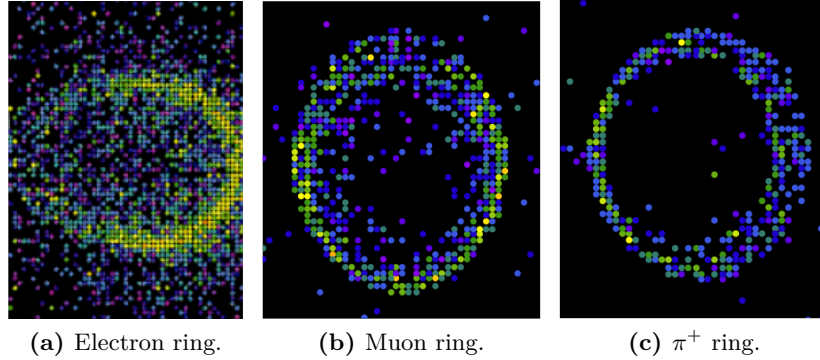


Figure 2.7: Simulated Cherenkov rings produced by an electron, muon and charged pion.

are seen as rings of light projected on the walls. The angle of emission is a function of the speed the particle is moving:

$$\cos \theta_c = \frac{1}{\beta n}, \quad (2.4)$$

where $\beta = \frac{v}{c}$.

Faster particles will emit Cherenkov radiation at larger angles, with a maximum of 41.2° in water, and as a particle slows while traveling through a medium, the Cherenkov cone will slowly collapse until no light is emitted [61]. Different particles will produce different patterns of Cherenkov light. Muon and electron Cherenkov rings are distinct because electrons will shower in the water producing “fuzzy rings”, while muons travel in a straighter trajectory which produces a sharper ring. Due to their similar masses charged pions and muons produce similar rings, except that the pions may interact hadronically. Simulated electron, muon and charged pion rings are displayed in Fig 2.7.

The Cherenkov light produced by charged particles from neutrino interactions is detected in the SK PMTs and used to determine what happened in a given interaction. This will be described in detail in Chapter 4.

2.3.3 Calibration

Calibration of the Super-Kamiokande detector is essential for understanding the detector output and making the physics measurements of interest to T2K.

Relative PMT Gain Calibration

The PMT gain is used to convert the output PMT charge to photoelectrons, and needs to be calibrated for each PMT. This is done by first calibrating the relative gain difference between each PMT. A nitrogen laser driven dye laser is used as a stable light source with constant intensity. The laser initially emits light at 337 nm, and then this light is shifted to 398 nm with a dye. Light is sent into the detector with an optical fiber connected to a diffuser ball placed in the center of the SK tank to produce isotropic light. The laser is run in two modes, high intensity and low intensity which are selected by changing the intensity of the laser light with a variable optical filter. In the high intensity mode each PMT has enough light to calculate an average charge $Q(i)$ for each PMT. In the low intensity mode only a few PMTs are hit so it is possible to assume that all of the hits are single photoelectron hits, and the number of times a PMT is hit $N(i)$ can be measured. If these two quantities $Q(i)$ and $N(i)$ are measured in the same place, they are mostly identical except for the PMT gain for the i th PMT:

$$Q(i) \propto I_{\text{high}} a(i) \epsilon_{QE}(i) G(i) \quad (2.5)$$

$$N(i) \propto I_{\text{low}} a(i) \epsilon_{QE}(i) \quad (2.6)$$

where I_{high} and I_{low} are the intensities of the high and low intensity light from the laser, $a(i)$ is the PMT acceptance ϵ_{QE} is the quantum and collection efficiency and $G(i)$ is the PMT gain.

Then the PMT gain can be calculated as

$$G(i) = \frac{Q(i)}{N(i)}, \quad (2.7)$$

using the measurements of $Q(i)$ and $N(i)$. This ratio is tabulated for each PMT and is used to convert charge to photoelectrons on a PMT by PMT basis. The root mean squared (RMS) of the PMT gains in the detector is 5.9%, which is assumed to be due to differences in the quantum and collection efficiencies [19].

Absolute Gain Calibration

The absolute gain of the detector is measured using a nickel source that produces a uniform source of light at the one photo electron level. The nickel source is a ball of NiO and polyethylene with a californium-252 source inserted in the center. The californium source produces neutrons which capture on the nickel and result in the reaction $\text{Ni}^{58} + n \rightarrow \text{Ni}^{59} + \gamma$. This provides an isotropic source of 9 MeV gammas which produce an average of 0.004 photoelectrons per PMT per event when placed at the center of the SK detector, and means that more than 99% of the event signals are at the one photoelectron level.

All of the one photoelectron distributions from each PMT are added together in PMT charge to find the absolute gain of the SK detector. The PMT by PMT corrections as determined in the relative gain calibration are included to account for differences between the PMTs. The average of this summed single photoelectron distribution over the range of output charges is the absolute gain of the SK detector. It is found to be 2.658 pC per photoelectron as measured at the beginning of the latest SK run period. This summed single photoelectron distribution is used in the detector simulation [19].

Relative Quantum Efficiency

For low intensity light, as described in the relative gain calibration, the hit probability is proportional to the PMT quantum and collection efficiency, ϵ_{QE} . Using Eq. 2.6 the quantum and collection efficiency can be written as:

$$\epsilon_{QE} = \frac{N_i}{I_{\text{low}} a(i)}. \quad (2.8)$$

The number of hits N_i is calculated as the ratio of the number of observed hits to the number of predicted hits where the predicted hits are calculated with the detector simulation. Corrections are applied to take into account the PMT position relative to the source, the PMT acceptance $a(i)$, and the properties of light propagation in the detector. Any remaining differences are attributed to the quantum and collection efficiencies. These are tabulated relative to the average for each PMT and are used in the detector simulation [19].

Timing Calibration

The timing of the detector also needs to be calibrated. The timing response of different channels can vary based on various factors such as the length of the PMT cables and the processing time of the readout electronics. It also depends on the observed charge, as the amount of time it takes a large pulse to cross the discriminator threshold is shorter than for a small pulse.

This calibration is done with a fast pulsing nitrogen laser, and an optical filter is used to vary the light intensity. The filtered light goes into a diffuser ball in the center of the SK tank via an optical fiber, and this produces an isotropic source of light. The time that the laser light is emitted is measured with a dedicated 2 inch PMT, and then the channel response time is corrected with this emission time as well as the time it will take light to travel from the center of the tank. Using the optical filter to vary the pulse height of the light, the two dimensional distribution of timing and charge are measured for each channel. Each charge bin is fit with an asymmetric Gaussian distribution to reproduce the timing distribution of the data, and these are used in the SK detector simulation [19].

Water Quality Calibrations

The optical properties of the water that Cherenkov light travels through are calibrated using a laser injected vertically into the SK tank. The properties of light transmission are measured as a distance from the bottom of the tank. The tank is broken up vertically into five PMT regions, and a sixth

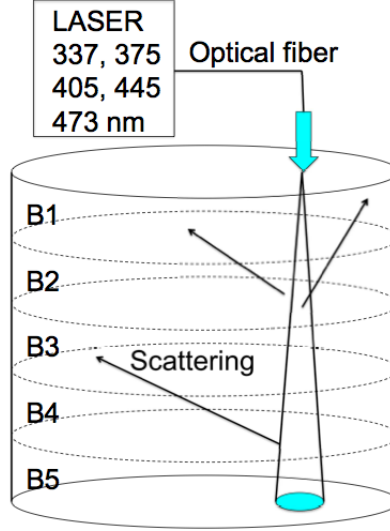


Figure 2.8: Illustration of the five vertical slices B1-B5 that the SK tank is broken up into to calibrate the properties of the water. The sixth corresponds to the PMTs on the top of the tank. Figure from [19].

region is defined as the PMTs on the top of the tank. These are illustrated in Fig. 2.8.

The time of flight corrected timing distributions are calculated for the PMTs in each detector region B1 to B5 and the top PMTs, and Monte-Carlo parameters are generated to match the data. These timing distributions are broken into a “scattering and absorption” region as well as a reflection region.

In the scattering and absorption region the laser light is modeled as a function of wavelength as:

$$I(\lambda) = I_0(\lambda) \exp \left[\frac{-l}{L(\lambda)} \right] \quad (2.9)$$

where I_0 is the initial intensity of the laser, l is the distance the light travels, and $L(\lambda)$ is the attenuation length due to scattering and absorption.

The attenuation length is described in terms of three components: ab-

sorption, and two angular regions of scattering defined by the scattered photon angle θ . Symmetric scattering is due to Rayleigh and symmetric Mie scattering with an angular distribution of $1 + \cos \theta$. Asymmetric scattering is primarily due to forward Mie scattering where the scattering is described by $\cos \theta$ in the forward direction, and there is no backward scattering.

This means the attenuation length may be written as

$$L(\lambda) = \frac{1}{\alpha_{\text{abs}}(\lambda) + \alpha_{\text{sym}}(\lambda) + \alpha_{\text{asym}}(\lambda)} \quad (2.10)$$

where the α parameters are determined from fits to the laser data.

The water transparency is measured as the amount of scattering and absorption of light in the SK water. This is done by injecting laser light of varying wavelengths into the SK tank. Combining the attenuation lengths from each of these components leads to a total attenuation length of 120 m for light with a wavelength of 400 nm.

The reflection portion of the timing distribution from the laser data is used to measure the effective complex index of refraction at the interface of the water, PMT glass, photocathode, and vacuum. The index of refraction of water and vacuum are set separately to 1.33 and 1.0 respectively. The laser data for wavelengths from 337-420 nm is fit to determine the effective index of refraction for each wavelength. These are used in the detector simulation.

Reflectivity of Black Sheet

A specialized laser injection system is used to measure the reflectivity of the black sheet surrounding the inner detector PMTs. This is done with light injector placed in the center of the SK tank. The injector points a laser with a variety of wavelengths at various incident angles on a sample of black sheet. The reflected light enters the SK tank and is measured by the detector PMTs. The laser injector can also be operated without the sample of black sheet to normalize the measurement. The ratio of the measured charge with and without the black sheet is the reflectivity of the black sheet, and is used in the detector simulation [59].

2.4 Neutrino Interactions at SK

Beam neutrinos are detected when they interact in the SK detector and produce charged particles. Neutrinos can interact either through charged current weak interactions mediated by the W^\pm , or neutral current weak interactions, mediated by the Z^0 . The cross section for charged current neutrino interactions as a function of energy is shown in Fig. 2.9 along with the world measurements of these cross sections [20]. As illustrated in this figure, there are three main types of charged current neutrino interactions: charged-current quasi-elastic, resonance, and deep inelastic scattering. Each of these will be discussed in more detail below.

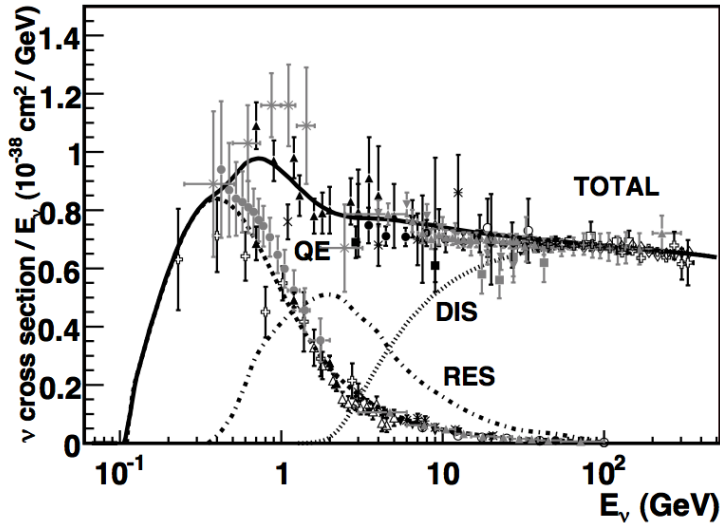


Figure 2.9: World neutrino interaction cross section data. Figure from [20].

2.4.1 Charged Current Quasi Elastic

Charged-current quasi-elastic (CCQE) interactions are dominant in the energy range of the T2K beam, around 600 MeV. These interactions occur when a neutrino of flavor l interacts with a neutron in the water to produce

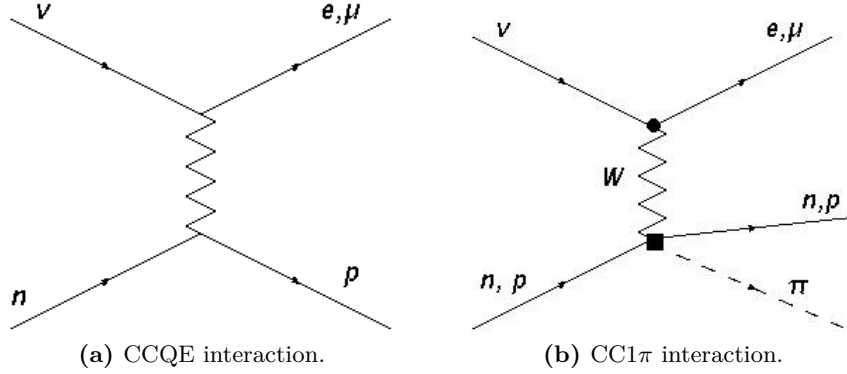


Figure 2.10: Feynman diagrams of common neutrino interactions at T2K neutrino energies.

a lepton and a proton:

$$\nu_l + n \rightarrow l^- + p, \quad (2.11)$$

as illustrated in Fig. 2.10a. At T2K l can be either an electron or a muon because the neutrino energy is typically below the tau production threshold. The proton in the CCQE interaction is almost always below the Cherenkov threshold, so these events are selected by looking for single electron or muon rings in the SK water. Since CCQE is a two body interaction, the neutrino energy E_ν can be calculated using only the lepton kinematics, as

$$E_\nu = \frac{m_p^2 - (m_n - E_b)^2 - m_l^2 + 2(m_n - E_b)E_l}{2(m_n - E_b - E_l + p_l \cos \theta_{l\nu})} \quad (2.12)$$

where m_n and m_p are the masses of the neutron and proton, $E_b = 27$ MeV is the binding energy of a nucleon in an ^{16}O nucleus, and E_l , p_l , $\theta_{l\nu}$ are, respectively, the energy, momentum, and angle between the direction of the incoming neutrino and outgoing lepton. This calculation assumes that the interaction happens with a bound nucleon at rest, and neglects the Fermi momentum of the nucleon within the nucleus.

2.4.2 Charged Current Single Pion

The second most dominant interaction at T2K beam energies is the charged-current single pion interaction (CC1 π), also known as “RES” in Fig. 2.9 because they typically come from resonances in the nucleus that decay into pions. The most common resonance at these energies is the $\Delta(1232)$. Interactions on protons produce the Δ^{++} resonance which decays to a proton and π^+ . Interactions on neutrons produce the Δ^+ resonance which may decay into either a neutron and π^+ or a proton and π^0 . This means that neutrinos can produce charged pions or neutral pions in these interactions:

$$\nu_l + p/n \rightarrow l^- + \pi^+ + p/n \quad (2.13)$$

$$\nu_l + n \rightarrow l^- + \pi^0 + p, \quad (2.14)$$

as illustrated in Fig. 2.10b, but are dominated by π^+ production. Negative pions are produced in anti-neutrino interactions.

Charged current resonance events that produce π^0 s are unlikely to produce backgrounds to the CCQE samples. These events will have three rings, one from the electron or muon and two from decay of the π^0 into photons. This means that it will be unlikely that the event will be single ring-like as the lepton and one of the photon rings will usually be visible. As the photons come from π^0 decay one of them is required to have energy that is at least half of the mass of the π^0 , which is a minimum of about 67 MeV.

The CC1 π^+ interactions can also be explicitly selected at SK to increase the number of signal events and reduce the backgrounds in the CCQE sample by using a combination of ring particle identification and decay electron counting. The focus of this thesis is the ν_μ CC1 π^+ interaction which produces positively charged pions and the details of the selection methods will be discussed in more detail in the following chapters.

2.4.3 Deep Inelastic Scattering

Deep inelastic scattering (DIS) events happen at high energy and occur on individual quarks within the nucleons as opposed to the nucleons themselves.

These interactions often produce multiple pions as well as other mesons in addition to the final state lepton. These are typically backgrounds to the CCQE and CC1 π^+ interaction channels. If all of the pions are below Cherenkov threshold these events may look CCQE-like or CC1 π^+ -like depending on how many decay electrons are produced. If only one pion is above Cherenkov threshold these events may look CC1 π^+ -like. These may also contribute to CCQE and CC1 π^+ backgrounds because of the final state interactions that pions undergo in the nucleus which may result in only zero or one pion leaving the nucleus after the interaction.

2.4.4 Neutral Current Interactions

Neutral current (NC) interactions occur through exchange of a Z^0 . An elastic NC interaction is:

$$\nu_l + p/n \rightarrow \nu_l + p/n. \quad (2.15)$$

Neutral current interactions also produce pions from excitation of Δ resonances within the nucleus:

$$\nu_l + p/n \rightarrow \nu_l + \pi^+ + p/n \quad (2.16)$$

$$\nu_l + n \rightarrow \nu_l + \pi^0 + p, \quad (2.17)$$

as in the CC1 π interactions. There are also high energy neutral current interactions that may produce multiple pions or other mesons.

Neutral current single pion (NC1 π^+) events are a background to the ν_μ CCQE selection because muon and pion rings can be very similar at SK, as illustrated in Fig. 2.7. These may also be a background to the CC1 π^+ selection if the pion scatters in the SK water and both rings are visible so that the event looks two ring-like despite the fact that only one particle is present. They may also be a background to the CC1 π^+ selection if both the pion and the proton are above Cherenkov threshold.

2.5 Simulation

The T2K experiment is simulated using a series of different models and packages described in the following sections.

2.5.1 Flux Prediction

The T2K flux as produced by the beam is simulated from the protons entering the secondary beamline to the target and finally to the decays in which the neutrinos are produced. The protons from the primary beamline and their interactions in the target are simulated using FLUKA [62]. The rest of the secondary beamline is simulated using a Geant3 simulation called JNUBEAM and with the GCALOR package from Geant3 used for hadronic interactions [63]. All of the hadronic interactions from JNUBEAM are saved for any hadron that eventually produces a neutrino. The hadron production that occurs in the target is reweighted to hadron production data from the NA61/SHINE experiments at CERN [64]. This hadron production data was taken on a 2 cm thin graphite target, and with the same beam energy as T2K. Data from a replica of the target used in the T2K secondary beamline has been taken and will be used in the future. Additional data, such as from the HARP experiment, is used to tune pion and nucleon interactions after the primary production process, such as from scattering in the horns. This reweighting improves upon the GCALOR model predictions by matching the flux prediction to hadron production measurements [65] [66].

2.5.2 Neutrino Interaction Generators

Neutrino interactions are simulated for a given neutrino flux and cross section as a function of neutrino energy using neutrino interaction generators. Each of a variety of neutrino interactions as defined in Section 2.4 are simulated with different probabilities depending on the neutrino flux and energy. There are several common neutrino interaction generators, each with different implementations of various neutrino interaction models. Some of these standard generators are NEUT [67], GENIE [68] and NuWro [69].

2.5.3 NEUT

The T2K experiment primarily uses the NEUT neutrino interaction generator to simulate neutrino interactions in the ND280 and SK detectors [67].

The neutrino cross sections calculated in NEUT assume that interactions occur on single nucleons within a nucleus and then these are summed to calculate the cross section. This requires the kinematics of the nucleons within the nucleus.

There are several nuclear models used in NEUT. The relativistic Fermi gas model is the simplest model of the nucleus. It assumes a flat distribution of initial nucleon momentum up to the maximum of the Fermi momentum. This corresponds to a constant nuclear density. The Spectral Function model describes the nuclear density as a two dimensional distribution of momentum and binding energy which is integrated over the volume of the nucleus.

NEUT by default uses the spectral function nuclear model to calculate CCQE interactions and the relativistic Fermi gas nuclear model to calculate charged current interactions that produce pions and all neutral current interactions. Due to discrepancies between the CCQE cross section calculated in NEUT with the spectral function nuclear model and external measurements of the CCQE cross sections, however, T2K currently uses the relativistic Fermi gas model for all neutrino interactions.

The relativistic Fermi gas model requires a value of the Fermi momentum and nuclear binding energy in the medium in which the neutrinos are interacting. The nuclear binding energy is the energy required to eject a nucleon from the nucleus, and is subtracted from the energy available after the neutrino interaction. These are obtained by fits to electron scattering data interpreted using the relativistic Fermi gas model. The reference values for binding energy and Fermi momentum on oxygen are found to be 27 MeV and 225 MeV/ c respectively [18] [21].

The CCQE differential cross section is calculated using the Llewellyn-Smith formalism [70]. Multi-nucleon correlations and nucleon-nucleon correlations such as 2p2h are simulated using the Nieves model [71].

CC1 π^+ interactions can happen either on nucleons or coherently with the

nucleus. Nucleon interactions are simulated with an implementation of the Rein-Sehgal model that assumes the pions come from excitation of a baryon in the nucleus [72]. There are 18 resonances included in this model and the probability of a final state is proportional to the sum of these contributions along with the probability that each nucleon will decay into a final state with a single nucleon and pion. NEUT uses the Rein-Sehgal implementation of the resonant axial mass and the value of the axial form factor at zero transferred four-momentum. The non-resonant contribution is modeled as suggested by Rein-Sehgal, using a Breit-Wigner amplitude. Modified form factors that focus on the $\Delta(1232)$ are used, because at T2K neutrino energies a $\Delta(1232)$ is the most commonly produced resonance. The angular distribution of pions is calculated using the Rein-Sehgal method for the $\Delta(1232)$ resonance and assumes an isotropic distribution in the resonance rest frame for the other resonances [73]. Some of the higher resonances may generate multi-pion production processes in addition to single pion production. This model is only used below 2 GeV of hadronic invariant mass. Coherent interactions are simulated with a different Rhein-Sehgal model assuming that the interactions happen on the nucleus as a whole instead of an individual nucleon [74].

There is a transition region above the $\Delta(1232)$ resonance in which there is a mixture of resonance production and deep inelastic scattering. This means that deep inelastic scattering interactions are simulated separately above and below 2 GeV of invariant hadronic mass. Above 2 GeV the Pythia/JetSet model is used [75]. As this model is tuned to high energies a combination of models are used below 2 GeV. Exclusive modes, such as the single pion discussed earlier, single kaon, and single eta are calculated separately. Events with more than one pion are generated with the Rein-Sehgal model for resonance production described earlier [18].

Particles that are produced in simulated neutrino interactions are propagated through the nuclear medium assuming a Woods-Saxon potential using a cascade model. The particles are simulated at a location within the nucleus, and then this model calculates the interaction probability of each particle at each step it takes towards exiting the nucleus. For the analysis

presented in this thesis these final state interactions (FSI) are most important in the T2K energy range for charged pions as they have the highest interaction probabilities. Pions with momentum below 500 MeV/ c can interact via absorption, charge exchange or scattering. These probabilities are calculated with the Oset *et. al.* model which uses a many body calculation in an infinite nuclear matter combined with a local density approximation [76]. Pions with momentum above 500 MeV/ c can also produce multiple hadrons or double charge exchange in a secondary interaction. These are modeled using fits to pion-proton and pion-deuteron scattering data [10] [18].

2.5.4 ND280 Detector Simulation

The ND280 Detector is simulated using a GEANT4 representation of the detector geometry. Models within GEANT4 are also used to simulate particles propagating in the detector and the detector response, such as scintillation light and MPPC response and associated electronics. All of the subdetectors are simulated in a single framework. Individual detectors may have their own reconstruction packages which are then integrated into a global event reconstruction.

2.5.5 SK Detector Simulation

The SK detector is simulated using a custom software package written by the Super-Kamiokande collaboration called SKDETSIM [18]. This package models the SK tank, water and PMTs and uses a combination of GEANT3 and custom models to propagate particles from their production at a neutrino interaction vertex and through the detector geometry [63]. The production and propagation of Cherenkov light is also modeled and takes into account processes such as absorption, Rayleigh scattering and Mie scattering. The laser calibration data as described earlier is used to calculate parameter inputs and tune the detector simulation so that it matches the SK water [18].

Pion Hadronic Interactions

Charged pions may re-interact in the SK water. These are called secondary interactions (SI). The SI that pions undergo in the water are modeled with the NEUT cascade model as described in Section 2.5.3 for pions with momentum less than 500 MeV/ c . They are modeled with the GCALOR package for pions with momentum greater than 500 MeV/ c [65]. Although FSI is a property of the neutrino interaction, and SI describes what happens in the detector, the NEUT cascade model is used in both the NEUT neutrino interaction generator and SKDETSIM to model pion hadronic interactions.

The hadronic interactions that charged pions undergo either in the nucleus or in the SK water can be described by the number and type of pions after the interaction. For positively charged pions these are defined as:

- Absorption: no pions after the interaction.
- Charge exchange: one π^0 after the interaction.
- Scattering: one π^+ after the interaction. There is both elastic and inelastic scattering, that, while modeled differently, produce the same topology in the SK detector.
- Double charge exchange: one π^- after the interaction.
- Hadron production: multiple pions of any charge after the interaction.

These definitions will be used throughout this thesis to discuss the interactions pions may undergo in the nucleus or in the SK water.

Chapter 3

PICCOLO

This thesis will focus on the identification of charged pions at SK. Most of the charged pions produced in neutrino interactions at SK are close to the Cherenkov threshold of $160 \text{ MeV}/c$ in momentum, as illustrated in the true momentum distribution for charged pions produced by $CC1\pi^+$ interactions in Fig. 3.1.

The PICCOLO (Pion Integrating Cylinder for Cherenkov Optics and Light Observation) detector was built to better understand the amount and properties of the Cherenkov light produced by pions close to the Cherenkov threshold, which may be different than for electrons and muons because of the pion hadronic interactions. This detector is an integrating water Cherenkov cylinder made out of PVC pipe with a 12 inch diameter and 1 m length displayed in Fig. 3.3. The inside of the cylinder is painted with white AvianD reflectance coating so the Cherenkov light produced will reflect off the walls of the detector, and be collected in one of four PMTs. Three 2 inch PMTs are located on top of the detector, and one 5 inch PMT is located opposite a 1 cm beam window. The detector set up is illustrated in Fig. ??.

Data was collected in the TRIUMF M11 secondary beam line which contains electrons, muons and charged pions. To scan the pion Cherenkov threshold data was collected in momentum steps of $5 \text{ MeV}/c$ from 130 to $200 \text{ MeV}/c$, and then more coarsely in $20\text{-}30 \text{ MeV}/c$ steps up to $300 \text{ MeV}/c$. Several data sets were collected at some of these momentum settings. The

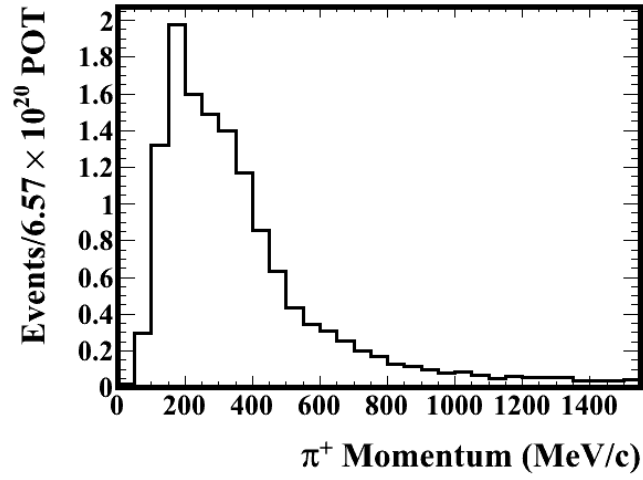


Figure 3.1: Momentum distribution of true CC1 π^+ events in the T2K-SK Monte-Carlo.



Figure 3.2: The PICCOLO detector.

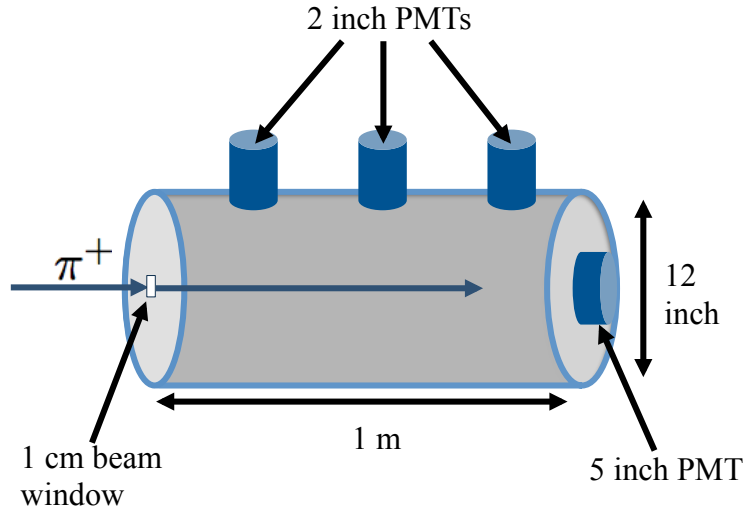
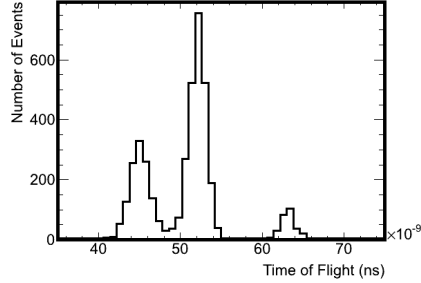


Figure 3.3: Schematic of the PICCOLO detector.

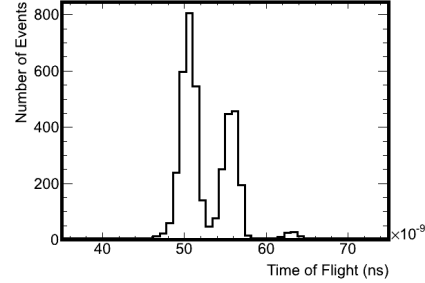
beam has approximately 2% momentum resolution. Each of the four PMT waveforms were read simultaneously on a LeCroy oscilloscope with 2 ns sampling of the PMT waveform over 5 μ s. Within this time it is possible to see primary PMT hits from the initial particle as well as decay electrons later in the waveform. Particles were detected in the PMT waveform using a custom peak finder. The single photoelectron peak of each of the four phototubes was calibrated for each data run by looking at all peaks in the waveforms after 4 μ s where there is the least contamination from decay electrons.

Particle identification (PID) was done using particle time of flight from production to the detector, as illustrated in Fig. 3.4. It becomes more difficult to separate the three particle types at higher energies, but the electron and muon fraction of the beam also drops off at higher energies, so above 200 MeV/c it is assumed that all of the beam particles are pions.

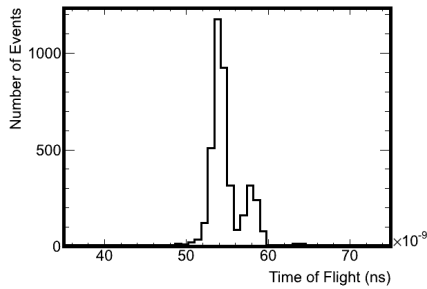
To test the efficacy of the detector and the data collection technique the muon lifetime was measured. As the beam was run with positively charged particles, no effects from muon capture are expected. Using the time of flight particle identification muons were identified, and then the peak finder was



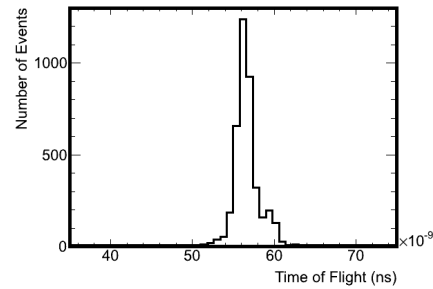
(a) 130 MeV/c.



(b) 160 MeV/c.



(c) 190 MeV/c.



(d) 220 MeV/c.

Figure 3.4: M11 beam composition at each of a range of momentum settings based on particle time of flight. The time difference between the accelerator and a scintillator in front of the PIC-COLO detector is plotted. Because of the way the difference is taken, electrons appear as the peak at the highest times, muons in the middle and pions at the shortest time.

used to select a decay electron peak. A plot of the decay times for muons is shown in Fig. 3.5, and when fit with an exponential the lifetime is measured as $2.21 \pm 0.04 \mu\text{s}$, which is consistent with the PDG lifetime of $2.197 \mu\text{s}$ [10].

In order to measure only the Cherenkov light that comes from the primary pion or muon, any contribution from late decay electron or dark noise light needs to be removed. This is done by looking at the starting time of a peak in the waveform that produces light. Below Cherenkov threshold the only visible light is from the decay electron, and the peak start times

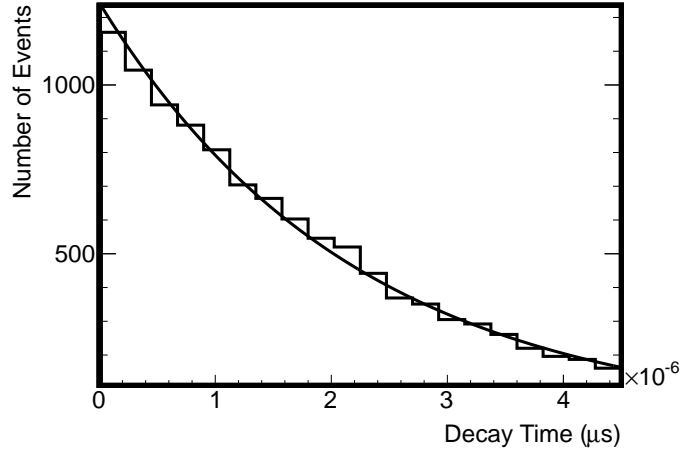
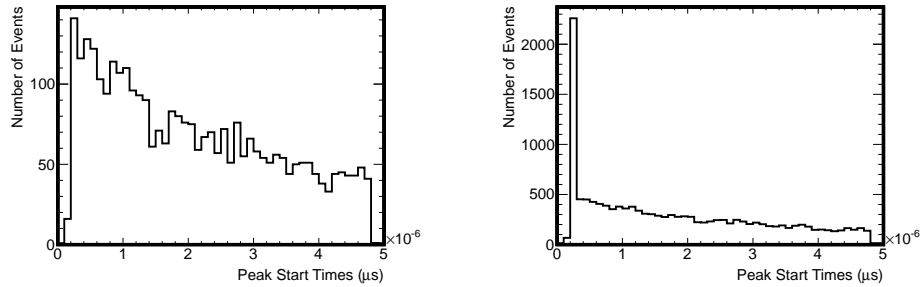


Figure 3.5: The muon lifetime as measured in the PICCOLO detector.

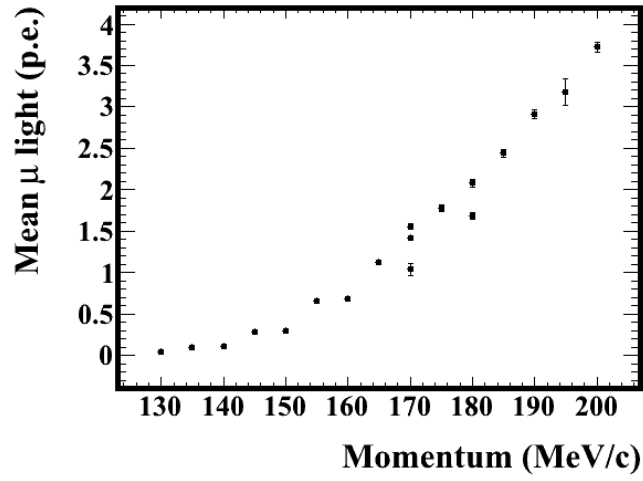


(a) Time that light emission begins for 130 MeV/c muons, at Cherenkov threshold. (b) Time that light emission begins for 180 MeV/c muons, above Cherenkov threshold.

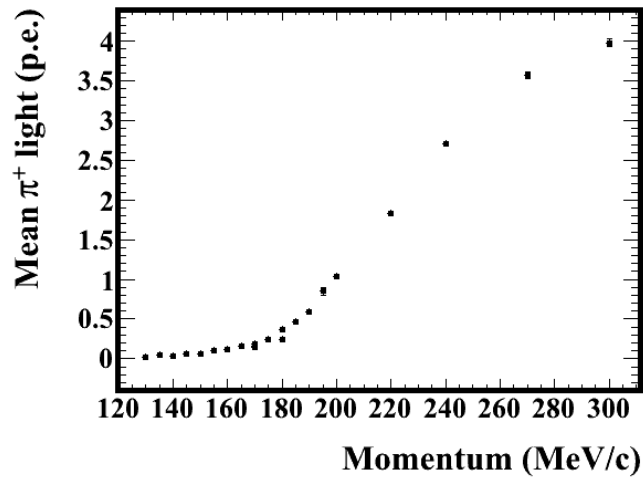
Figure 3.6: Time that light emission begins for muons in PICCOLO.

roughly follow the decay electron spectrum as illustrated in Fig. 3.6a. Above Cherenkov threshold there is a sharp peak in the distribution of the time that light is produced which corresponds to the light from the muon or pion, as illustrated in Fig. 3.6b. To look at only the light from the initial particle a cut is made on a 20 ns time window in light production times.

Looking only at this 20 ns time window, the mean amount of light produced by the initial muons and pions over the momentum range in which data was collected are shown in Fig. 3.7. It is possible to see evidence of the Cherenkov threshold in both cases. In particular, charged pions expend approximately as much Cherenkov light as expected, and there is evidence of the threshold at expected location of $160 \text{ MeV}/c$ in pion momentum. There was not enough light produced in this detector to do more detailed studies of the Cherenkov light emission model in SKDETSIM compared to the data and more extensively understand any threshold effects that come from pion hadronic interactions. It may be possible to study these effects more extensively in a future water Cherenkov beam test experiment such as the proposed NuPRISM Phase 0 beam test at Fermilab [77]. Future beam tests may also make use of the explicit charged pion reconstruction described in the next chapter to further understand the impact of hadronic interactions on the Cherenkov light production of charged pions in water.



(a) Light emitted by muons.



(b) Light emitted by charged pions.

Figure 3.7: PICCOLO results.

Chapter 4

SK Reconstruction

To extract the physics we are interested in from the SK detector we need to use the data recorded by the PMTs to determine which particles were produced and their kinematics. An event at SK is a set of times and charges recorded by each of the PMTs. These charges are clustered into sets of similar times and then arranged into “sub-events” which contain exactly one charge and one time per PMT. We then use a maximum likelihood algorithm called fitQun to extract the particle identification and kinematic quantities of interest.

4.1 Likelihood Function

fitQun is a maximum likelihood algorithm for the SK detector. It was inspired by the event reconstruction used for the MiniBooNE detector [3], and uses the times and charges recorded on each of the 11,129 PMTs in the SK inner detector to determine what happened in an event.

The quantities that we are interested in reconstructing are the number of particles in an event, which particles there are in an event (particle identification), and the location and kinematics of each of these particles. It is simplest to start by looking at how to reconstruct a single particle, and then the method will be generalized to include multiple particles. One particle can be defined in terms of eight track parameters: vertex position (x, y, z)

and time, momentum, direction (θ, ϕ) , and the energy lost along the particle track. Collectively these track parameters are called \mathbf{x} .

A likelihood function can be written in terms of these track parameters as:

$$L(\mathbf{x}) = \prod_{i=1}^{N_{\text{unhit}}} \mathcal{P}_i(\text{unhit}; \mathbf{x}) \prod_{j=1}^{N_{\text{hit}}} \mathcal{P}_j(\text{hit}; \mathbf{x}) f_q(q_j; \mathbf{x}) f_t(t_j; \mathbf{x}). \quad (4.1)$$

Here, N_{hit} is the number of hit PMTs in the event, and N_{unhit} is the number of unhit PMTs in the event. The likelihood is constructed as the product of the probability that a given PMT will be hit or unhit for the hypothesized particle type and track parameters. Each of the 11,129 inner detector PMTs is assumed to be either hit or unhit such that $N_{\text{hit}} + N_{\text{unhit}} = 11,129$ PMTs. $\mathcal{P}_i(\text{unhit}; \mathbf{x})$ is the probability that PMT i will be unhit for a given set of track parameters \mathbf{x} and $\mathcal{P}_j(\text{hit}; \mathbf{x})$ is the probability that PMT j will be hit for the same set of track parameters. The unhit probability can be written in terms of the hit probability as $\mathcal{P}_i(\text{unhit}; \mathbf{x}) = 1 - \mathcal{P}_i(\text{hit}; \mathbf{x})$. For the PMTs that are hit there is a charge and time likelihood $f_q(q_j; \mathbf{x})$ and $f_t(t_j; \mathbf{x})$ specific to the track parameters \mathbf{x} . These charge and time profiles are evaluated at the measured charge q_j and time t_j at PMT j respectively.

It is easiest to find the best likelihood, and the track parameters that go along with this likelihood, by working with the negative of the log likelihood instead of the likelihood itself. Working with the negative of the likelihood makes it possible for us to use existing minimization algorithms. Using the logarithm of the likelihood makes it possible to break it up into time and charge components.

In this formulation the time and charge likelihoods can be fully separated as:

$$\mathcal{L}_q(\mathbf{x}) = \sum_{i=1}^{N_{\text{unhit}}} \log(\mathcal{P}_i(\text{unhit}; \mathbf{x})) + \sum_{j=1}^{N_{\text{hit}}} \log(1 - \mathcal{P}_j(\text{unhit}; \mathbf{x}) f_q(q_j; \mathbf{x})) \quad (4.2)$$

$$\mathcal{L}_t(\mathbf{x}) = \sum_{j=1}^{N_{\text{hit}}} \log(f_t(t_j; \mathbf{x})), \quad (4.3)$$

and the full likelihood written as $\mathcal{L} = -\mathcal{L}_q - \mathcal{L}_t$. The negative log likelihood is minimized for a given set of track parameters \boldsymbol{x} , as well as recorded times and charges to determine the type of particle and its track parameters for a given event.

4.2 Charge Likelihood

It is possible to calculate the charge likelihood by decoupling the propagation of particles in the detector and the emission of Cherenkov photons from the PMT response and associated electronics by introducing a quantity called the predicted charge. The predicted charge is defined as the average number of photoelectrons that a PMT will observe for a given particle hypothesis and set of track parameters and is written at the i th PMT as μ_i . It is possible to calculate the predicted charge for a given set of track parameters \boldsymbol{x} using what is known from simulation and calibration data about the particle propagation, Cherenkov light emission, and detector response. This is done separately for each type of particle that is reconstructed, and the details will be described in the next section.

Using this mapping between track parameters \boldsymbol{x} and predicted charge μ_i the charge likelihood can be written only in terms of the detector response:

$$\mathcal{L}_q(\mu) = \sum_{i=1}^{N_{\text{unhit}}} \log(\mathcal{P}_i(\text{unhit}; \mu_i)) + \sum_{j=1}^{N_{\text{hit}}} \log(1 - \mathcal{P}_j(\text{unhit}; \mu_j) f_q(q_j; \mu_j)). \quad (4.4)$$

With this definition of the likelihood, the unhit probability of a given PMT should be Poisson with a mean of the predicted charge μ :

$$\mathcal{P}_i(\text{unhit}; \mu_i) = e^{-\mu}. \quad (4.5)$$

Due to the PMT threshold, however, not all photoelectrons produced will necessarily result in a PMT hit. To correct for this effect the unhit probability is expanded in predicted charge as:

$$\mathcal{P}_i(\text{unhit}; \mu_i) \approx (1 + a_1 \mu_i + a_2 \mu_i^2 + a_3 \mu_i^3) e^{-\mu_i}, \quad (4.6)$$

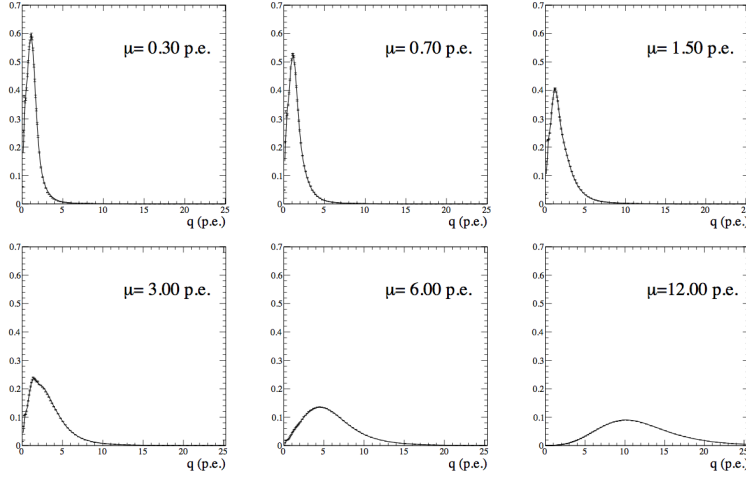


Figure 4.1: Charge probability distribution functions $f_q(q; \mu)$ at a variety of predicted charges μ . The data points are the output of the simulation, and the line is the fitted function used to evaluate the likelihood. Diagram from [4].

with the a coefficients extracted from the detector simulation. This is found to better replicate the detector simulation than the Poisson probability alone.

Finally the charge probability distribution function $f_q(q; \mu)$ is calculated by simulating photons in the detector that have a range of predicted charge μ , and looking at the distribution of measured charge for the hit PMTs as illustrated in Fig. 4.1. These charge distributions are normalized and fit with a polynomial that is a function of predicted charge μ at each value of measured charge q . The likelihood is evaluated for a given measured charge q by linearly interpolating between the values closest to the measured charge, and evaluating the result at the predicted charge μ .

This method requires calculating the predicted charge for a given particle hypothesis and set of track parameters before the charge likelihood can be evaluated with the measured charges.

4.2.1 Predicted Charge

The predicted charge contains two main components, light that travels directly from emission to a PMT, and indirect light which scatters or reflects in the detector before reaching a PMT. For a given particle track the predicted charges for direct and indirect light are calculated separately, and then added together to put into the likelihood calculation. The calculation of the direct and indirect predicted charges for a particle hypothesis and set of track parameters is described here.

The predicted charge from direct and indirect light are both a function of the light emission point relative to the PMT that the light hits. Both are expressed as integrals along the track length of the particle, s .

The predicted charge for direct light is:

$$\mu_{\text{dir}} = \Phi(p) \int g(p, s, \cos \theta) \Omega(R) T(R) \epsilon(\eta) ds. \quad (4.7)$$

As illustrated in Fig. 4.2, R is the distance from the light emission point to the PMT, θ is the angle between the particle direction relative to R , and η is the angle between the PMT normal and R . p is the initial momentum of the particle. The functions that make up this integral define the light emission and propagation along with the phototube acceptance and response. The light that is emitted by a particle traveling in the SK detector is described with the Cherenkov emission profile $g(p, s, \cos \theta)$. The amount that light attenuates due to absorption and scattering in the water is described by $T(R)$. Finally the Cherenkov light acceptance by the PMT is described by two factors: the solid angle covered by the PMT face $\Omega(R)$, and the angular acceptance of the PMT $\epsilon(\eta)$. There is also a normalization term $\Phi(p)$ which represents the number of photons and absorbs the constant factors across the Cherenkov light emission, propagation and PMT acceptance such as the average number of photons produced by a particle with initial momentum p and the PMT quantum efficiency.

The predicted charge for indirect light is:

$$\mu_{\text{indir}} = \Phi(p) \int \Omega(R) T(R) \epsilon(\eta) A(s) \left[\int \frac{1}{4\pi} g(p, s, \cos \theta) \sin \theta d\theta d\phi \right] ds. \quad (4.8)$$

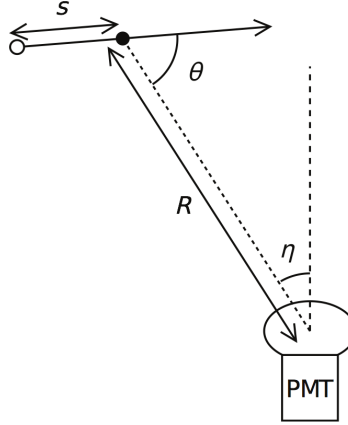


Figure 4.2: Variables used in calculation of predicted charge. The initial particle production is indicated by the white dot, and the point of light emission, s , is indicated by a black dot. Diagram from [4].

Note that the expression for the direct and indirect predicted charges are the same except for the factor $A(s)$ which describes the light that is produced by scattering in the water or reflections from the PMT glass and black sheet.

The calculation of each of the factors in the integrals in Eq. 4.7 and 4.8 will be described in the following sections.

Cherenkov Emission Profile

The Cherenkov emission profile $g(p, s, \cos \theta)$ describes the light that is emitted by a particle traveling in the SK detector. More specifically it is a function that gives the number of photons that are emitted at angle θ along the path of a particle with initial momentum p and that has traveled a distance s . The emission profile is normalized so that

$$\int g(p, s, \cos \theta) ds (\sin \theta d\theta d\phi) = 1. \quad (4.9)$$

The normalization corresponding to the total number of detected photons is absorbed into $\Phi(p)$ in Eq. 4.7 along with the other normalizations described

earlier.

The Cherenkov emission profile is calculated by generating particles of each type that we plan to reconstruct: electrons, muons, charged pions, protons, kaons, and gammas, at discrete initial momenta using the SK detector simulation. Plots of these emission profiles for electrons and muons at several momenta are shown in Fig. 4.3. The emission profiles are displayed as a function of the position at which light is emitted, s , and the Cherenkov angle, θ . These plots illustrate that the Cherenkov light emitted by electrons and muons looks very different. For electrons the peak of the Cherenkov angle emission tends to be the same as that of a particle with $v = c$. Muons have a more obvious cone collapse as they travel in the detector. Electrons also tend to have a wider angular profile compared to muons, as they produce electromagnetic showers in the detector. Differences like these in the Cherenkov emission profile are used to do particle identification on the rings that the reconstruction identifies.

Light Transmission

The function $T(R)$ corresponds to the amount that light attenuates as a result of absorption and scattering in the water. It is parameterized in terms of the attenuation length in the SK water, L_{att} . The attenuation length was calculated in the detector simulation by generating samples of 100 simultaneously produced 3 MeV electrons from a single vertex and at random directions to approximate a point source of Cherenkov light. This was done in two special configurations of the detector simulation. One mode consists of direct light only, so any light that would have scattered or reflected is instead absorbed, and the other is perfect transmission, which does not allow any light to be scattered, absorbed, or reflected. These samples were generated in a line across the vertical center of the detector and plotted as a ratio of the number of photons in the direct light sample to those in the perfect transmission sample. The results are fit to an exponential, and

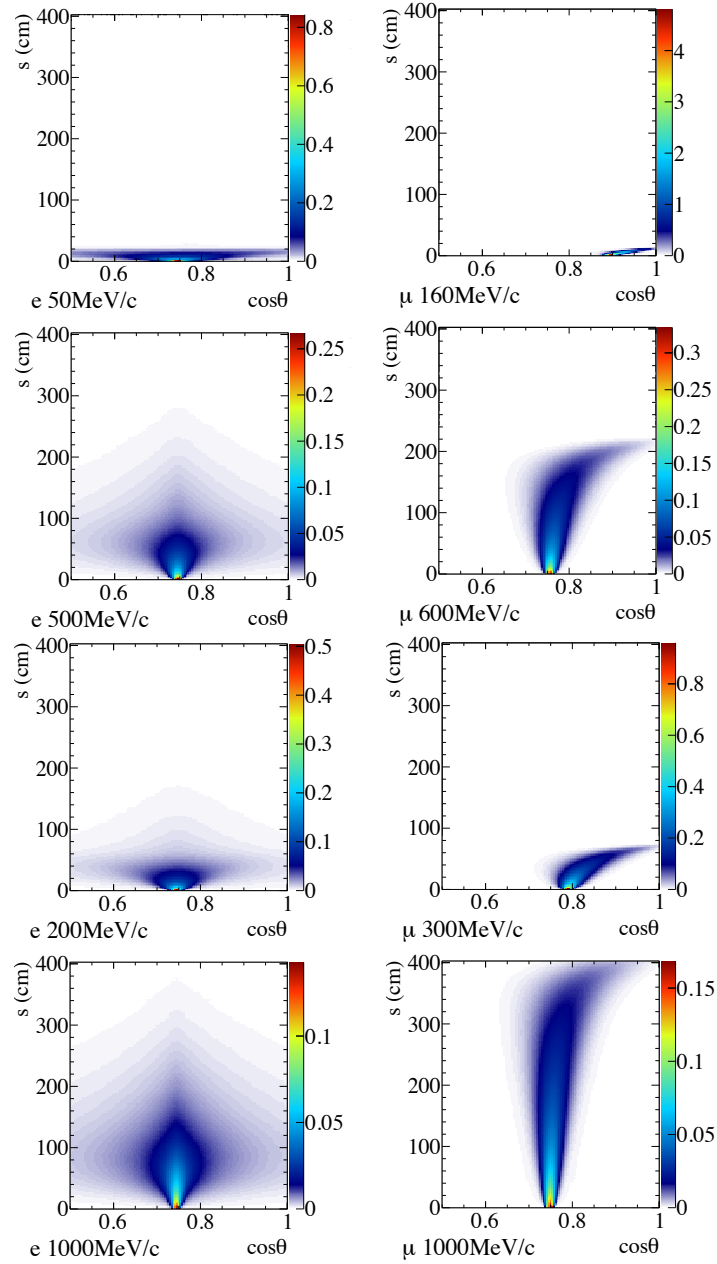


Figure 4.3: Example charge profiles for electrons (left) and muons (right) as a function of the position at which light is emitted s , and the Cherenkov angle. Figure adapted from [4].

defined as the transmission function given by

$$T(R) = \exp\left(\frac{-R}{L_{\text{att}}}\right). \quad (4.10)$$

The attenuation length as measured by this method was determined as $L_{\text{att}} = 72.96$ m.

Solid Angle

The solid angle factor $\Omega(R)$ corresponds to the geometric area presented by the active detector surface as viewed from a point R , assuming that all of the light is perpendicularly incident. It is calculated as the solid angle covered by a PMT when viewed perpendicularly at a distance R from the center of the phototube, assuming that the PMT is a flat circular object:

$$\Omega(R) = \frac{\pi a^2}{R^2 + a^2} \quad (4.11)$$

where a is the radius of a PMT ($a=25.4$ cm). The assumption that the PMT is a flat circular object holds sufficiently well at distances $R>1$ m.

PMT Angular Acceptance

The function $\epsilon(\eta)$ is the PMT angular acceptance. This corresponds to how much the light a phototube collects is reduced if the light is not perpendicularly incident on the phototube as assumed in $\Omega(R)$. The incident angle η is between the direction perpendicular to the PMT surface and the particle direction. The acceptance function as calculated from the detector simulation is shown in Fig. 4.4. The detector simulation output is fit to a piecewise continuous polynomial and the result is used as $\epsilon(\eta)$. It is approximated that the angular acceptance can only reduce the total amount of light detected by a PMT, so the angular acceptance function is normalized to 1 for the perpendicular light calculated by the solid angle factor.

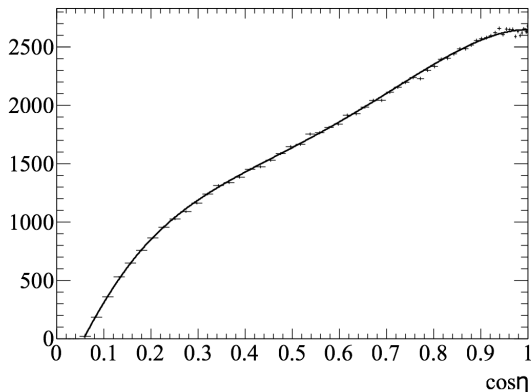


Figure 4.4: PMT acceptance output from SKDETSIM. The vertical axis has arbitrary units, and the normalization is set so that $\epsilon(\cos \eta = 1) = 1$. Diagram from [4].

Scattering Table

The additional factor present in the predicted charge integral for scattered light is the scattering table, which is calculated as the ratio of the differential predicted charge from scattered light to that of isotropic direct light:

$$A(s) = A(x_{PMT}, z_{vtx}, R_{vtx}, \varphi, \theta, \phi) = \frac{d\mu_{scat}}{d\mu_{dir}}. \quad (4.12)$$

The isotropic direct light in the denominator is the same as that considered in the direct light predicted charge. Assuming that the Cherenkov angle does not change as the particle propagates and loses energy, and taking the ratio as above, it is possible to factor out the momentum dependence in the scattering table. This allows one table to be used for all particles across all momenta.

The scattering table is parameterized in terms of six variables that describe the PMT and particle locations relative to each other. These are illustrated in Fig. 4.5. It was calculated by simulating 3 MeV/ c electrons at random positions in the SK detector. The output is filled in a six dimensional histogram. When a fit is run $A(s)$ is calculated for the indirect charge prediction by linearly interpolating between the six dimensions of this table.

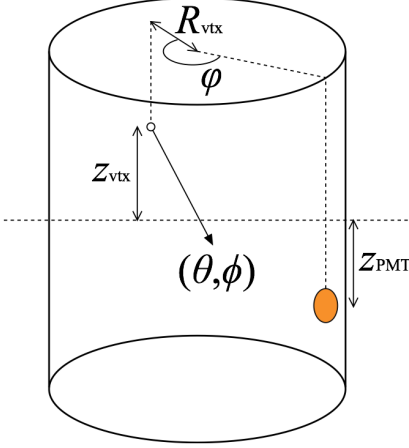


Figure 4.5: Variables used to parameterize the six dimensional scattering table for PMTs on the walls of the detector. Diagram is the same for PMTs on the top and bottom of the tank except that R_{PMT} , which is not illustrated, is used instead of z_{PMT} . Diagram from [4].

4.2.2 Calculation of Charge Likelihood

With the predicted charge fully defined as described above, it is possible to calculate the charge likelihood using the measured charges for each phototube.

Parabolic Approximation of Predicted Charge Calculation

The integrals required to calculate the predicted charge must be evaluated multiple times for every PMT in an event. This is computationally impractical in a reconstruction algorithm, so these integrals are pre-calculated and stored in lookup tables. This is done using the fact that the part of the predicted charge integral that describes the PMT acceptance usually varies slowly as a function of the light emission point relative to the PMT, s . This means that it can be approximated with a parabola as follows:

$$J(s) \approx j_0 + j_1 s + j_2 s^2. \quad (4.13)$$

The function $J(s)$ combines the PMT solid angle, $\Omega(R)$, the water transmission function $T(R)$ and the PMT angular acceptance $\epsilon(\eta)$ into a single function in terms of the distance s .

With this approximation the predicted charge from direct light in Eq. 4.7 simplifies to:

$$\begin{aligned}\mu_{dir} &= \Phi(p) \int_{-\infty}^{\infty} g(p, s, \cos \theta) J(s) ds \\ &\approx \Phi(p) \left[j_0 \int_{-\infty}^{\infty} g(p, s, \cos \theta) ds \right. \\ &\quad + j_1 \int_{-\infty}^{\infty} g(p, s, \cos \theta) s ds \\ &\quad \left. + j_2 \int_{-\infty}^{\infty} g(p, s, \cos \theta) s^2 ds \right]\end{aligned}\tag{4.14}$$

The coefficients j_0 , j_1 , j_2 can be calculated by evaluating $J(s)$ at three different points along the track: the initial position ($s = 0$), the point at which 90% of the particle's Cherenkov light has been emitted, and halfway between these two points. This approximation is found to well approximate the full integral.

The scattering table $A(s)$ also varies slowly in s , so this approximation can be extended for indirect light. This is done by approximating:

$$J(s)A(s) \approx k_0 + k_1 s + k_2 s^2\tag{4.15}$$

This makes it possible to write the indirect predicted charge in Eq. 4.8

as:

$$\begin{aligned}
\mu_{dir} &= \Phi(p) \int_{-\infty}^{\infty} g(p, s, \cos \theta) J(s) A(s) ds \\
&\approx \frac{\Phi(p)}{4\pi} \left[k_0 \int_{-\infty}^{\infty} g(p, s, \cos \theta) \sin \theta d\theta d\phi ds \right. \\
&\quad + k_1 \int_{-\infty}^{\infty} g(p, s, \cos \theta) \sin \theta d\theta d\phi s ds \\
&\quad \left. + k_2 \int_{-\infty}^{\infty} g(p, s, \cos \theta) \sin \theta d\theta d\phi s^2 ds \right]
\end{aligned} \tag{4.16}$$

and k_0 , k_1 , k_2 can be calculated in the same way as the direct light j_i coefficients.

The remaining integrals are over the Cherenkov profile for direct and indirect light as:

$$I_{dir}(n) = \int_{-\infty}^{\infty} g(p, s, \cos \theta) s^n ds \tag{4.17}$$

$$I_{scat}(n) = \int_{-\infty}^{\infty} g(p, s, \cos \theta) \frac{\sin \theta d\theta d\phi}{4\pi} s^n ds. \tag{4.18}$$

These integrals are calculated in advance for a set of parameters that define the initial conditions of the particle and the relative orientation to the PMT. These are, as illustrated in Fig. 4.2, the initial momentum of the particle, the initial distance R from the particle to the PMT, and the angle θ between the direction of the particle and the line connecting the initial position of the particle and the PMT. The results of these integrals for discrete sets of these three parameters are fit as a function of initial particle momentum for each value of R and θ . During the event reconstruction the integral calculation is done by first evaluating it at a given initial momentum for the two closest tabulated values of R and θ , and then the results are linearly interpolated. The results can then be used as the predicted charge needed to calculate the charge likelihood.

4.3 Time Likelihood

The time likelihood $\mathcal{L}_t(t_i|\mathbf{x})$ depends on the track parameters \mathbf{x} as well as the position of the i th PMT. Calculation can be simplified by introducing a corrected time t_i^c that depends on the initial position and direction of the particle and the relative location of the hit PMT. This corrected time removes some of the dependence on the track parameters \mathbf{x} that comes from just using the raw hit time t_i , because it makes it possible to parameterize the time likelihood in three dimensions as a function of only the track momentum, and the direct and indirect predicted charge.

The corrected time is calculated by assuming that all of the light from the particle comes from the center of the particle track. Then the corrected time is defined by subtracting the starting time of the track, the time for the particle to propagate from the start point to the midpoint of the track, and the time for light to travel from the midpoint of the track to the PMT from the measured time t_i :

$$t_i^c = t_i - t_0 - \frac{s_{\text{mid}}}{c} - \frac{|\mathbf{x}_i^{\text{PMT}} - (\mathbf{x}_0 + s_{\text{mid}}\mathbf{d})|}{c_n}. \quad (4.19)$$

Here, t_0 is the starting time of the particle track. The term $\frac{s_{\text{mid}}}{c}$ is the time it takes the particle to travel from its starting point to the track midpoint s_{mid} , assuming that the particle's velocity is close to c . The midpoint of the track is calculated using the track energy. The final term is the time it takes light to travel from the track midpoint to the PMT. This depends on the distance of the i th PMT from the track midpoint, which is calculated using the midpoint of the particle track s_{mid} , the distance from the starting point of the track to the i th PMT $\mathbf{x}_i^{\text{PMT}}$, the starting position of the track \mathbf{x}_0 , and the direction of the particle \mathbf{d} . Light travels from the center of the track to the PMT at the group velocity of the Cherenkov photons in water, or $c_n = c/n$ where $n = 1.38$.

Calculation of the time likelihood can be simplified by assuming that the corrected time likelihood only depends on the momentum of the particle

and the predicted charge. The dependence on which particle is producing light and the properties of the PMT response are included in the predicted charge. The predicted charge dependence is broken into direct and indirect components where the direct component comes from the direct charge prediction and indirect from the indirect charge prediction. The direct light arrives promptly, whereas indirect light arrives later due to the fact that it has been scattered or reflected. Varying these separately makes it possible to vary the ratio of prompt and late times that light reaches the PMT in the time likelihood. After being calculated separately the direct and indirect time likelihoods are combined to produce the final time likelihood.

Assuming that an indirect photon can only provide a hit at PMT i if no direct light reached this PMT then the direct and indirect time likelihoods can be combined as

$$\mathcal{L}_t(t_i^c) = w\mathcal{L}_t^{dir}(t_i^c) + (1 - w)\mathcal{L}_t^{sct}(t_i^c). \quad (4.20)$$

Here w is the weight given to the direct light distribution and $1 - w$ is the weight given to the late light distribution. The probability that there are no direct or indirect light hits is the Poisson probability of drawing zero with a mean value of the predicted charge. This means that w , the probability that a hit has at least one prompt photoelectron is calculated as

$$w = \frac{1 - e^{-\mu^{dir}}}{1 - e^{-\mu^{dir}} e^{-\mu^{sct}}}. \quad (4.21)$$

The time likelihood is calculated at each step in the likelihood minimization.

4.3.1 Time Likelihood from Direct Light

The direct time likelihood for the corrected time t_i^c defined above is assumed to be a Gaussian and depend only on the predicted charge from direct light μ_{dir} and the initial momentum of the particle. A hit typically incorporates all the light that reaches a PMT in association with an event, but only one time, which corresponds to when the first photon to reach a PMT is

registered. This means that as there are more photons the width of the corrected time distribution will decrease. Similarly, the particle momentum is related to the width of this distribution because the longer the track the more possible photon production times there are, which means that the calculation of the amount of time that it takes a photon to reach a PMT built into the corrected time definition will become less accurate.

Corrected time distributions can be generated using MC samples of each particle type at a range of fixed momentum values. Using these samples a two dimensional histogram in corrected time t_c and predicted charge from direct light $\log(\mu_{\text{dir}})$ is filled for all PMT hits from direct light at each momentum. Each bin of predicted charge is fit as a Gaussian distribution in corrected time. The resulting mean and standard deviations for each predicted charge bin are fit as a sixth order polynomial. Then each of the resulting polynomial fit parameters are fit as a function of initial particle momentum. This parameterizes the direct time likelihood as a function that depends only on the predicted charge and particle momentum. An example of this parameterization compared to the raw output of the simulation is shown for 450 MeV/c muons and a range of predicted charge in Fig. 4.6.

4.3.2 Time Likelihood from Indirect Light

The indirect time likelihood is modeled as the following formula that follows the typical shape of the corrected time distribution from indirect light:

$$\mathcal{L}_t^{\text{sct}} = \frac{1}{\sqrt{\pi/2\sigma + 2\gamma}} \times e^{-\tau^2/2\sigma} \quad \text{for } \tau < 0 \quad (4.22)$$

$$\frac{1}{\sqrt{\pi/2\sigma + 2\gamma}} \times \left(\frac{\tau}{\gamma} + 1\right) e^{-\tau/\gamma} \quad \text{for } \tau > 0. \quad (4.23)$$

Here, $\tau = t_c - 5$ ns, $\sigma = 8$ ns, and $\gamma = 25$ ns. The long tail at late times corresponds to reflected light. The predicted charge and momentum dependence are not taken into account in this calculation.

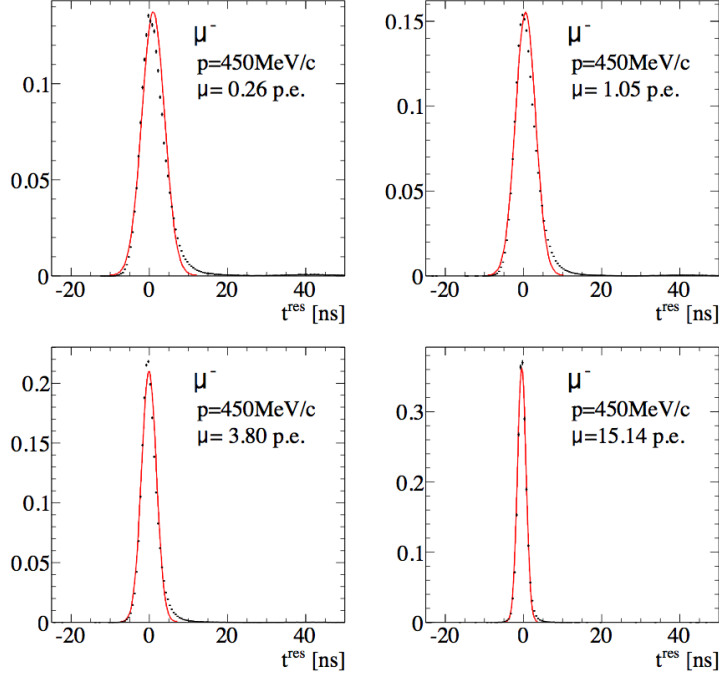


Figure 4.6: Time likelihood from direct light for 450 MeV/c muons and a range of predicted charge. The data points indicate the raw simulation output and the red curve is the final fit output assuming that the likelihood depends only on the predicted charge and particle momentum. Diagram from [4].

4.4 Sub-Event Algorithm

A SK event is defined as any PMT hits in a time window of order $10\ \mu\text{s}$ around an event trigger. These hits are clustered into groups of similar times, and then these clusters are arranged into subevents which contain one charge and one time per PMT. The likelihood algorithm described above is run on each of these subevents. Typically the first subevent contains the primary particles from a neutrino interaction, and subsequent subevents contain activity that is separate or delayed. This delayed activity is often a result of decay electrons that come from muons and pions produced in neutrino interactions. These are well separated in time as the muon lifetime

is about $2 \mu\text{s}$. The timing resolution of the SK detectors is about 3 ns [19].

4.4.1 Vertex Pre-Fitter

The vertex prefitter uses the hit times of the PMTs to estimate the vertex position and time (\mathbf{x}, t) . This is done by looking for the (\mathbf{x}, t) that maximizes the vertex goodness assuming that a point light source is emitted at the vertex:

$$G(\mathbf{x}, t) = \sum_i^{\text{hit}} \exp \left(\left(-\frac{t_i^{c(\text{point})}}{\sigma} \right)^2 / 2 \right), \quad (4.24)$$

where

$$t_i^{c(\text{point})} = t_i - t_0 - \frac{|\mathbf{x}_i^{\text{PMT}} - \mathbf{x}_0|}{c_n}. \quad (4.25)$$

For values close to the true vertex $t_i^{c(\text{point})}$ is close to zero, which results in large values of the goodness. Maximization of the goodness is done with a grid search in \mathbf{x} and t . The grid search calculates the goodness for a grid of allowed vertex positions and times, and the grid point at which the goodness is best is considered the best fit. Then the goodness is minimized using the Simplex algorithm in MINUIT [78]. This is done on all of the hits in the event to quickly find a seed for the vertex position and time.

4.4.2 Subevents

Possible subevents are first identified with a peak finder. This is done by fixing the vertex position at the output of the vertex prefitter and then scanning the goodness function while varying the time. Subevents appear as peaks in the goodness distribution, assuming that the true vertex positions are close to the prefit values.

Time windows are defined around each peak. Only one hit per PMT is allowed within the peak. To calculate the time windows first the corrected time as defined in Eq. 4.25 is calculated for each measured time t_i within a

peak. The hits that are earliest and latest in terms of corrected time, and that also fall within a window of $180 \text{ ns} < t_i^{c(\text{point})} < 800 \text{ ns}$ are called a time window.

The time windows are defined by calculating the corrected time as defined in Eq. 4.25 for each measured time t_i within a peak and looking for the earliest and latest hits that fall within a window of $-180 \text{ ns} < t_i^{c(\text{point})} < 800 \text{ ns}$. Any time windows that overlap are combined.

Finally the vertex pre-fitter and the peak finder are rerun on each of the time windows to define the subevents on which the full likelihood reconstruction algorithm is applied.

4.5 One Ring Fits

The full likelihood as defined in Eq. 4.1 is minimized for each subevent to find the track parameters \boldsymbol{x} for a given subevent. This is done sequentially for each of the one ring particle hypotheses: electron, muon, and charged pion, with a separate Cherenkov profile used for each. The SIMPLEX algorithm in MINUIT is used to do the minimization [78].

The electron fit is run first. The vertex is seeded with the output of the vertex pre-fitter. The direction is seeded with a likelihood scan of points equally spaced on a unit sphere with the momentum fixed to an estimate that comes from the total event charge. The momentum is seeded with another likelihood scan at the direction found in the earlier step. Once these seeds have been determined the fit is done by minimizing the negative log likelihood.

The muon fit is seeded with the vertex and direction result from the electron fit, and uses a grid search to seed the momentum. Fit results are obtained by minimizing the negative log likelihood with these seeds.

4.5.1 Upstream π^+ Fit

Charged pions and muons have similar masses, $139 \text{ MeV}/c^2$ and $105 \text{ MeV}/c^2$ respectively, which means that their charge profiles in SK will be similar [10], as illustrated by the rings in Fig. 2.7. Unlike muons, however, charged pions

can undergo hadronic interactions, and these can be used to separate them from muons. These hadronic interactions mean that a pion may abruptly stop emitting light because it has either been absorbed in the water or lost enough energy in a hadronic scatter to fall below Cherenkov threshold. When this occurs a pion will produce a sharp thin ring. Muons, however, tend to generate Cherenkov light continuously until they fall below Cherenkov threshold. Pion tracks are defined in relation to their hadronic interactions, where the portion before the interaction is called the “upstream track”, and after the interaction is called the “downstream track”, as illustrated in Fig. 4.7. The upstream π^+ fit only considers light that is produced by the upstream segment, before a hadronic interaction.

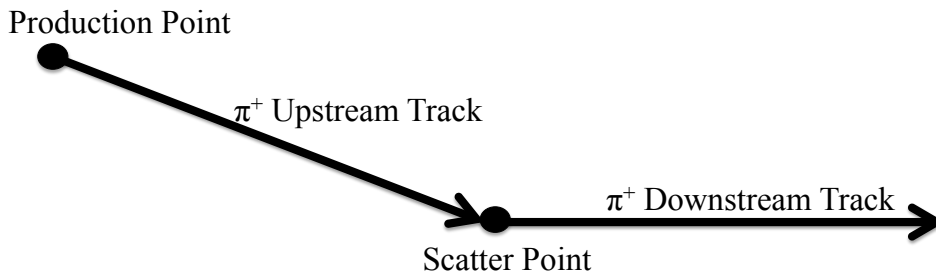


Figure 4.7: Pion hadronic scatter.

This effect, in which pions abruptly stop generating light, can be built into the one ring fit algorithm by defining a parameter that indicates how much energy the pion has lost from where it started to where it interacts. Using this parameter, and assuming that a pion expends energy at a constant rate along the track length, it is possible to calculate the position and momentum of the pion at its interaction point. Then two separate charge predictions are combined to create a pion track. The first, which is called the “full track”, uses the initial momentum of the pion and assumes that it expends all of its energy traveling in the water. The second, called the “anti-track”, uses the pion momentum at its interaction point and represents the energy the pion would have expended if it continued to travel in the water. A charge prediction for the pion before an interaction is created

by subtracting these two charge predictions. These three components of the track are illustrated in Fig. 4.8. The upstream pion fit is done for all of the standard track parameters \boldsymbol{x} , as well as for the energy loss along the pion track. This fit is done after the one ring electron and muon fits, and uses the one ring muon fit as a seed.

4.6 Generic Multi-Ring Fit

The one ring fits described above can be generalized to fit for topologies with multiple rings by adding their charge predictions. fitQun contains a generic multi-ring fitter that can look for events with up to six rings.

Initially the rings in multi-ring events are assumed to be either electron-like or upstream pion-like. The sharp rings produced by muons and pions are distinct from the “fuzzy” rings produced by electron showers in the SK water. The upstream pion-like hypothesis mostly encompasses the muon hypothesis because of the similarity of their Cherenkov profiles. In the absence of hadronic interactions, when the energy loss along the track of the pion is the maximum allowed, pions and muons will appear to be almost identical.

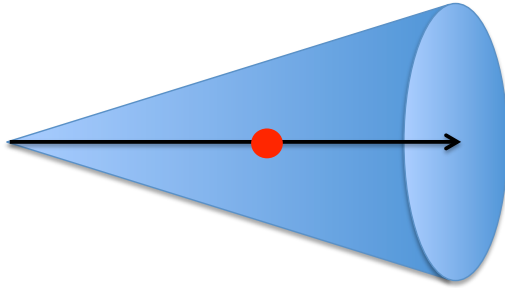
The multi-ring fit starts with either the one ring electron-like or the one ring pion-like fit output. Then another ring that is electron-like or pion-like, and comes from the same vertex is added. A fit is done to calculate the likelihood for the new hypothesis. All possible two ring combinations are tested: ee , $e\pi$, πe , $\pi\pi$. For each of these two ring fits the likelihood is checked to see if it improves with the addition of the new ring. This is done with a quantity called the ring counting likelihood defined as

$$\mathcal{L}_{\text{ring}} = \log(L_{(n+1)\text{R}}/L_{n\text{R}}), \quad (4.26)$$

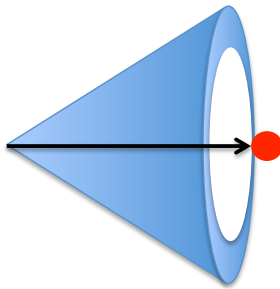
where n corresponds to the number of rings. When comparing the one ring and two ring fits, $n = 1$ and $n + 1 = 2$.

There are several issues to keep in mind when comparing the likelihoods of an event after adding a new ring. First, when additional degrees of freedom are added to the fit, such as with a new ring, the likelihood will

Full Track



Upstream Pion Track



Anti-Track

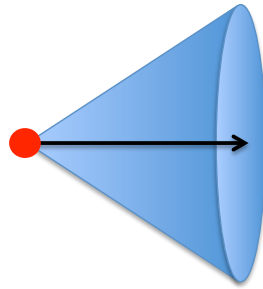


Figure 4.8: Cartoon of the three configurations of the charge likelihood for the upstream pion fit. The blue cones represent the Cherenkov light emitted by each charge likelihood configuration. The red dot indicates the pion scatter point.

typically improve because the result cannot do any worse than the original fit. That is, if the second ring is turned off it is possible to recover the original prediction. This means that when adding a new ring it is necessary to define a threshold over which a change in the likelihood due to a new ring is determined to be improving the event prediction.

The two ring likelihood for the ee and $e\pi$ configurations are compared to the one ring electron fit likelihood. The two ring likelihood for the πe and $\pi\pi$ configurations are compared to the one ring pion fit likelihood. A second ring is considered to improve the event prediction if the ring counting likelihood is greater than 87.5 for a new electron-like ring and 140 for a new pion-like ring. These values were determined empirically by looking at the ring counting distributions from SK atmospheric Monte Carlo (MC), which consists of simulated neutrino events produced with the flux of atmospheric neutrino events at SK .

Fits with three or more rings are constructed by adding an electron-like or pion-like ring to each of the two ring fit configurations. The fit result with an additional ring $n + 1$ is compared to the best fit of the previous fit stage with n rings using the ring counting likelihood. A new ring is determined to improve the event prediction if the ring counting likelihood is greater than 70 for these higher ring multiplicities, independent of ring type. This is done until either the addition of another ring does not improve the ring counting likelihood, or the fit reaches six rings. The multi-ring fit is currently only configured to work for up to six rings. The best fit is the fit hypothesis with the best likelihood among the final fits.

Once this preliminary multi-ring fitting is done the results are refined with a series of ring merging and refitting.

The ring merging is done by looking at the angle between the highest energy ring in the initial multi-ring fit, and each of the lower energy rings. If this angle is less than 20° the rings are added together.

The result of the ring merging is refit ring by ring. First the highest energy ring is refit assuming either an electron or pion hypothesis with all of the other rings fixed to their values from the result of the ring merging. The fit result of the electron ring hypothesis is compared to the pion ring

hypothesis to determine if, based on the likelihood, the highest energy ring is electron-like or pion-like. If the highest energy ring is determined to be electron-like then the fit with the electron hypothesis is used as the best fit. If the highest energy ring is determined to be pion-like then the event is refit with a muon hypothesis for the most energetic ring. The muon hypothesis is used because it is more likely that the highest energy ring in an event will be muon-like, from a charged current interaction, than pion-like from a neutral current interaction. Each of the lower energy rings are similarly refit using just an electron or a pion hypothesis and their particle type is reevaluated. The result of this refitting is the final output of the multi-ring fitter.

4.7 Scattered Charged Pion Fit

In addition to the generic multi-ring fit described above, fitQun also makes it possible to combine rings to search for particular event topologies, such as pion hadronic interactions. The simplest hadronic interaction topology is a charged pion that scatters exactly once in the SK detector, and produces light before and after the hadronic scatter, as illustrated in Fig 4.7. A scattered charged pion fitter was written to look for this charged pion topology. The method is based on one used at MiniBooNE, but the implementation is unique to SK [5].

This scattered charged pion fitter was studied to understand the reconstruction performance for charged pions individually before looking at the more complicated topology of $CC1\pi^+$. This fitter may also be used for physics analyses such as a $NC1\pi^+$ cross section measurement at SK.

4.7.1 Method

Each ring of a fitQun track is characterized by its particle identification as well as its vertex position and time (x, y, z, t) , direction of motion (θ, ϕ) , momentum, and energy lost along the track as the particle propagates in the water.

The scattered π^+ hypothesis is constructed by placing two single ring

π^+ tracks together. The downstream vertex position and time is calculated using kinematics of the upstream track as:

$$\begin{aligned}
x_{DS} &= x_{US} + l_{US} \sin(\theta_{US}) \cos(\phi_{US}) \\
y_{DS} &= y_{US} + l_{US} \sin(\theta_{US}) \sin(\phi_{US}) \\
z_{DS} &= z_{US} + l_{US} \cos(\theta_{US}) \\
t_{DS} &= t_{US} + t(l_{US}),
\end{aligned} \tag{4.27}$$

where l_{US} is the distance that the upstream track traveled, and $t(l_{US})$ is the time that it took the upstream track to travel its length.

The pion is also allowed to elastically or inelastically scatter such that the pion can lose energy in the scatter by restricting the downstream momentum to less than or equal to that of the upstream track. To make this constraint easier to work with, given the fact that the upstream momentum varies in the fit, the downstream momentum is fit as a fraction of the upstream momentum.

Pion Range Table

To approximate the energy lost as a pion travels in water, tables of the continuous slowing down approximation (CSDA) range were produced for fitQun. The CSDA is defined as:

$$\text{CSDA} = \int_{E_0}^0 \frac{dE}{-\frac{dE}{dx}} \tag{4.28}$$

[79].

The energy lost as a particle passes through matter $\frac{dE}{dx}$ can be estimated using the Bethe-Bloch equation:

$$-\frac{dE}{dx} = kz^2 \left(\frac{Z}{A}\right) \frac{1}{\beta^2} \left[\frac{1}{2} \ln \left(\frac{2m_e c^2 \beta^2 \gamma^2 W_{\max}}{I^2} \right) - \beta^2 - \frac{\delta(\beta\gamma)}{2} \right] \tag{4.29}$$

[10] [79]. The constant k is defined as

$$k = 4\pi N_A r_e m_e c^2 \quad (4.30)$$

where $N_A = 6.022141 \times 10^{20} \text{ mol}^{-1}$ is Avogadro's number, $r_e = \frac{e^2}{4\pi\epsilon_0 m_e c^2} = 2.817940285 \text{ fm}$ is the classical electron radius, and $m_e c^2 = 0.510998902 \text{ MeV}$ is the electron rest energy.

z^2 is the charge of the incident particle. The relativistic kinematic quantities are $\beta = v/c$ and $\gamma = 1/\sqrt{1 - \beta^2}$, as calculated for a particle with a given kinetic energy.

W_{\max} is the maximum kinematically allowed electron recoil kinetic energy in matter for an incident particle of mass M , given by:

$$W_{\max} = \frac{2m_e c^2 \beta^2 \gamma^2}{1 + \frac{2\gamma m_e}{M} + \frac{m_e^2}{M^2}} \quad (4.31)$$

[79].

Z/A is the ratio of the atomic number to the atomic mass and I is the mean excitation energy of the material. For water these are 0.55509 and 79.7 eV respectively [10].

The final term of the Bethe-Bloch equation, $\delta(\beta\gamma)$, is the density effect term which is a function of the energy of the incident particle. The pions it is possible to reconstruct at SK fall into the region where the density effect matters, but not high enough in energy to be well described by an asymptotic approximation based on the overall plasma energy of the material. This region is defined by: $x_0 < \log(p/M) < x_1$. For water $x_0 = 0.2400$ and $x_1 = 2.8004$ which corresponds to a range in pion momentum from 242 MeV/c to 87.8 GeV/c. Below this range in pion momentum the density effect is zero in a nonconductor like water. In the intermediate region the density effect function is defined as a function of the Sternheimer coefficients a , k , and \bar{c} as:

$$\delta(\beta\gamma) = 2\ln(10) \log_{10}(\beta\gamma) - \bar{c} + a(x_1 - \log_{10}(\beta\gamma))^k \quad (4.32)$$

For water, these constants are: $a=0.0912$, $k=3.4773$, $\bar{c}=3.5017$ [10].

The PDG calculates tables of the CSDA range as a function of kinetic energy for muons [10] [79]. As other particles, such as charged pions, are not included, the Bethe-Bloch equation was numerically integrated using the inputs above to calculate the CSDA range as a function of momentum for charged pions. This calculation neglects the pion hadronic interactions since the Bethe-Bloch equation only considers ionization loss. As the hadronic interactions are explicitly reconstructed these assumptions are compatible. The results of these calculations are shown in Fig. 4.9 for the momentum range of most pions expected at T2K neutrino energies.

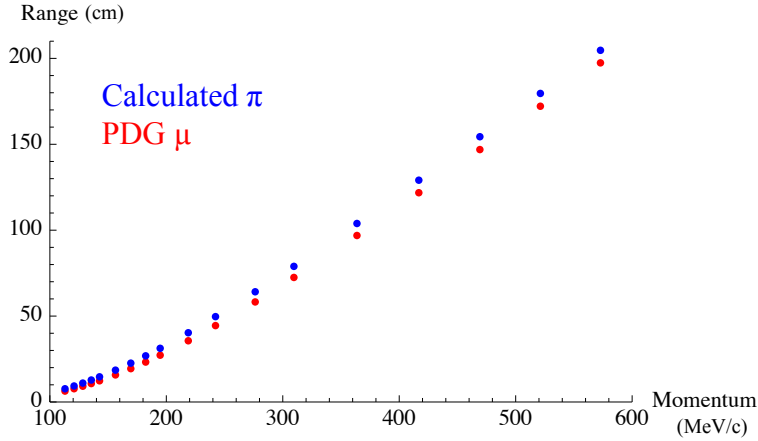


Figure 4.9: Comparison of muon and pion ranges in water at low energy.

A table of pion range as a function of pion momentum was produced up to 4 GeV/c in pion momentum to use in the scattered charged pion reconstruction. The range at a given momentum is calculated by linearly interpolating between the calculated points.

With this table, the distance that the upstream pion travels l_{US} is calculated as the difference in the range of a pion with given momentum p_{US} at the beginning of the upstream track, and momentum p_f at the end of the

upstream track:

$$l_{US} = \text{Range}(p_{US}) - \text{Range}(p_f). \quad (4.33)$$

The range is linearly interpolated between the calculated points in Fig. 4.9.

p_f is calculated in terms of the initial upstream pion momentum, p_{US} , and the upstream energy loss along the pion track as:

$$p_f = \sqrt{(E_{US}/c - E_{loss}/c)^2 - m_\pi^2 c^2}, \quad (4.34)$$

where E_{US} is the energy of the pion at the beginning of the upstream track, E_{loss} is the energy the pion loses along the upstream track, and m_π is the mass of the pion.

The time at which the upstream track ends, $t(l_{US})$ is calculated as:

$$t(l_{US}) = \frac{\rho_{US}}{c}(p_{US}c - p_{DS}c). \quad (4.35)$$

ρ_{US} is an estimate of the range as a function of energy for the upstream track in terms of the distance the pion travels l_{US} and the energy loss of the pion along the upstream track E_{loss} :

$$\rho_{US} = \frac{l_{US}}{E_{loss}}. \quad (4.36)$$

In the one ring fits, and the generic multi-ring fit an approximation of the range as a function of energy is given by $\rho = \frac{1}{dE/dx}$, where dE/dx is assumed to be constant.

Seeding Configurations

The starting point of all seeding configurations for the scattered pion fit is the output of the generic multi-ring fit with two pion rings. The scattered pion algorithm is applied after the generic multi-ring fit. This fit hypothesis assumes that there are two pion rings with independent kinematics produced at a single vertex, as described in Sec. 4.6. The scattered pion fit is done in two configurations, separately assuming that each of the rings from the

generic multi-ring fit with two pion rings is the upstream ring. The downstream ring is seeded by a grid search at the end point of the upstream pion track. The scattered pion fit outputs the kinematics outlined above, as well as the fit negative log likelihood for these two configurations (\mathcal{L}_1 , \mathcal{L}_2). The best fit is selected by comparing the likelihood ratio between these two configurations. If $\mathcal{L}_1 - \mathcal{L}_2 > 0$, then \mathcal{L}_1 is the best fit, and if $\mathcal{L}_2 - \mathcal{L}_1 > 0$, then \mathcal{L}_2 is the best fit.

Studies were also done assuming that the two ring pion fit had identified the upstream and downstream tracks and using each of those to seed the fit instead of the grid search. The fit performance was better when the generic two ring fit was combined with a grid search even though this discards the information from one of the rings in the generic two ring fit.

For comparison the fitter is seeded with the true Monte Carlo information which gives a representation of the theoretical limit of how well the fit can perform. In this case if the fit gets stuck in a local minimum or fails to converge this will be a result of the fit function itself as opposed to improvements that may be made to the seeding algorithm. Similarly the fit results, including the kinematic resolution will be representative of the best that the algorithm can return.

4.7.2 Fit Performance

Validation of the scattered pion fitter was done by testing a variety of different seeding configurations, and fixing and floating the upstream and downstream portions of the fit individually to isolate the fit performance.

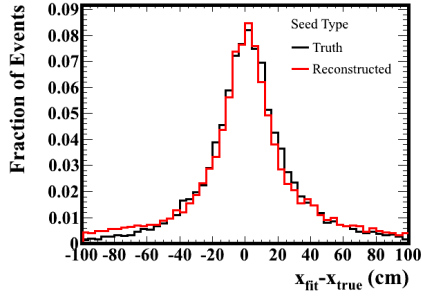
The fitter performance was studied in different seeding configurations on Monte Carlo charged pions. Single charged pions with a flat momentum distribution from 0-1 GeV/c were simulated in random positions and directions in the SK tank. Only basic selection cuts requiring the events to have a vertex position more than two meters from the walls of the inner detector and fewer than 16 hits in the outer detector, were applied. Events were categorized depending on the type of true hadronic interactions the pions underwent. The resolution of the vertex position and scatter point for pions

that undergo any hadronic interactions is shown in Fig. 4.10. The kinematic resolution of the upstream pion tracks for any pion hadronic interactions is shown in Fig. 4.11. The kinematic resolution for the downstream track for pions that undergo any hadronic interaction are shown in 4.12.

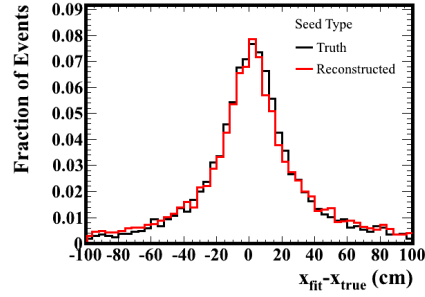
The ideal topology for this fitter is that of a charged pion scattering exactly once in the SK detector and continuing to emit light before and after the scatter, and the fitter performance was also explicitly studied on these events. The vertex position and scatter point for pions that scatter exactly once is shown in Fig. 4.13. The upstream kinematic resolution for pions that scatter exactly once is shown in Fig. 4.14 and the downstream kinematic resolution is in Fig. 4.15. In all of these plots the fitter performance when seeded with the true Monte Carlo kinematics is compared to the reconstructed seeding configuration described in Sec. 4.7.1. In general, the fitter is able to well reconstruct the kinematics, in particular for the upstream pion. Fit performance on pion events that scatter exactly once is almost as good when seeded with reconstructed quantities as when seeded with true quantities.

This fitter was also studied on the T2K-SK ν_μ Monte-Carlo (T2K-SK MC), and the performance is shown to be similar on true NC1 π^+ events. These events are, as described in Section 2.5, simulated to come from the T2K beam flux and contain other outgoing particles from neutrino interactions such as nucleons which could affect the reconstructed topology. They are also more realistic interactions in terms of event topologies that we could expect to reconstruct from neutrino interactions. The vertex and scatter point for all NC1 π^+ events is shown in Fig. 4.16, and the kinematic resolution for all NC1 π^+ events is in Fig. 4.17. The vertex and scatter point for the ideal topology of NC1 π^+ events in which the pion scatters exactly once are shown in Fig. 4.18 and the kinematic resolution for these events is shown in Fig. 4.19. The resolution is similar in both all pion topologies and the single scatter topology to the results on the simulated charged pions with a flat momentum distribution, except that the statistics for NC1 π^+ events are more limited.

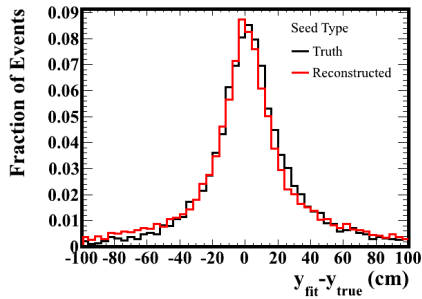
In summary the scattered π^+ fit is able to well reconstruct the up-



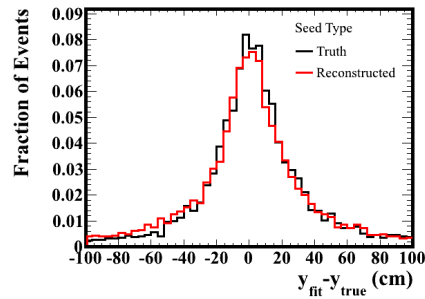
(a) Vertex resolution in x direction.



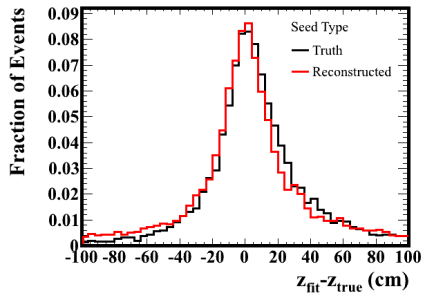
(b) Scatter point resolution in x direction.



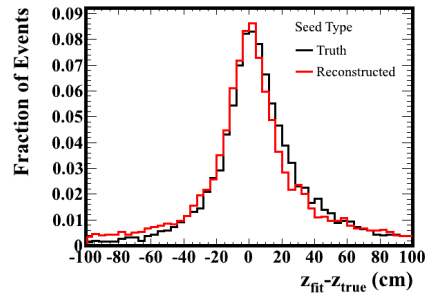
(c) Vertex resolution in y direction.



(d) Scatter point resolution in y direction.

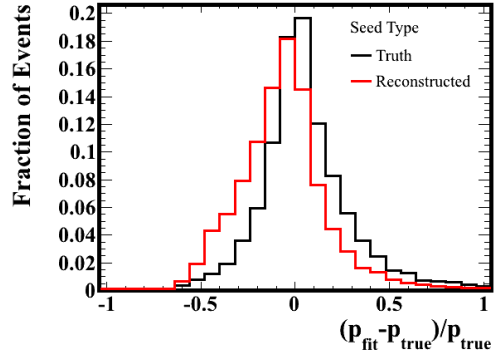


(e) Vertex resolution in z direction.

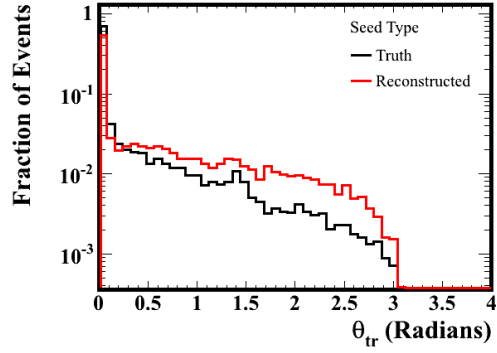


(f) Scatter point resolution in z direction.

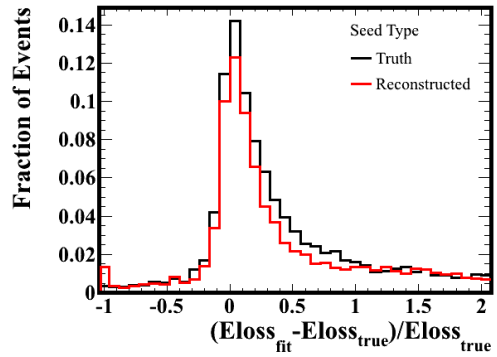
Figure 4.10: Vertex resolution for the scattered pion fit. The left column shows the production point and the right column shows the scatter point. All charged pions are shown in this plot.



(a) Momentum Resolution.

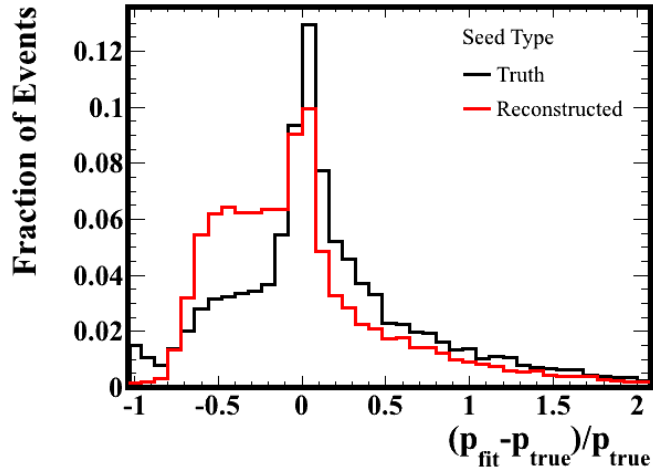


(b) Angle between true and reconstructed directions.

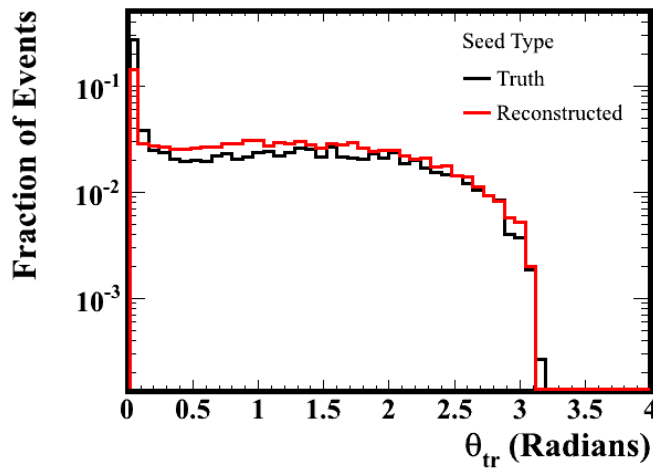


(c) Resolution of energy loss along the track.

Figure 4.11: Kinematic resolution of scattered pion fitter for the upstream pion track. All charged pions are shown in this plot.

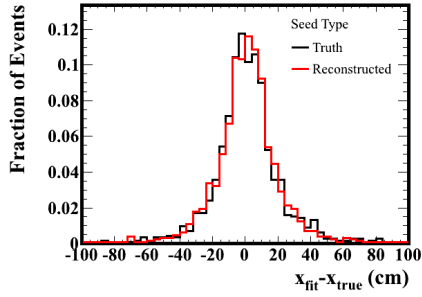


(a) Momentum Resolution.

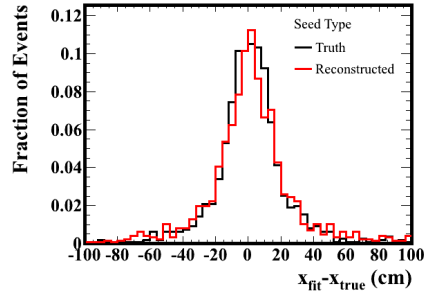


(b) Angle between true and reconstructed directions.

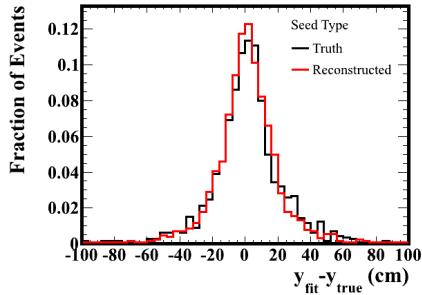
Figure 4.12: Kinematic resolution of scattered pion fitter for the downstream pion track. All charged pions are shown in this plot.



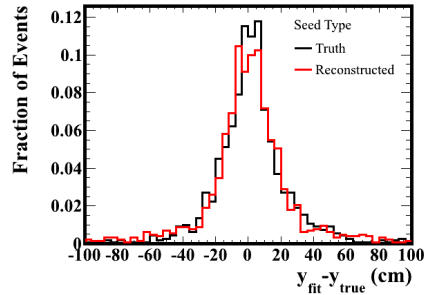
(a) Resolution in x direction.



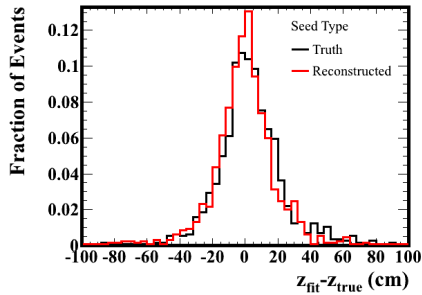
(b) Resolution in x direction.



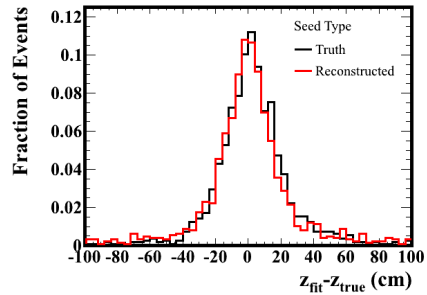
(c) Resolution in y direction.



(d) Resolution in y direction.

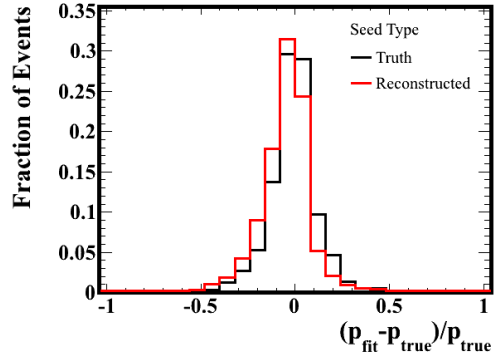


(e) Resolution in z direction.

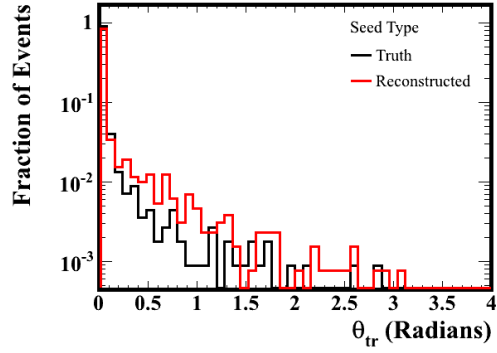


(f) Resolution in z direction.

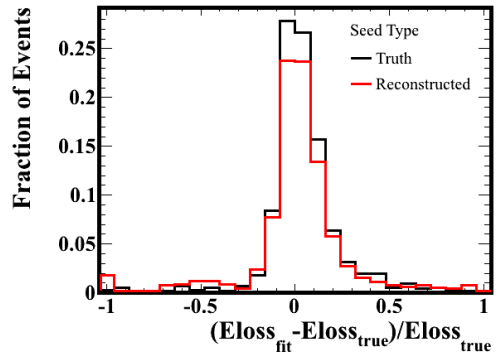
Figure 4.13: Vertex resolution for the scattered pion fit. The left column shows the production point and the right column shows the scatter point. Charged pions that scatter exactly once are shown in this plot.



(a) Momentum Resolution.

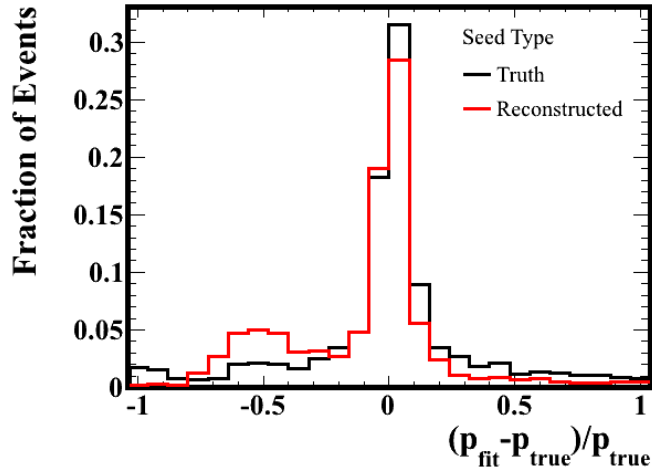


(b) Angle between true and reconstructed directions.

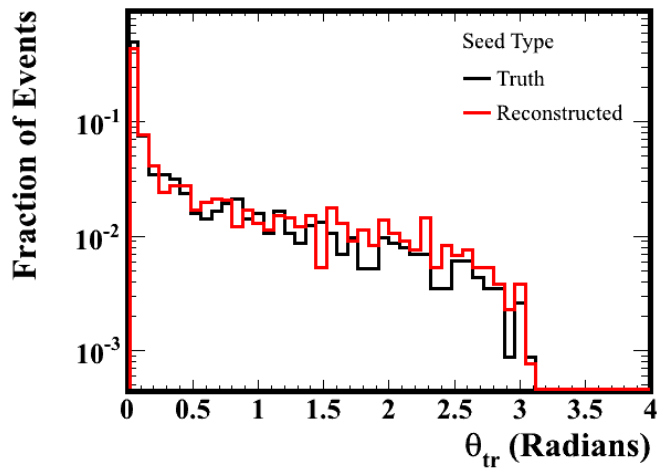


(c) Resolution of energy loss along the track.

Figure 4.14: Kinematic resolution of the scattered pion fitter for the upstream pion track. Charged pions that scatter exactly once are shown in this plot. 85

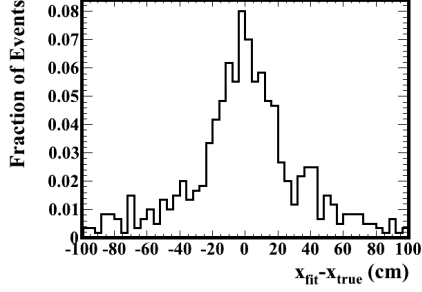


(a) Momentum Resolution.

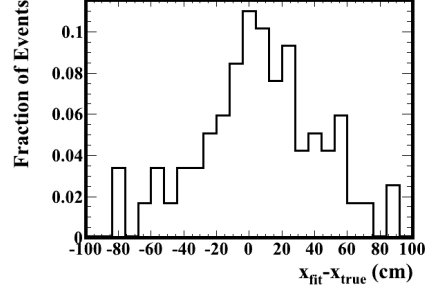


(b) Angle between true and reconstructed directions.

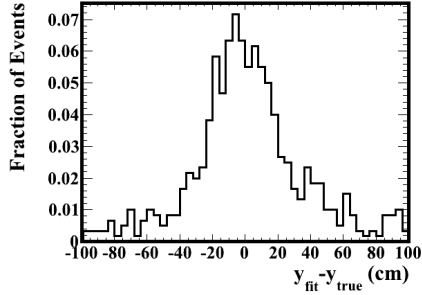
Figure 4.15: Kinematic resolution of the scattered pion fitter for the downstream pion track. Charged pions that scatter exactly once are shown in this plot.



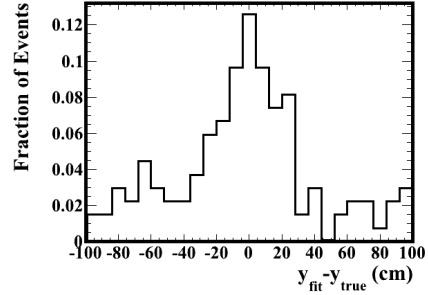
(a) Neutrino interaction vertex resolution in x direction.



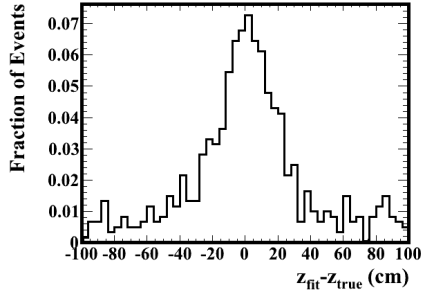
(b) Scatter point resolution in x direction.



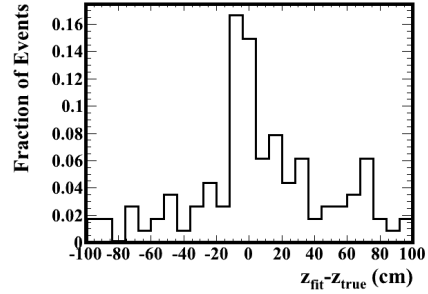
(c) Neutrino interaction vertex resolution in y direction.



(d) Scatter point resolution in y direction.

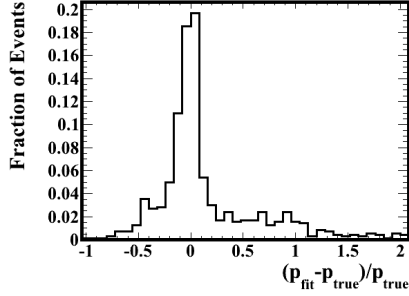


(e) Neutrino interaction vertex resolution in z direction.

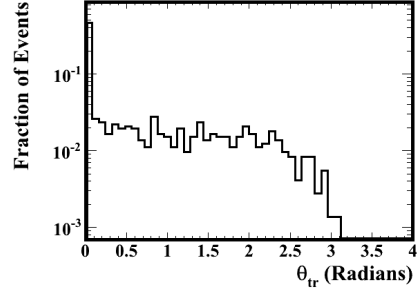


(f) Scatter point resolution in z direction.

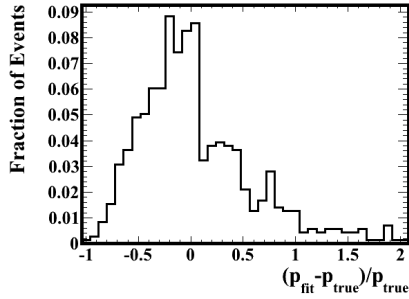
Figure 4.16: Vertex resolution for the scattered pion fit on $\text{NC}1\pi^+$ events in the T2K-SK MC for all outgoing pions. The left column shows the neutrino interaction vertex and the right column shows the scatter point.



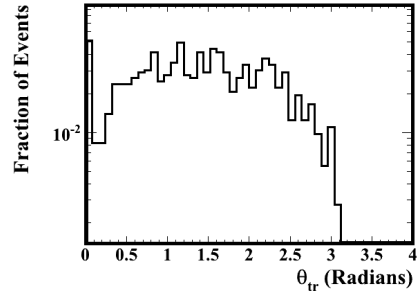
(a) Momentum resolution for the upstream track.



(b) Angle between true and reconstructed directions for the upstream track.



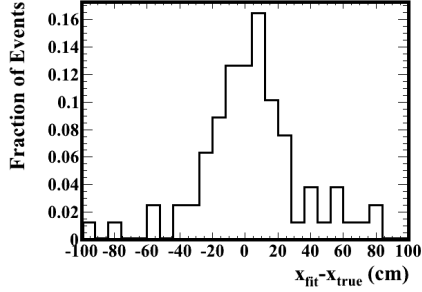
(c) Momentum resolution for the downstream track.



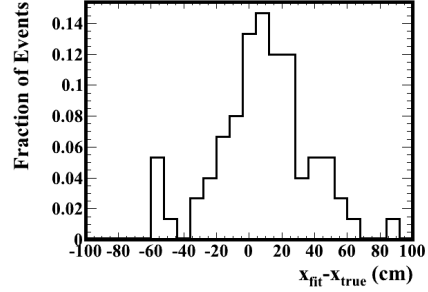
(d) Angle between true and reconstructed directions for the downstream track.

Figure 4.17: Kinematic resolution of the scattered pion fitter on $\text{NC}1\pi^+$ events in the T2K-SK MC for all outgoing pions.

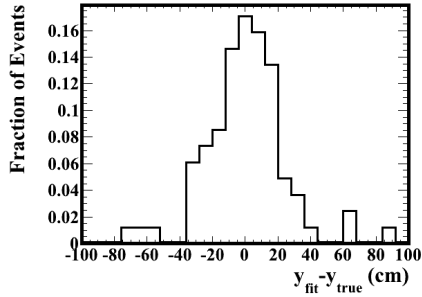
stream and downstream track parameters for simulated charged pions that are placed at random position and directions in the SK detector as well as for single charged pions that come from neutrino interactions with the T2K beam flux. The kinematics are best for the target topology of a charged pion scattering exactly once, but can also be reconstructed for charged pions that undergo any secondary interactions in the SK water.



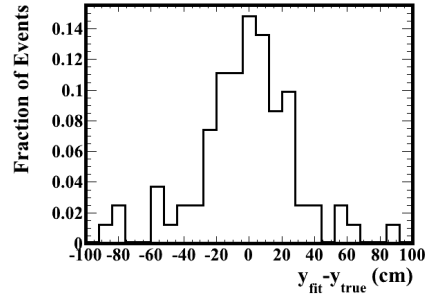
(a) Neutrino interaction vertex resolution in x direction.



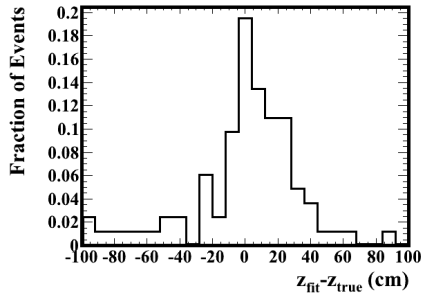
(b) Scatter point resolution in x direction.



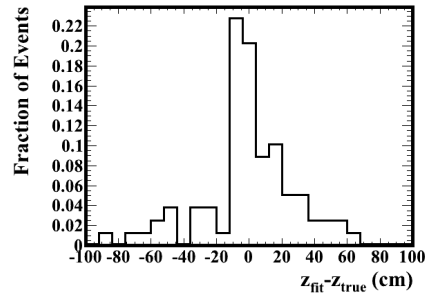
(c) Neutrino interaction vertex resolution in y direction.



(d) Scatter point resolution in y direction.

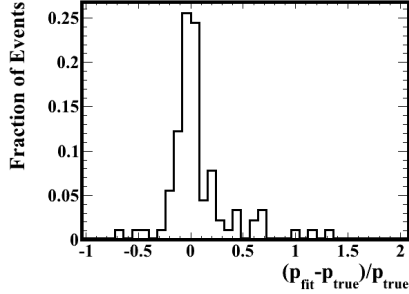


(e) Neutrino interaction vertex resolution in z direction.

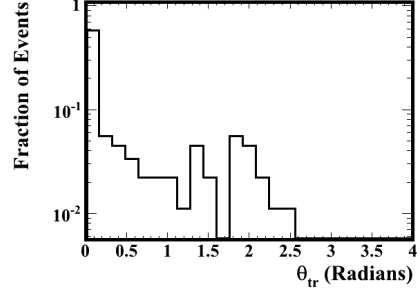


(f) Scatter point resolution in z direction.

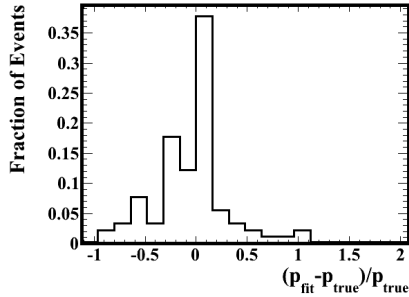
Figure 4.18: Vertex resolution for the scattered pion fit on $\text{NC}1\pi^+$ events in the T2K-SK MC with outgoing pions that scatter exactly once. The left column shows the neutrino interaction vertex and the right column shows the scatter point vertex.



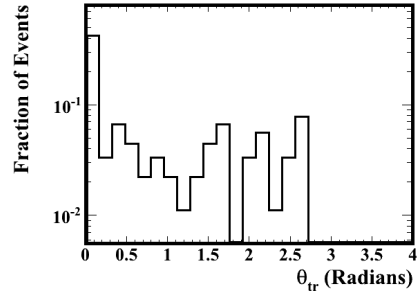
(a) Momentum resolution for the up-stream track.



(b) Angle between true and reconstructed directions for the upstream track.



(c) Momentum resolution for the down-stream track.



(d) Angle between true and reconstructed directions for the downstream track.

Figure 4.19: Kinematic resolution of the scattered pion fitter on $\text{NC1}\pi^+$ events in the T2K-SK MC with outgoing pions that scatter exactly once.

4.8 ν_μ $\text{CC1}\pi^+$ Reconstruction

It is possible to combine the scattered pion fit with a muon ring to create a dedicated ν_μ $\text{CC1}\pi^+$ hypothesis, where the muon and the upstream pion are assumed to originate from the same vertex, and the downstream pion track begins at the endpoint of the upstream pion track. The topology that is used is illustrated in Fig. 4.20. The charged pion portion of the fit is constructed in exactly the same way as the scattered charged pion fit described earlier, but a single muon track is added.

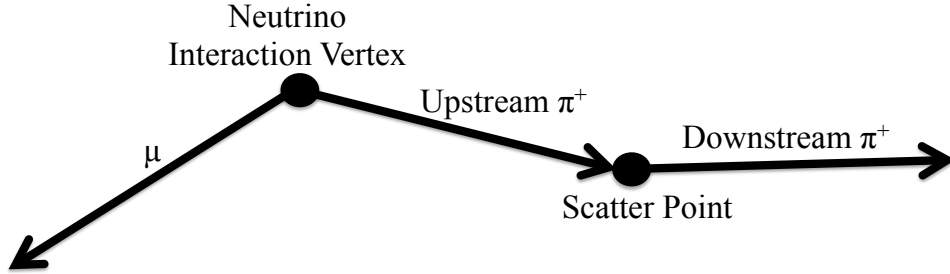


Figure 4.20: Cartoon of the $CC1\pi^+$ hypothesis.

Like the scattered pion fit, this fit is seeded with the two ring pion fit result from the generic multi-ring fitter and is applied to an event after the multi-ring fit has already been run. In this case, however, the fit is seeded assuming that one of the rings is the muon and the other is the upstream pion. A seed for the downstream pion is found using a grid search on the end of whichever ring is called the “upstream pion” for seeding purposes. The fit is done twice, assuming that the two rings from the generic multi-ring fit can correspond to either the muon or the upstream pion. In this case, the fit will output 19 parameters: the muon kinematics (momentum and direction), upstream pion kinematics (momentum, direction and energy lost along the track), downstream pion kinematics (momentum, direction, and energy lost along the track), as well as the neutrino interaction vertex, the scattered pion vertex. The likelihoods for each fit configuration are also returned.

The fit resolution and seeding configuration were optimized on a $CC1\pi^+$ particle gun sample in which a Monte Carlo muon and pion were generated to come from a single vertex randomly placed in the SK tank, and to be emitted at random angles relative to each other. This sample is called a “particle gun” sample because the particles are placed in the tank at a position and with some designated kinematics without assuming that they come from a neutrino interaction, as if it were possible to place a muon and pion source at randomly distributed points in the detector. The muons and pions were uniformly distributed in momentum between 0.1 and 1 GeV/ c , and completely

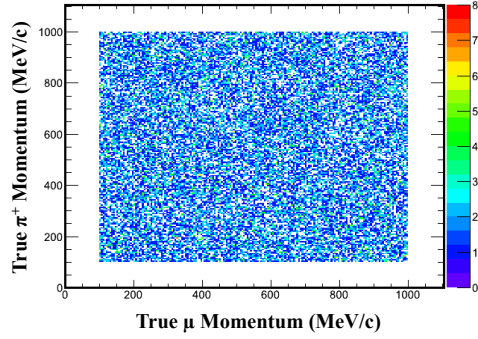
uncorrelated. The momentum distribution of the events generated is shown in Fig 4.21a. These are quite different from the muon and pion momentum distributions from events in the T2K-SK MC, in which the muon tends to be higher momentum than the pion for both unoscillated and oscillated events as illustrated in Fig. 4.21b and 4.21c. As illustrated in these plots the effect is larger for oscillated events.

Each time that the $CC1\pi^+$ fit is run, there are two output likelihoods, one for each seeding combination of muon and pion rings. In most cases one of the two seeding configurations is able to reconstruct the events, but unlike in the scattered pion fit, simply picking the result with the best likelihood did not typically return the result with the best kinematic resolution.

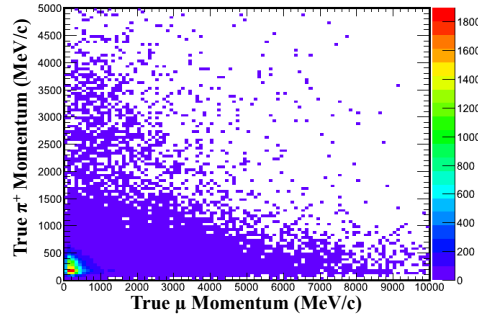
The two output fits from the $CC1\pi^+$ fit can be classified as one where the reconstructed momentum of the muon track is higher than that of the pion track, $\mathcal{L}(p_\mu > p_\pi)$, and one where the reconstructed momentum of the muon track is lower than that of the pion track, $\mathcal{L}(p_\pi > p_\mu)$. These two cases correspond almost exactly to which particle is seeded with the higher energy ring from the generic two ring fit.

The result with the best kinematic resolution is usually the case where the muon is seeded with the higher energy of the two rings from the generic two ring fit. This is because even if the pion energy is initially higher than that of the muon, the muon will appear to be higher energy than the pion due to the fact that the charged pion may lose energy in hadronic interactions. The fraction of times that the muon is better matched to the higher energy ring of the generic multi-ring fit with two pion rings is displayed in Table 4.1. Despite this, the likelihood prefers to assign the higher energy ring to the fit configuration with more degrees of freedom. As described in Section 4.5.1, the pion track has an additional degree of freedom due to the energy loss parameter that defines the distance the pion travels before a hadronic interaction. This additional fit parameter makes it easier to describe other complexities of high energy muon rings such as multiple scattering or decay in flight, and means that typically the muons are better described by the charged pion fit.

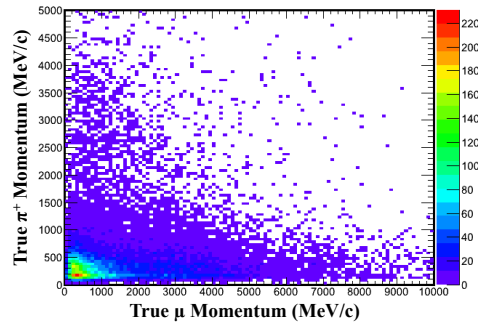
The likelihood ratio of these two outputs from the $CC1\pi^+$ fit, $\mathcal{L}(p_\mu >$



(a) $CC1\pi^+$ particle gun.



(b) Unoscillated $CC1\pi^+$ -like T2K-SK MC events.



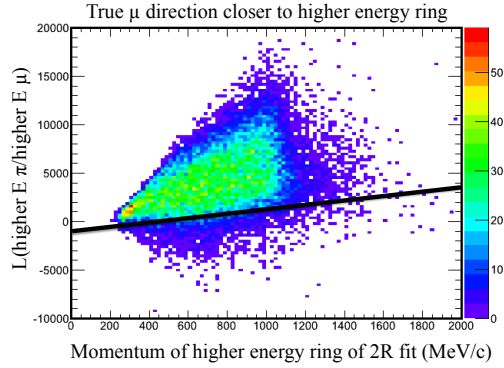
(c) Oscillated $CC1\pi^+$ -like T2K-SK MC events.

Figure 4.21: Pion and muon momentum distributions for samples used to study the $CC1\pi^+$ fitter.

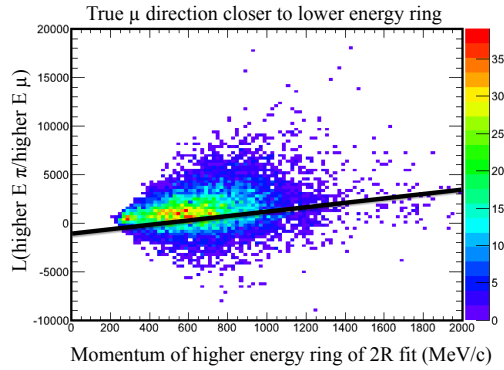
Table 4.1: Fraction that the μ ring is better matched to the higher or lower energy ring of the two ring pion fit.

μ better matched to:	Higher energy ring of 2R π fit (%)	Lower Energy Ring of 2R π fit (%)
CC1 π^+ Particle Gun	73.3	26.7
T2K-SK MC, no oscillation	81.8	18.2
T2K-SK MC, with oscillation	88.5	11.5

$p_\pi) - \mathcal{L}(p_\pi > p_\mu)$, was studied to look for a better place to put the muon-pion particle identification cut to improve the efficiency at which the correct configuration is selected. To do this, the CC1 π^+ particle gun sample was separated into cases where the angle between the true muon direction better matches the higher energy ring and where the true muon direction better matches the lower energy ring. For these two samples the likelihood ratio between the two fit outputs were plotted in terms of a variety of kinematic variables. The likelihood ratio as a function of the momentum of the higher energy ring from the generic multi-ring fit with two pion rings is shown in Fig. 4.22. These plots show significant overlap between these samples, as well as that if the likelihood cut is placed at zero, the fit assuming $p_\pi > p_\mu$ will be selected almost all of the time, despite the fact that this is true only about 25% of the time. Instead of this more basic cut at $\mathcal{L}(p_\mu > p_\pi) - \mathcal{L}(p_\pi > p_\mu) = 0$, a cut in the likelihood space was made to follow the peak of the distribution that matches the muon to the higher energy ring, and to go through the center of the distribution that matches the muon to the lower energy ring. This cut is placed at: $\mathcal{L}(p_\mu > p_\pi) - \mathcal{L}(p_\pi > p_\mu) = 2p_{2R \text{ high}} - 500$, where $p_{2R \text{ high}}$ is the momentum of the higher energy ring of the generic multi-ring fit with two pion rings in MeV/ c . It was optimized on the CC1 π^+ particle gun sample. This cut is shown for the CC1 π^+ particle gun in Fig. 4.22, and for the oscillated and unoscillated T2K-SK MC in Fig. 4.23. The fraction that this line cut selects the correct configuration for the muon ring is shown in Table 4.2. This cut selects the correct fit configuration 88.6% of the time for the oscillated T2K-SK MC. This could potentially be improved in the future by applying machine learning methods.

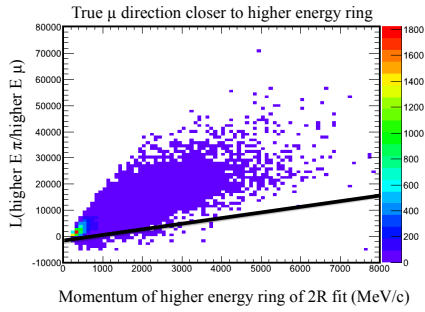


(a) True muon direction closer to higher energy ring of 2R fit.

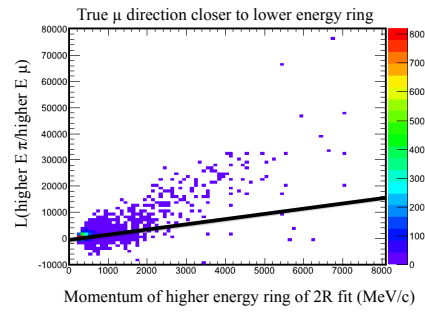


(b) True muon direction closer to lower energy ring of 2R fit.

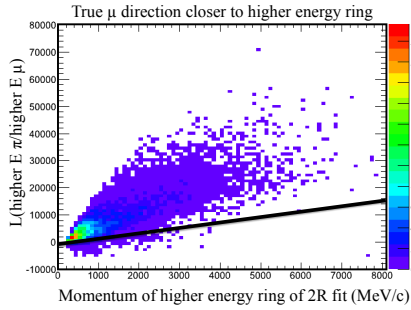
Figure 4.22: $CC1\pi^+$ particle gun broken into samples in which the muon is better matched to the higher energy ring from the generic two ring fit (top) and the lower energy ring from the generic two ring fit (bottom). The muon/pion PID is the black line.



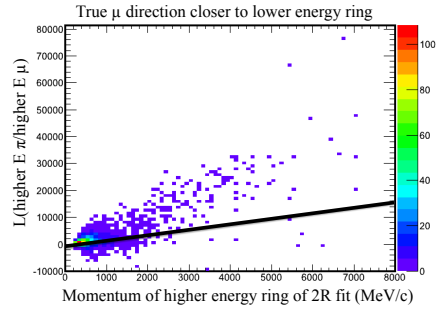
(a) True muon direction closer to higher energy ring of 2R fit for the unoscillated T2K-SK MC.



(b) True muon direction closer to lower energy ring of 2R fit for the unoscillated T2K-SK MC.



(c) True muon direction closer to higher energy ring of 2R fit for the oscillated T2K-SK MC.



(d) True muon direction closer to lower energy ring of 2R fit for the oscillated T2K-SK MC.

Figure 4.23: T2K-SK MC broken into samples in which the muon is better matched to the higher energy ring from the generic two ring fit (left row) and the lower energy ring from the generic two ring fit (right row). The top row shows the unoscillated MC and the bottom row shows the oscillated MC. The muon/ π PID is the black line.

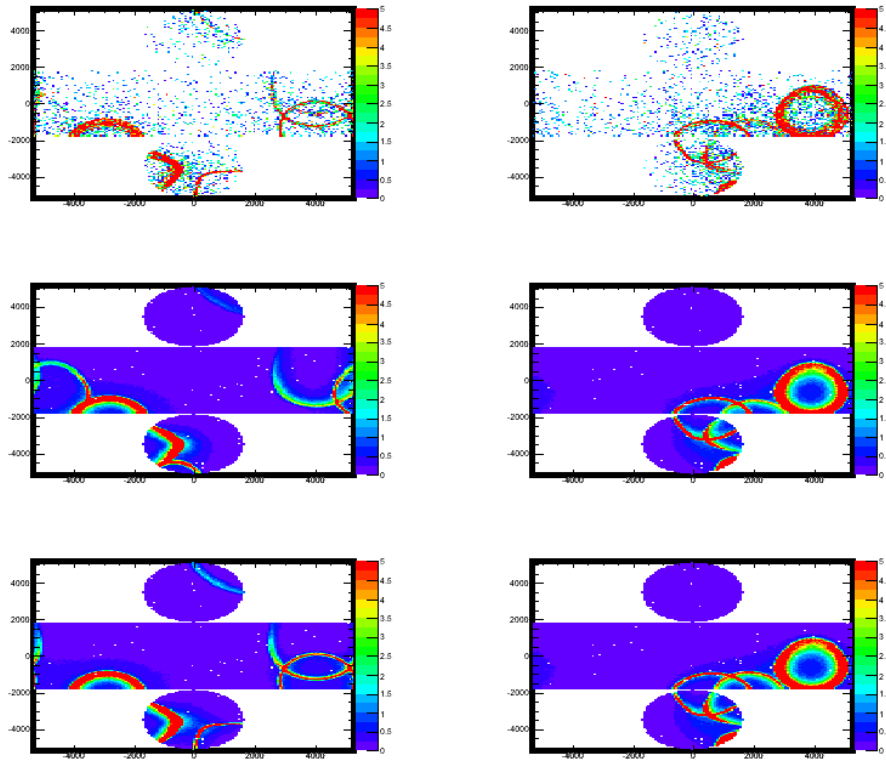
Table 4.2: Fraction that the μ ring is correctly assigned in the best fit configuration when the likelihood cut is used to select the best fit.

	% Correct	% Incorrect
CC1 π^+ Particle Gun	73.3	26.7
T2K-SK MC, no oscillation	81.8	18.2
T2K-SK MC, with oscillation	88.6	11.4

4.8.1 Performance

Two example post-fit charge distributions are shown compared to event displays for a CC1 π^+ particle gun event in Fig. 4.24. In these events the muon ring is visible, along with an upstream and downstream ring from a scattered charged pion. The upstream pion ring is thin because the pion abruptly changes direction and stops emitting light in its initial direction when it scatters. The muon ring is more filled in because it travels in a single direction and emits light until it drops below Cherenkov threshold.

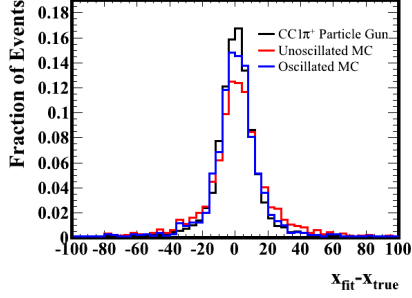
The CC1 π^+ fitter performance is compared using the CC1 π^+ particle gun sample as well as the oscillated and unoscillated T2K-SK MC. The vertex resolution for the neutrino interaction point and the position of the pion scatter is shown in Fig. 4.25. The muon momentum and direction resolution are shown in Fig. 4.26. The upstream pion kinematics are shown in Fig. 4.27 and the downstream pion kinematics are shown in Fig. 4.28. These plots demonstrate that the CC1 π^+ fitter is able to successfully reconstruct the muon and pion kinematics needed to calculate the neutrino energy of an event.



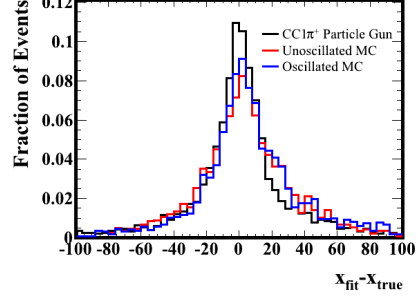
(a) Left-most ring is the muon. Two thin rings to the right are the upstream and downstream pion rings.

(b) Right-most ring is the muon. Two thin rings to the left are the upstream and downstream pion rings.

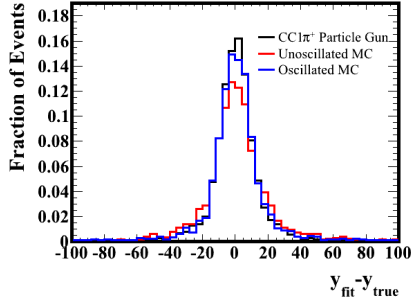
Figure 4.24: Example event display outputs from the $CC1\pi^+$ fit. The top row is the true PMT hit distribution, the middle row is the seed charge distribution, and the bottom row is the charge distribution after the $CC1\pi^+$ fit is run. The post-fit charge distribution is visibly the same as the true distribution of hit PMTs in both of these events.



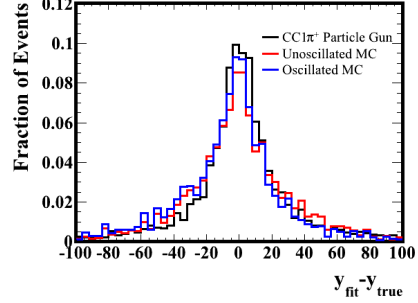
(a) Neutrino interaction vertex resolution in x direction.



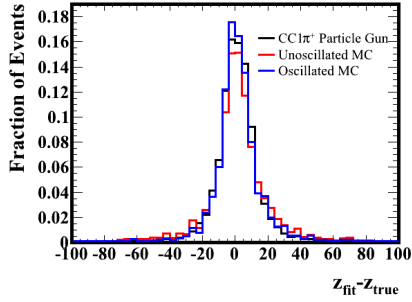
(b) Scatter point resolution in x direction.



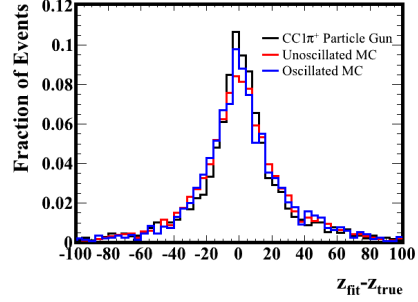
(c) Neutrino interaction vertex resolution in y direction.



(d) Scatter point resolution in y direction.

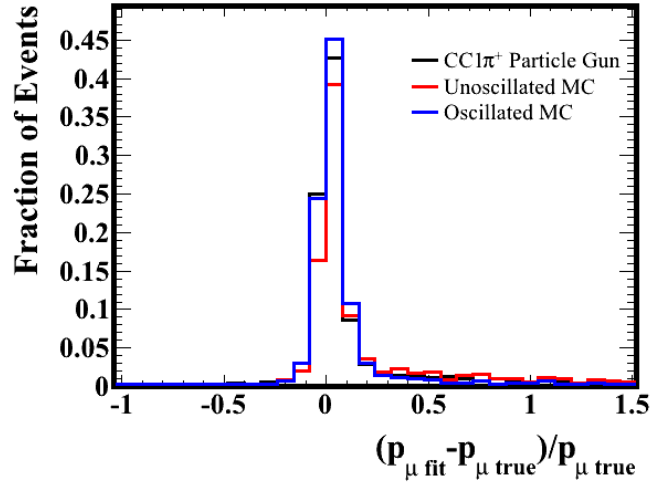


(e) Neutrino interaction vertex resolution in z direction.

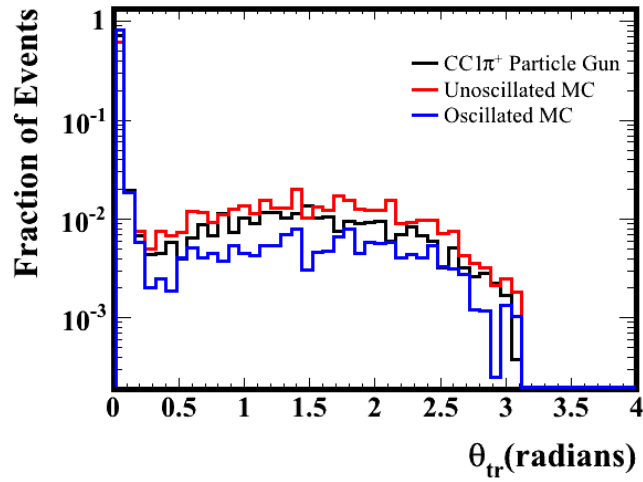


(f) Scatter point resolution in z direction.

Figure 4.25: Vertex resolution for the $CC1\pi^+$ fit on the $CC1\pi^+$ particle gun, oscillated and unoscillated T2K-SK MC. The left column shows the neutrino interaction vertex and the right column shows the scatter point vertex.

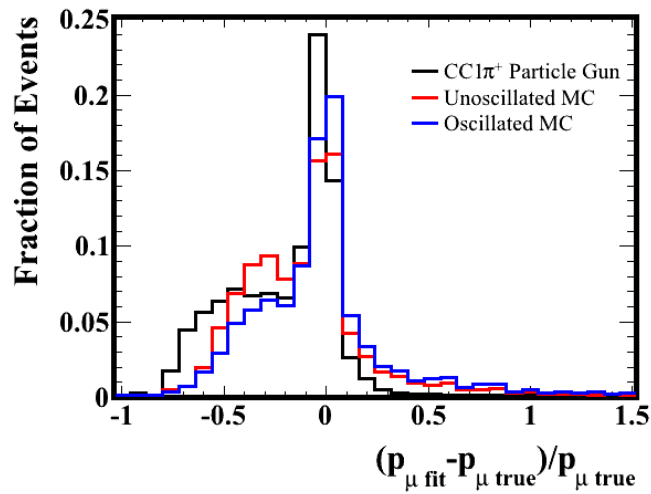


(a) Muon momentum resolution.

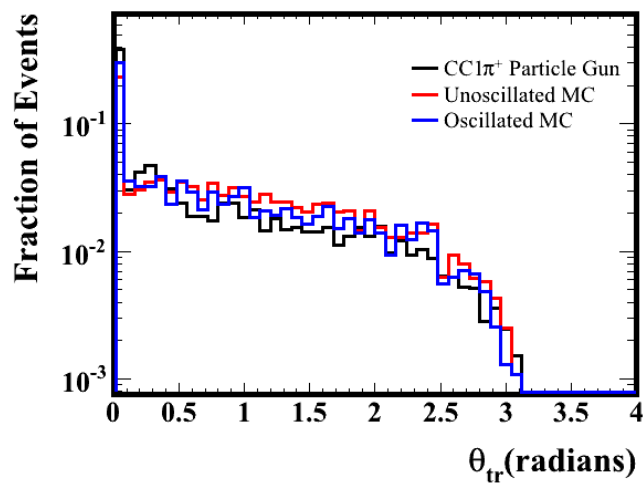


(b) Angle between true and reconstructed muon direction.

Figure 4.26: Fit resolution of the muon kinematics compared for $CC1\pi^+$ particle gun sample, unoscillated $CC1\pi^+$ events from the T2K-SK MC, and oscillated $CC1\pi^+$ events from the T2K-SK MC.

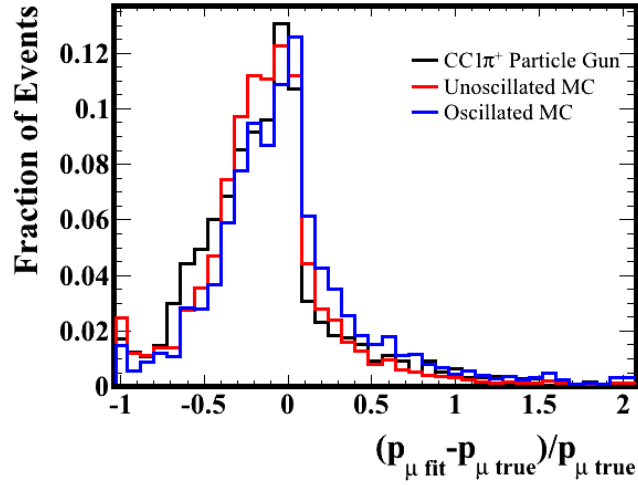


(a) Upstream pion momentum resolution.

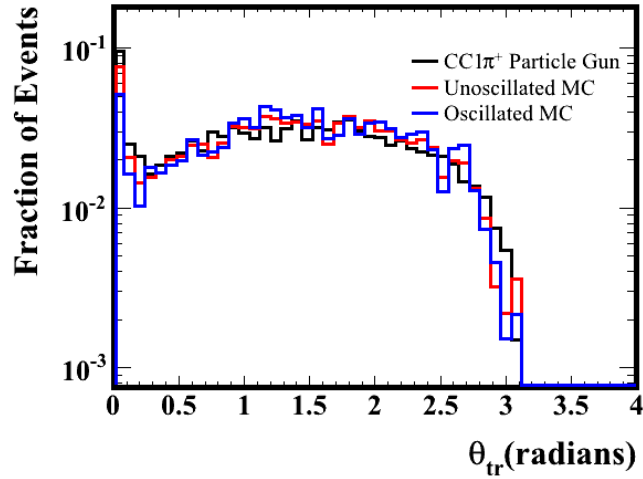


(b) Angle between true and reconstructed upstream pion direction.

Figure 4.27: Fit resolution of the upstream pion kinematics compared for $CC1\pi^+$ particle gun sample, unoscillated $CC1\pi^+$ events from the T2K-SK MC, and oscillated $CC1\pi^+$ events from the T2K-SK MC.



(a) Downstream pion momentum resolution.



(b) Angle between true and reconstructed downstream pion direction.

Figure 4.28: Fit resolution of the downstream pion kinematics compared for $CC1\pi^+$ particle gun sample, unoscillated $CC1\pi^+$ events from the T2K-SK MC, and oscillated $CC1\pi^+$ events from the T2K-SK MC.

Chapter 5

ν_μ CC1 π^+ Event Selection

As described in Section 2.4, CC1 π^+ interactions have the second largest cross section in the energy range of the T2K neutrino beam. Identifying these events can increase the total number of charged current neutrino interactions observed at SK from the T2K beam line, and can provide an additional signal to measure neutrino oscillations. This chapter will present the selection of one ring and multi-ring ν_μ CC1 π^+ events.

As introduced in Chapter 1, CC1 π^+ events are defined as the interaction where a neutrino interacts on a nucleon to produce a lepton, charged pion and nucleon. For ν_μ CC1 π^+ : $\nu_\mu + n/p \rightarrow \mu^- + \pi^+ + n/p$. Due to final state interactions, however, the pion may absorb or charge exchange in the nucleus, which means that not all CC1 π^+ events as defined by neutrino interaction mode will have a π^+ that exits the nucleus. This chapter will focus on visible CC1 π^+ events, which are defined as having exactly one pion and one muon exiting the nucleus after a neutrino interaction. This corresponds to what we will be able to see at SK, independent of what may have occurred in the neutrino-nucleon interaction.

CC1 π^+ events primarily have either one, two, or three rings. One ring events occur when only the muon is above Cherenkov threshold and visible in the detector. Two ring events occur when the muon and pion are both above Cherenkov threshold. Three ring events occur when the muon and pion are both above Cherenkov threshold, and the pion scatters in the detector and

continues to produce light after the interaction.

Decay electrons can also be used to help tag $\text{CC1}\pi^+$ events. Positively charged pions, such as those produced in $\text{CC1}\pi^+$ neutrino interactions, decay 99.988% of the time as:

$$\begin{aligned}\pi^+ &\rightarrow \mu^+ + \nu_\mu \\ &\rightarrow e^+ + \nu_e + \bar{\nu}_\mu\end{aligned}\tag{5.1}$$

with a mean lifetime for the initial pion decay of 2.603×10^{-8} s [10]. The other 1.234×10^{-4} % of the time they decay directly into a positron and electron neutrino as $\pi^+ \rightarrow e^+ + \nu_e$. Hadronic interactions in the water such as charge exchange and absorption can also affect whether or not a charged pion produces a decay electron.

Muons produced in CCQE and $\text{CC1}\pi^+$ interactions decay as:

$$\mu^- \rightarrow e^- + \bar{\nu}_e + \nu_\mu\tag{5.2}$$

with a mean lifetime of $2.197\mu\text{s}$ [10].

Negatively charged muons may also capture in the water, in which case they will not produce a decay electron. Capture will also impact the effective lifetime of the muon [10].

This means that a ν_μ $\text{CC1}\pi^+$ event may have zero decay electrons if neither the muon nor the pion produces a decay electron, one decay electron if one of the muon or pion produces a decay electron, or two decay electrons if both the muon and the pion produce a decay electron. The decay electron detection efficiency at SK is about 88%, and this may also cause migrations between these decay electron categories.

The $\text{CC1}\pi^+$ selection presented here is built around the number of decay electrons and the number of rings.

5.1 Neutrino Energy Calculation

For a high purity sample of $\text{CC1}\pi^+$ events it is possible to calculate the neutrino energy. This gives more detailed information about the oscillations

neutrinos undergo.

If both the muon and pion are above Cherenkov threshold and their kinematics are reconstructed as discussed in Chapter 4, the neutrino energy can be calculated using four momentum conservation. Assuming that the target nucleon is at rest and that the unmeasured final state particle is a nucleon, the reconstructed neutrino energy is

$$E_\nu = \frac{m_\mu^2 + m_{\pi^+}^2 - 2m_N(E_\mu + E_{\pi^+}) + 2\mathbf{p}_\mu \cdot \mathbf{p}_{\pi^+}}{2(E_\mu + E_{\pi^+} - |\mathbf{p}_\mu| \cos \theta_{\nu\mu} - |\mathbf{p}_{\pi^+}| \cos \theta_{\nu\pi^+} - m_N)}, \quad (5.3)$$

where m_μ , m_{π^+} , m_N are the masses of the muon, pion and nucleon, E_μ and E_{π^+} are the energy of the muon and pion, p_μ and p_{π^+} are the 4-momentum of the muon and pion, $|\mathbf{p}_\mu|$ and $|\mathbf{p}_{\pi^+}|$ are the magnitude of the 3-momentum of the pion and muon, $\theta_{\nu\mu}$ is the angle between the neutrino and muon directions, and $\theta_{\nu\pi^+}$ is the angle between the neutrino and pion directions. This calculation neglects the Fermi motion of the nucleons within the nucleus.

If the pion is below Cherenkov threshold and its kinematics can not be directly reconstructed, the neutrino energy can still be calculated by assuming that the pion produced comes from the decay of a Δ in the nucleus as this is the primary method of pion production. With this assumption it is possible to calculate neutrino energy again using four-momentum conservation. In this case the neutrino energy only depends on the muon kinematics and the mass of the Δ which is assumed to be the peak of the resonance at 1232.0 MeV/ c^2 :

$$E_\nu = \frac{2m_p E_\mu + m_\Delta - m_p^2 - m_\mu^2}{2(m_p - E_\mu + p_\mu \cos \theta_{\nu\mu})}, \quad (5.4)$$

where E_μ , p_μ and $\cos \theta_{\nu\mu}$ are the muon energy, momentum and direction relative to the neutrino beam, and m_p , m_Δ , m_μ are the masses of the proton, Δ resonance and muon respectively.

These formulas will be used to calculate neutrino energy in the selected CC1 π^+ samples discussed in the rest of this chapter. Either formula may be used for events with multiple rings, but the neutrino energy resolution for

the signal is found to be better using the muon and pion kinematics than the assumption of a Δ resonance. In the following sections Eq. 5.4 is used for the one ring events and Eq. 5.3 is used for the multi-ring events. This will be discussed in more detail in Section 5.6.

5.2 Visible Event Topologies

At each stage of the selection the events remaining are broken up into visible event topologies based on the true particles exiting the nucleus after the neutrino interaction. These particles correspond to what we will be able to actually see in the SK detector, independent of what may have actually occurred in a neutrino interaction. For example, these categories may vary from the true neutrino interaction topologies because of final state interactions of pions or nucleons within the nucleus.

A particle that exits the nucleus after a neutrino interaction is called a primary particle. These primary particles may also re-interact in the water in the SK tank, and these are called secondary interactions, with the particles produced in these interactions called secondary particles. Secondary interactions may also change the visible event topology, and what is reconstructed in the detector. In particular these affect whether we are able to reconstruct an event as the CCQE or $CC1\pi^+$ events used as neutrino oscillation signal in the T2K analysis.

As mentioned earlier we are interested in $CC1\pi^+$ events with pions both above and below Cherenkov threshold. One ring $CC1\pi^+$ events with a pion below Cherenkov threshold can be tagged if both the muon and the pion produce a decay electron. The number of decay electrons can, however, be affected by secondary interactions in the water. Pions that absorb or charge exchange will not produce decay electrons, and if they are below threshold will not be detected. On the other hand, if a pion is above Cherenkov threshold and absorbs in the water the pion ring may still be detected before the absorption even if it does not produce a decay electron. Furthermore we are interested in reducing the background due to events with π^0 as much as possible because the pion kinematics are not well understood and will have

a large systematic uncertainty.

It is also important to note that particles just at the Cherenkov threshold may produce little or no light that is detectable in the SK PMTs, so for a particle to be considered visible it is required to have a momentum that is 30 MeV/ c above the Cherenkov threshold.

Using these considerations the visible event categories defined in the T2K-SK MC are as follows:

- CC0 π : one muon, no pions, any number of nucleons and photons from nuclear de-excitations (called nuclear gammas), no other primary particles. The proton is below Cherenkov threshold.
- CC0 π , proton over threshold (ot): one muon, no pions, any number of nucleons or nuclear gammas, no other primary particles. The proton is at least 30 MeV/ c over Cherenkov threshold.
- CC1 π^+ , π^+ over threshold (ot): one primary muon, one primary π^+ with any number of nucleons and nuclear gammas and no other primary particles. The pion is at least 30MeV/ c over Cherenkov threshold and is allowed to scatter any number of times, or absorb. It can not have a secondary interaction charge exchange, double charge exchange or hadron production.
- CC1 π^+ , π^+ under threshold (ut): one primary muon, one primary π^+ with any number of nucleons and nuclear gammas and no other primary particles. The pion is below Cherenkov threshold and is allowed to scatter any number of times, or absorb. It can not have a secondary interaction charge exchange, double charge exchange or hadron production.
- CC1 π^+ , charge exchange (CX): one primary muon, one primary π^+ that undergoes charge exchange in the water.
- CC1 π^+ , double charge exchange or hadron production (mpi): one primary muon, one primary π^+ that either undergoes double charge exchange or produces multiple pions in the water.

- $CC\pi^0$: one primary muon, at least one primary π^0 .
- $CCm\pi$: one primary muon, multiple π^+ or π^- , or both a π^+ and π^- . No π^0 s.
- $CCother$: one muon, and anything not in the other categories.
- $NC0\pi$: no primary muon, no pions, any number of nucleons and nuclear gammas, no other primary particles.
- $NC1\pi^+$: no primary muon, one primary π^+ with any number of nucleons and nuclear gammas, and no other primary particles.
- $NC\pi^0$: no primary muon, one primary π^0 with any number of nucleons and nuclear gammas, and no other primary particles.
- $NCm\pi$: no primary muon, multiple π^+ or π^- , or both a π^+ and π^- . No π^0 s.
- $NCother$: no primary muon, and not in any of the other categories

These detailed categories may then be more coarsely grouped into the following categories based on the type of neutrino interaction that may have created these visible topologies. These are defined as:

- $CCQE = CC0\pi + (CC0\pi, \text{proton over threshold})$
- $CC1\pi^+ = (CC1\pi^+, \pi^+ \text{ over threshold}) + (CC1\pi^+, \pi^+ \text{ under threshold}) + (CC1\pi^+, \text{charge exchange}) + (CC1\pi^+, \text{double charge exchange or hadron production})$
- $CCother = CC\pi^0 + CCm\pi + CCother$
- $NC = NC0\pi + NC1\pi^+ + NC\pi^0 + NCm\pi + NCother.$

These coarser visible categories are used to illustrate the selection, where $CC1\pi^+$ is signal and the other three categories ($CCQE$, $CCother$ and NC) are backgrounds. The more detailed categories will be used to further discuss features of the selections shown in the following sections.

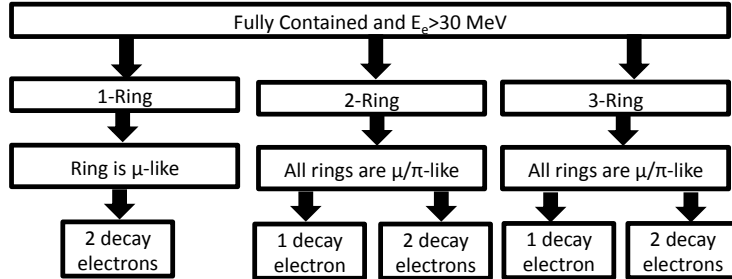


Figure 5.1: Flow chart describing $CC1\pi^+$ event selection.

5.3 Selection Cuts

The $CC1\pi^+$ selection is built around the number of rings, the particle identification of these rings, and the number of decay electrons in an event. This leads to several categories of $CC1\pi^+$ events, which are illustrated schematically in the flow chart in Fig. 5.1. Each of these selection stages will be described in more detail in the remainder of this chapter.

The first cuts made are standard SK quality cuts that require events be fully contained within the fiducial volume of the SK detector. These require that there be fewer than 16 hits in the SK outer detector, and that the $CC1\pi^+$ event vertex be reconstructed more than 2 m from the SK tank wall. There is also a minimum energy event quality cut. The visible reconstructed energy assuming that a ring is one ring electron-like is required to be greater than 30 MeV. The events remaining after each of these cuts are shown as a function of true and reconstructed neutrino energy in Fig. 5.2. In these plots the neutrino energy is calculated using the $CC1\pi^+$ reconstruction formula in Eq. 5.3. The plots are stacked histograms with each color area showing the number of events in each of the four visible categories defined in Section 5.2: CCQE, $CC1\pi^+$, CCothers and NC. This comparison illustrates how the signal and background events shift when the neutrino energy is calculated using the $CC1\pi^+$ formula and particle kinematics are reconstructed with fitQun as opposed to the true neutrino energy from the simulation. These events are scaled to T2K Run 1-8 protons on target (POT), which is 14.7×10^{20}

Table 5.1: Oscillation parameters used in this section.

$\sin^2 \theta_{12}$	$\sin^2 \theta_{13}$	$\sin^2 \theta_{23}$	Δm_{21}^2	Δm_{32}^2	δ_{CP}	Hierarchy
0.32	0.0257	0.5	$7.6 \times 10^{-5} \text{eV}^2$	$2.4 \times 10^{-3} \text{eV}^2$	0	Normal

POT, and this data normalization is used throughout unless otherwise specified. After these preliminary cuts the events are broken down by number of rings using the generic fitQun multi-ring fitter, and by number of decay electrons using the number of fitQun subevents to optimize $\text{CC1}\pi^+$ purity and efficiency.

All the plots in this section are shown assuming oscillation parameters as displayed in Table 5.1. These are selected as the nominal values because they are close to the current world best fit parameters.

The number of rings broken down by visible interaction topology for all events that pass the fully contained fiducial volume (FCFV) and minimum energy cuts are shown in Fig. 5.3. The plot has a limit of six rings as this is the maximum number of rings that fitQun reconstructs. Most of the $\text{CC1}\pi^+$ events are one, two, or three ring-like. The cut sequence, or the number of events remaining after each cut, for these preliminary cuts is shown in Fig. 5.4.

These events will be discussed both over all neutrino energy regions, and below 1.33 GeV in true neutrino energy, called the “sub-GeV” region, where neutrino oscillations are most important. This 1.33 GeV cut is the same as the one used in the SK measurements of atmospheric neutrinos.

5.3.1 One Ring ν_μ $\text{CC1}\pi^+$ Events

The selection for one ring muon events has been optimized for the standard CCQE event selection used in the current analysis [45] [80]. The selection cuts used are:

1. The event is fully contained within the SK inner detector.
2. The event is within the SK fiducial volume.
3. The event is one ring-like.

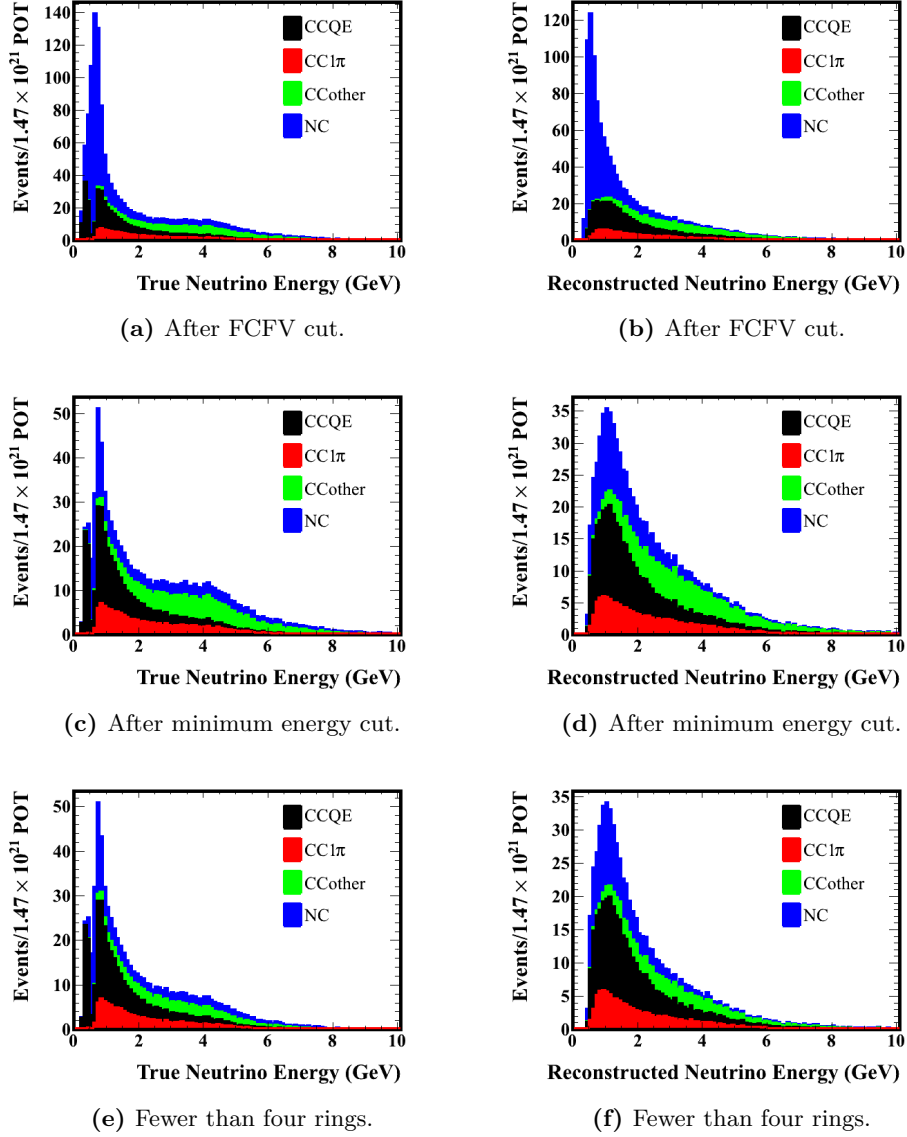


Figure 5.2: Initial quality cuts performed for ν_μ $\text{CC}1\pi^+$ selection on the T2K-SK MC as a function of true (left) and reconstructed (right) neutrino energy.

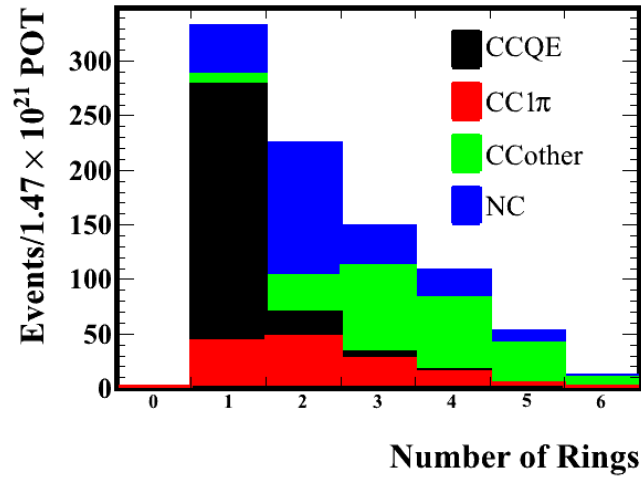


Figure 5.3: Number of rings for all events passing the FCFV and minimum energy cuts.

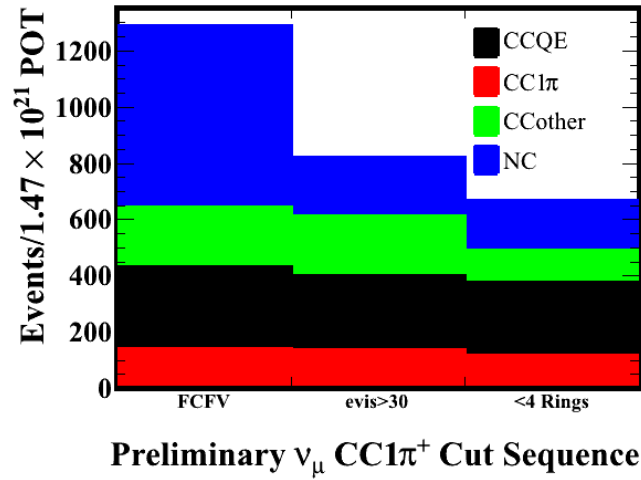


Figure 5.4: Cut sequence for preliminary event quality cuts.

4. The ring is muon-like, not electron-like as defined by $\mathcal{L}_e/\mathcal{L}_\mu < 0.2p_e$, where \mathcal{L}_e and \mathcal{L}_μ are the likelihoods of the one ring electron and muon fits and p_e is the one ring electron momentum.
5. The reconstructed muon momentum is greater than 200 MeV/c.
6. The event has zero or one decay electrons.
7. The event is muon-like, not π^+ -like as defined by $\mathcal{L}_{\pi^+}/\mathcal{L}_\mu < 0.15p_\mu$ where \mathcal{L}_{π^+} is the likelihood of the upstream charged pion, \mathcal{L}_μ is the likelihood of the one ring muon fit, and p_μ is the one ring muon momentum. This cut removes NC1 π^+ background.

This selection can be modified to select one ring ν_μ CC1 π^+ events by requiring events to have exactly two decay electrons. In these events the pion is below Cherenkov threshold, so is not directly visible, but the decay electron produced will be visible, and acts as an effective way to tag pions without seeing the ring. Requiring two decay electrons means that both the muon and the pion produce a decay electron. A similar strategy has been used to select one ring ν_e CC1 π^+ events [81].

The selection cuts used for this one ring ν_μ CC1 π^+ sample are:

1. The event is fully contained within the SK inner detector.
2. The event is within the SK fiducial volume.
3. The event is one ring-like.
4. The ring is muon-like, not electron-like.
5. The reconstructed muon momentum is greater than 200 MeV/c
6. The event is muon-like, not π^+ -like.
7. The event has two decay electrons

All of the cuts are the same as in the CCQE sample described earlier except for the decay electron cut. In Fig. 5.1, and throughout this section, cuts four, five and six are collectively referred to as muon-like PID cuts.

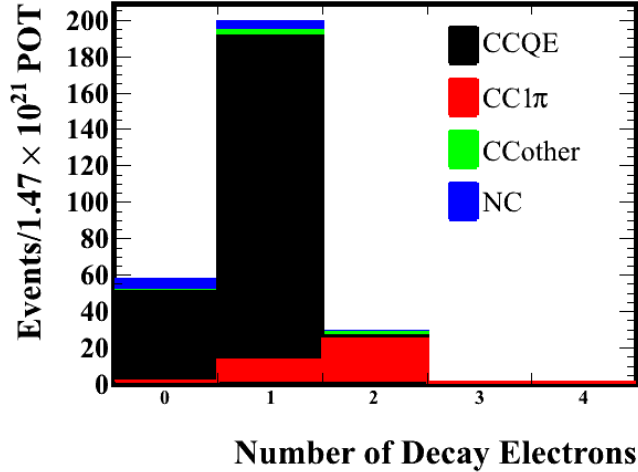


Figure 5.5: Number of decay electrons for one ring muon-like events.

The number of decay electrons for one ring muon events is shown in Fig. 5.5. Most $CC1\pi^+$ events have either one or two decay electrons. The two decay electron sample is dominantly $CC1\pi^+$. As the zero and one decay electron events are dominated by CCQE interactions and already part of the T2K selection, the one ring $CC1\pi^+$ sample will be the one ring μ -like 2 decay electron sample (1R+2de).

The event breakdown after each of these cuts, starting with the 1-ring events, is shown in Fig. 5.6.

For these one ring events where the pion kinematics can not be directly reconstructed, neutrino energy is calculated assuming that the pions produced come from the decay of a Δ in the nucleus using Eq. 5.4.

The event breakdown in true and reconstructed neutrino energy after the one ring-like cut and the particle identification cuts which correspond to cuts four to six above (muon-like ring, not a pion-like ring, reconstructed muon momentum greater than 200 MeV/c) are shown in Fig. 5.7. The final one ring $CC1\pi^+$ sample is selected by requiring that there be two decay electrons in an event, and the sample after this criteria is applied is shown in Fig. 5.8 as a function of true and reconstructed neutrino energy. The

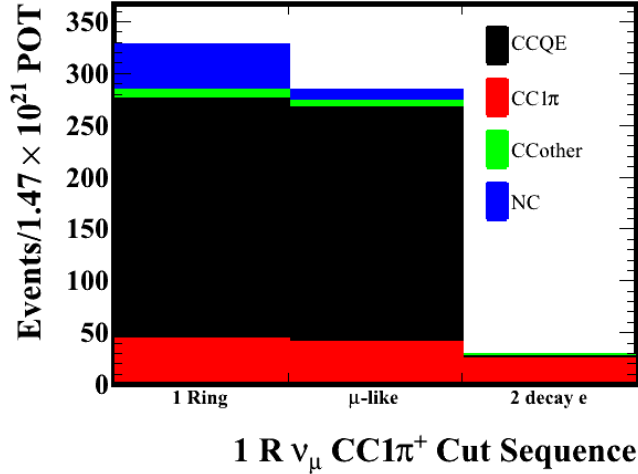


Figure 5.6: Cut sequence for one ring muon-like events after the preliminary quality cuts.

number of events remaining after each cut is shown in Table 5.2.

This one ring $CC1\pi^+$ sample contains 28.90 events, with 85% purity. Table 5.3 shows the sample purity for events over the entire possible range of neutrino energy, and for events with true neutrino energy less than 1.33 GeV in the region around the peak of the neutrino oscillation probability. The $CC1\pi^+$ purity increases to 91% in this lower energy region. Table 5.2 also shows the efficiency of the one $CC1\pi^+$ sample events from the FCFV cut and the one ring cut. This sample is 17% efficient for $CC1\pi^+$ events from the FCFV and 57% efficient for $CC1\pi^+$ events from the one ring cut.

5.3.2 Multi-Ring ν_μ $CC1\pi^+$ Events

The multi-ring $CC1\pi^+$ selection was developed by breaking events that pass the standard SK quality cuts into categories based on the number of rings and number of decay electrons.

As described in Chapter 4, fitQun has a generic multi-ring fitter that reconstructs up to six rings, and will assign either an electron-like or a pion-like PID to each of the rings that it finds. In this framework, true muon rings

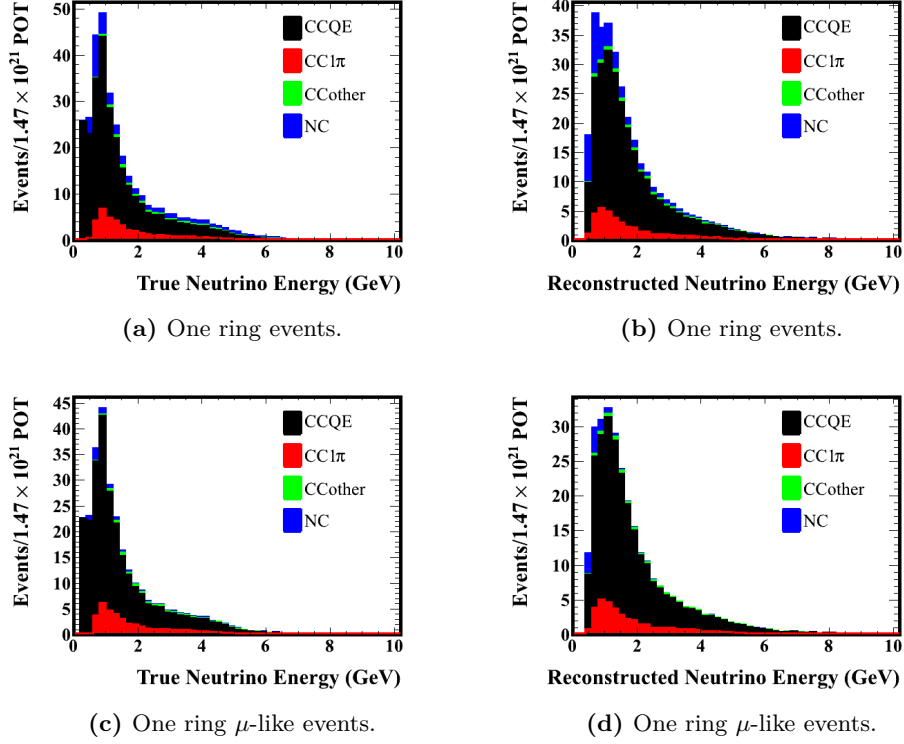
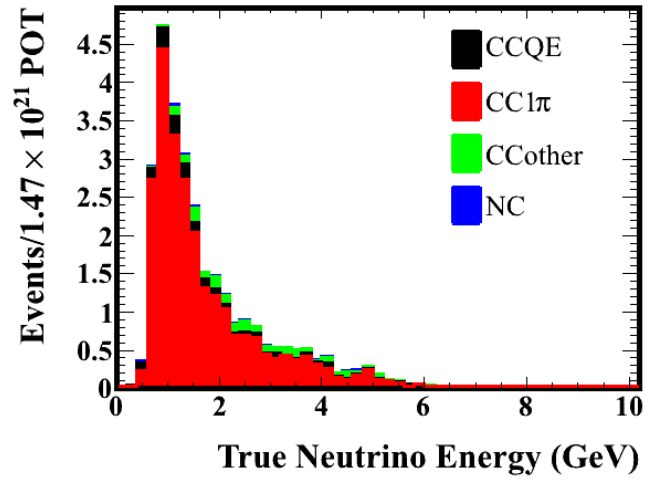


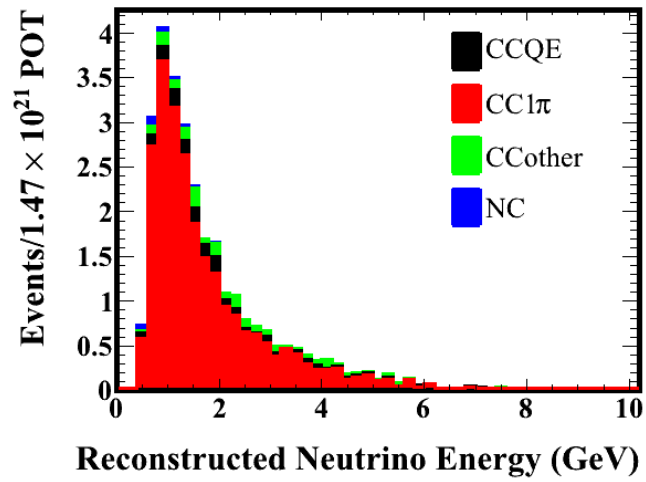
Figure 5.7: One ring events after ring counting (a,b) and PID cuts (c,d).

Table 5.2: One ring μ -like events, after each selection cut

	CCQE	CC $1\pi^+$	CCother	NC	Total
FCFV	290.40	142.69	213.50	643.15	1289.75
evis>30	261.25	138.99	212.93	210.44	823.61
1R Events	231.84	43.34	9.04	43.68	327.90
1R μ Events	225.67	40.55	7.17	10.48	283.88
1R+2de	1.86	24.73	1.98	0.33	28.90
Efficiency from FCFV(%)	0.64	17.33	0.93	0.05	2.24
Efficiency from 1R(%)	0.80	57.05	21.93	0.75	8.81



(a) True neutrino energy.



(b) Reconstructed neutrino energy.

Figure 5.8: One ring μ -like events with two decay electrons.

Table 5.3: Percent of one ring μ -like events after each selection cut

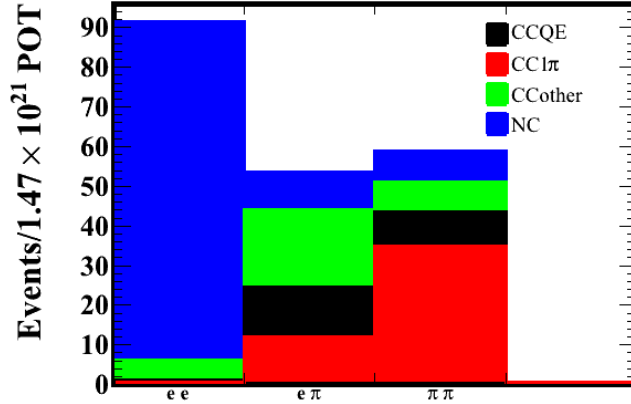
	Cut	CCQE	CC1 π^+	CCother	NC	Total
All Events	FCFV	22.52	11.06	16.55	49.87	100.00
	evis>30	31.72	16.88	25.85	25.55	100.00
	1 R Events	70.71	13.22	2.76	13.32	100.00
	1R μ Events	79.50	14.28	2.53	3.69	100.00
	1R+2de	6.45	85.55	6.86	1.14	100.00
True Sub-GeV Events	FCFV	26.21	6.25	1.95	65.59	100.00
	evis>30	53.21	13.68	4.48	28.63	100.00
	1 R Events	78.08	10.29	0.81	10.82	100.00
	1R μ Events	85.47	10.40	0.66	3.47	100.00
	1R+2de	6.51	91.16	1.50	0.82	100.00

will typically be classified as pion-like because of the similar charge profile of muons and pions. This means that ν_μ CC1 π^+ events can be selected by looking for events with rings that are all classified as pion-like. This fitter is used to select multi-ring CC1 π^+ events, and then the output of the dedicated CC1 π^+ fitter is used to calculate the neutrino energy for each of the selected events. The CC1 π^+ fitter is also used to determine which of the rings is the muon and which is the pion.

For these events, because both the muon and pion are above Cherenkov threshold and their kinematics can be reconstructed, neutrino energy is calculated using Eq. 5.3.

The sequence of cuts for multi-ring CC1 π^+ events is:

1. The event is fully contained within the SK inner detector.
2. The event is within the SK fiducial volume.
3. The event is two or three ring-like.
4. All of the rings in the event are π^+ -like
5. The event has one or two decay electrons.



Best 2 ring multi-ring fit configuration

Figure 5.9: Ring PID of best multi-ring fit output for two ring events.

Two ring events

The two ring events are selected using a combination of ring PID and number of decay electrons, as described earlier.

There are three possible combinations of ring PID for these events. They can both be pion-like ($\pi\pi$), one can be pion-like and one can be electron-like ($e\pi$), or they can both be electron-like (ee). The two ring events are broken down by best multi-ring fit configuration in Fig. 5.9. There are some $CC1\pi^+$ events in the $e\pi$ and ee categories, but these also have a significant CCoher and neutral current backgrounds.

In Table 5.4 the signal composition is broken down into the definitions from Section 5.2 for both all events and true sub-GeV events below 1.33 GeV in true neutrino energy where neutrino oscillations are most important. The ideal signal topology for two ring events is $CC1\pi^+$ with the pion above Cherenkov threshold. These are the events for which we expect to be able to reconstruct the muon and the pion rings simultaneously. For this definition of signal the highest fraction of these true visible signal events are in the two ring $\pi\pi$ category, with 24.85 events, compared to the πe and ee , which contain 6.24 and 0.37 of these events respectively. When a cut

Table 5.4: Number of two ring signal $CC1\pi^+$ events broken up across the possible two ring fit configurations.

		$CC1\pi^+$ ot	$CC1\pi^+$ ut	$CC1\pi^+$, CX	$CC1\pi^+$, mpi
All Events	All 2R	31.46	3.07	0.21	12.89
	$\pi\pi$	24.85	1.05	0.04	8.98
	$e\pi$	6.24	1.95	0.13	3.72
	ee	0.37	0.07	0.04	0.19
True Sub-GeV Events	All 2R	11.31	0.50	0.09	3.26
	$\pi\pi$	9.79	0.20	0.02	2.61
	$e\pi$	1.31	0.26	0.03	0.60
	ee	0.21	0.03	0.04	0.06

is made on true sub-GeV events the relative fraction of these ideal signal topology events that fall into the $e\pi$ and ee categories decreases. The number of $CC1\pi^+$ events with hadronic interactions that produce multiple pions also decreases because lower energy neutrino events typically produce lower energy pions and these are less likely to undergo pion producing hadronic interactions.

The number of decay electrons for the two ring pion-like events are shown in Fig. 5.10. The one and two decay electron events are both dominantly $CC1\pi^+$ events. The zero decay electron sample is dominated by neutral current events and has relatively few true $CC1\pi^+$ events, so this sample will not be included in the multi-ring $CC1\pi^+$ selection. Similarly the three decay electron sample is dominated by CCother events.

The number of events and composition in terms of neutrino interaction mode after each of these cuts, starting from the two ring events, is shown in Fig. 5.11.

True and reconstructed neutrino energy for two ring events with and without the requirement that both rings be pion-like are shown in Fig. 5.12.

The final two ring $CC1\pi^+$ samples are the one decay electron sample and the two decay electron sample. The two ring one decay electron sample (2R+1de) is shown as a function of true and reconstructed neutrino energy in Fig. 5.13. Similarly the two ring two decay electron (2R+2de) sample

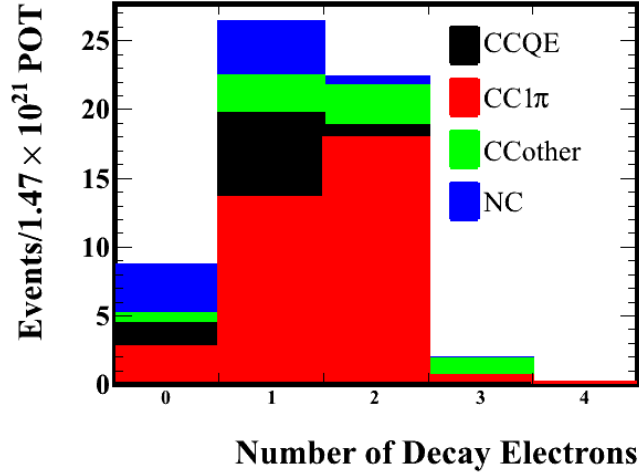


Figure 5.10: Number of decay electrons for two ring pion-like events.

is shown in Fig. 5.14. The number of events in each of these samples are in Table 5.5. The 2R+1de and 2R+2de samples are both predominantly $CC1\pi^+$ events with a purity of 52% and 81% respectively, as shown in Table 5.6. The purity increases to 55% for the 2R+1de and 96% for the 2R+2de events in the true sub-GeV neutrino energy region.

The main background for the 2R+1de sample comes from CCQE events. These are predominantly (77%) events where the proton is over Cherenkov threshold. The largest background for the 2R+2de sample, and the second largest for the one decay electron sample, is CCother. In both cases this is mostly from $CCm\pi$ events in which multiple pions exit the nucleus after the neutrino interaction.

The efficiency for the two ring $CC1\pi^+$ samples is shown in Table 5.7 relative to the number of events in the FCFV and the number of two ring events. The two ring $CC1\pi^+$ samples are 22% efficient for $CC1\pi^+$ events from the FV and 66% efficient for $CC1\pi^+$ events from the two ring cut.

Table 5.5: Number of two ring events after each selection cut.

	CCQE	CC1 π^+	CCother	NC	Total
FCFV	290.40	142.69	213.50	643.15	1289.75
evis>30	261.25	138.99	212.93	210.44	823.61
2R Events	21.71	47.63	32.18	102.52	204.04
2R π Events	8.59	34.92	7.54	7.95	58.99
2R+1de	6.06	13.53	2.72	3.88	26.20
2R+2de	0.84	17.93	2.88	0.60	22.25

Table 5.6: Sample purity after each selection cut.

	Cut	CCQE	CC1 π^+	CCother	NC	Total
All Events	FCFV	22.52	11.06	16.55	49.87	100.00
	evis>30	31.72	16.88	25.85	25.55	100.00
	2R Events	10.64	23.34	15.77	50.24	100.00
	2 R π Events	14.56	59.20	12.77	13.48	100.00
	2R+1de	23.13	51.65	10.40	14.82	100.00
	2R+2de	3.76	80.59	12.95	2.70	100.00
True Sub-GeV Events	FCFV	26.21	6.25	1.95	65.59	100.00
	evis>30	53.21	13.68	4.48	28.63	100.00
	2R Events	6.83	18.33	4.67	70.17	100.00
	2R π Events	16.03	69.36	2.50	12.11	100.00
	2R+1de	28.51	54.73	2.46	14.01	100.00
	2R+2de	2.01	95.76	2.08	0.14	100.00

Table 5.7: Efficiency of the two ring CC1 π^+ samples relative to the FCFV and the two ring cut.

		CCQE	CC1 π^+	CCother	NC	Total
Efficiency from FCFV(%)	2R+1de	2.09	9.48	1.28	0.60	2.03
	2R+2de	0.29	12.56	1.35	0.09	1.72
	Total	2.38	22.04	2.63	0.69	3.75
Efficiency from 2R (%)	2R+1de	27.91	28.41	8.46	3.79	12.84
	2R+2de	3.86	37.64	8.95	0.59	10.90
	Total	31.77	66.05	17.41	4.38	23.74

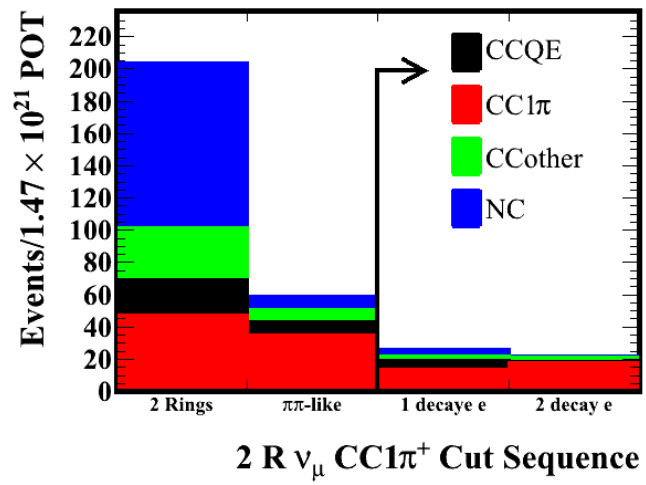
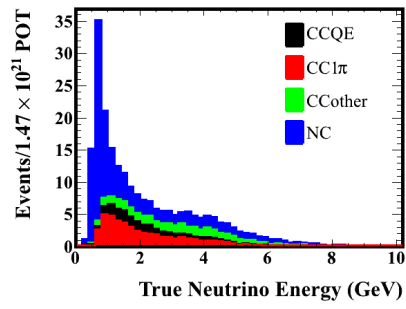
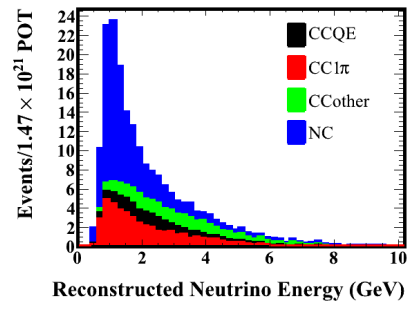


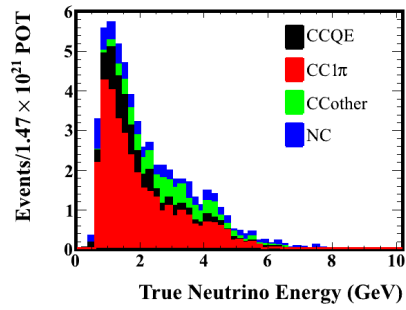
Figure 5.11: Cut sequence for two ring events. The black line indicates the final samples



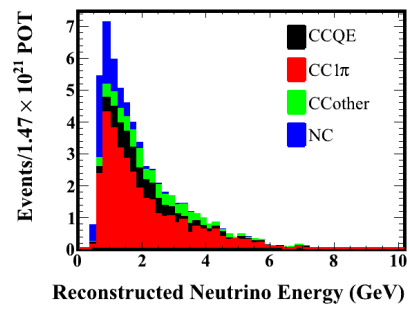
(a) Two ring events.



(b) Two ring events.

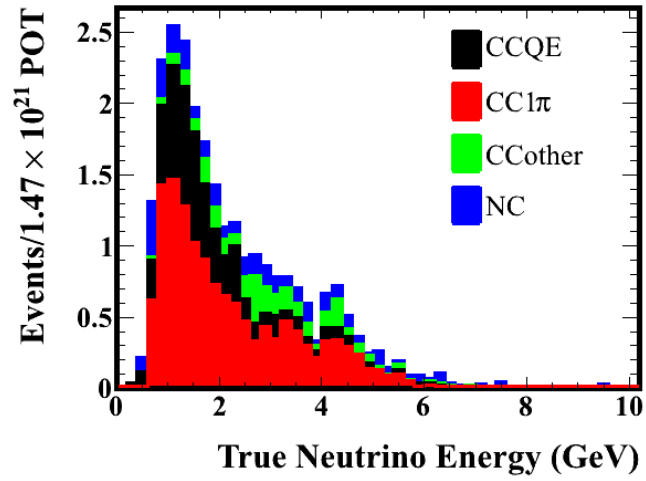


(c) Two ring π^+ -like events.

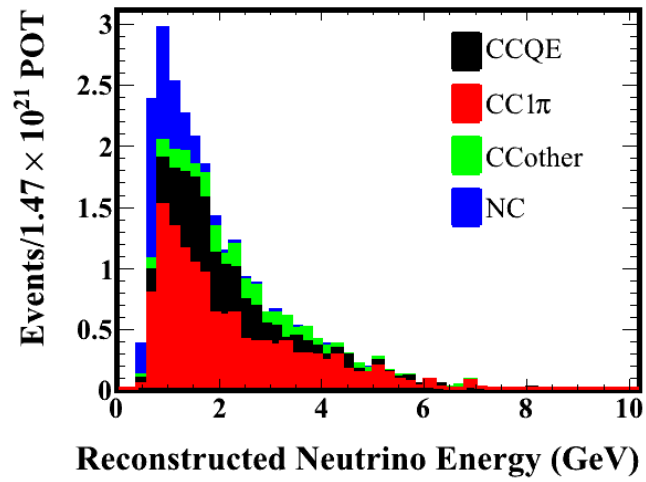


(d) Two ring π^+ -like events.

Figure 5.12: Two ring events after ring counting (a, b) and PID cuts (c, d).

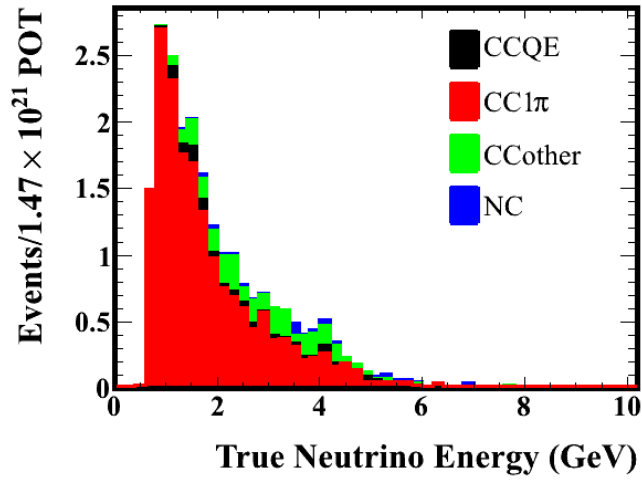


(a) True neutrino energy.

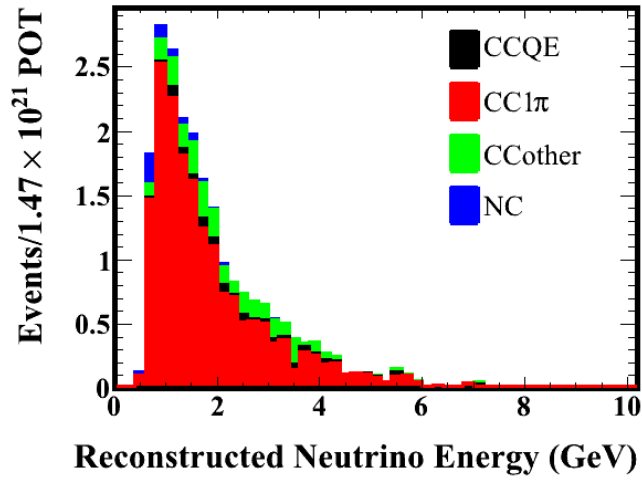


(b) Reconstructed neutrino energy.

Figure 5.13: Two ring π^+ -like events with one decay electron.



(a) True neutrino energy.



(b) Reconstructed neutrino energy.

Figure 5.14: Two ring π^+ -like events with two decay electrons.

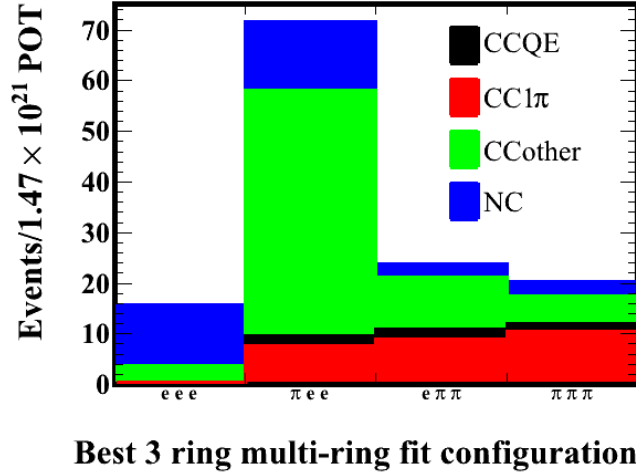


Figure 5.15: Ring PID of best multi-ring fit output for three ring events.

Three ring events

Three ring events are selected similarly to the two ring events. Here, the ideal interaction topology is that of a $CC1\pi^+$ event in which the muon and pion are both above Cherenkov threshold, and the pion scatters in the water and continues to produce light after the hadronic interaction.

Three ring events have four possible combinations of best ring PID. Rings can be either all pion like ($\pi\pi\pi$), two pion like rings and one electron-like ring ($e\pi\pi$), one pion-like ring and two electron-like rings (πee), or all electron-like (eee). The distribution of which events are best fit in each category is shown in Fig. 5.15.

As with the two ring events, the three ring events which are all identified as pion-like contain the highest fraction of the target sample of events with one muon and one pion above Cherenkov threshold. There are still relatively significant fractions of these signal events in the other categories, but these come with much higher backgrounds of multi-pion events, and other charged current interactions, and so will not be included in the final selection.

The events that are best fit with three rings and three pion-like rings are

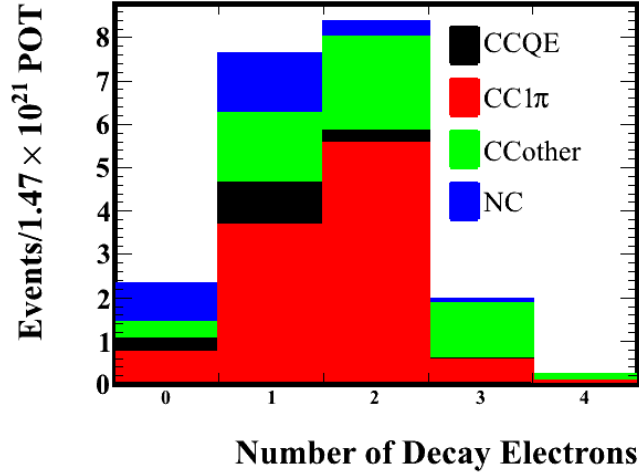


Figure 5.16: Number of decay electrons for three ring events.

shown in Fig. 5.18 as a function of true and reconstructed neutrino energy. The dominant background in these events are CCother interactions. Three ring events are more common at higher energy because the cross section for multi-particle producing CCother events is higher, and because higher energy particles tend to produce more rings.

The number of decay electrons for events with three pion-like rings is shown in Fig. 5.16. As with the two ring events, the zero decay electron events have a large neutral current component, but the one and two decay electron events both have relatively high CC1π⁺ fractions. The events with three decay electrons are primarily CCother.

The cut sequence of the three ring events is shown in Fig. 5.17.

True and reconstructed neutrino energy for three ring events with and without the requirement that both rings be pion-like are shown in Fig. 5.18.

The final three ring CC1π⁺ samples are the one decay electron sample and the two decay electron sample. The three ring one decay electron sample (3R+1de) is shown in Fig. 5.19 as a function of true and reconstructed neutrino energy. The three ring two decay electron sample (3R+2de) is similarly shown in Fig. 5.20.

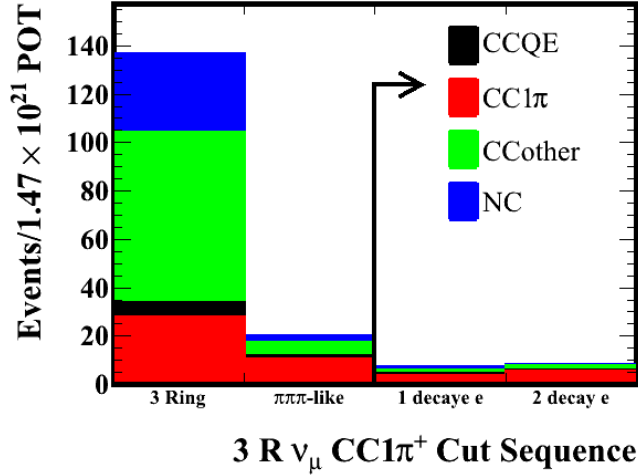


Figure 5.17: Cut sequence for three ring $\text{CC1}\pi^+$ events. The black arrow indicates the final samples.

Table 5.8: Number of three ring events after each selection cut

	CCQE	CC1 π^+	CCother	NC	Total
FCFV	290.40	142.69	213.50	643.15	1289.75
evis>30	261.25	138.99	212.93	210.44	823.61
3R Events	5.53	28.14	70.80	32.03	136.50
3R π Events	1.53	10.53	5.55	2.70	20.30
3R+1de	0.93	3.66	1.56	1.39	7.54
3R+2de	0.29	5.50	2.13	0.34	8.26

As shown in Table 5.8, there are 7.54 events in the 3R+1de sample and 8.26 events in the 3R+2de sample. These have a $\text{CC1}\pi^+$ fraction of 48% and 66% respectively, as shown in Table 5.10. The purity increases to 59% for the 3R+1de sample and 95% for the 3R+2de sample when only sub-GeV events are considered. Table 5.9 shows the efficiency for selecting events of each topology relative to the total number of events in the fiducial volume, and the number of events in the three ring sample. The three ring $\text{CC1}\pi^+$ samples are 6% efficient for selecting $\text{CC1}\pi^+$ events from the FCFV and 33% efficient for selecting $\text{CC1}\pi^+$ events from the three ring cut.

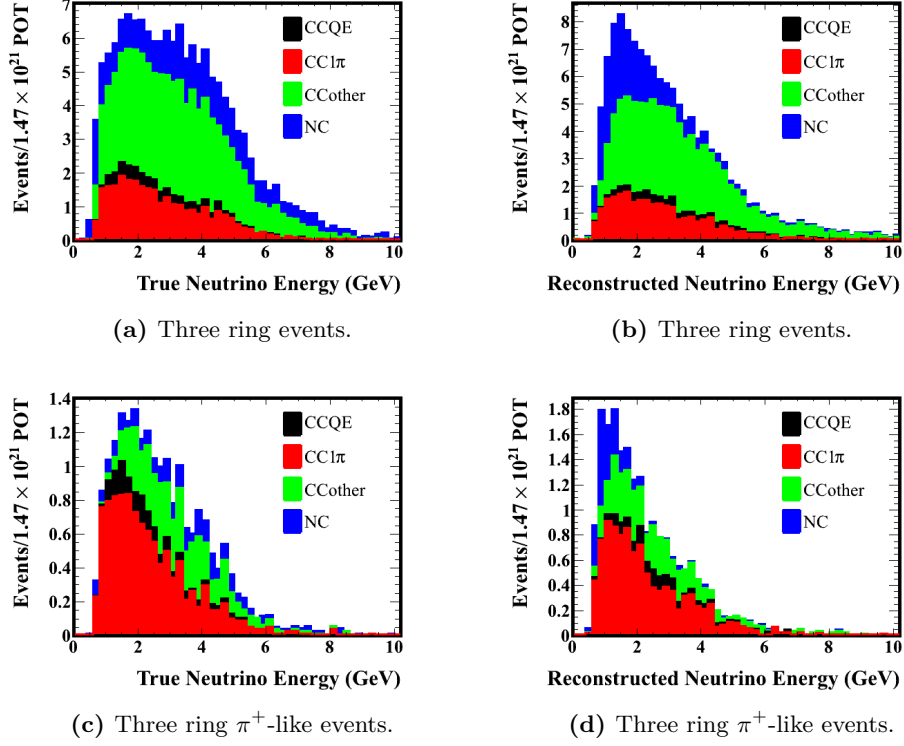
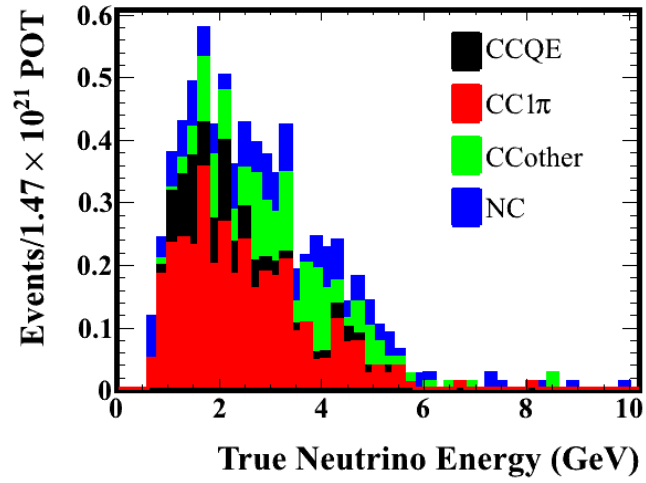


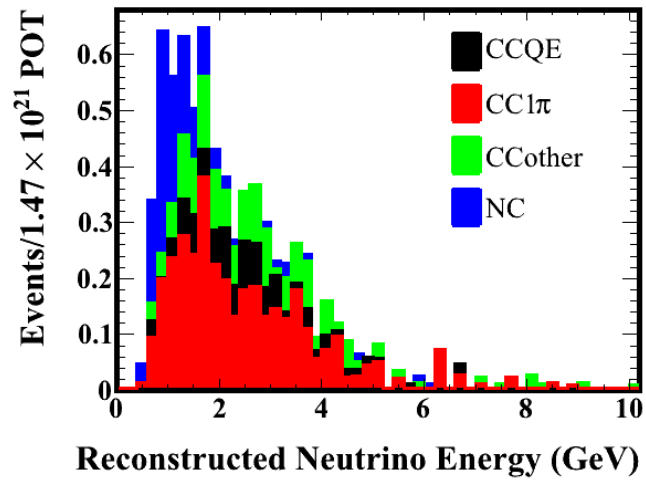
Figure 5.18: Three ring events after ring counting (a, b) and PID cuts (c, d).

Table 5.9: Efficiency of selecting three ring events from the FCFV and the three ring cut.

		CCQE	CC1 π^+	CCother	NC	Total
Efficiency from FCFV (%)	3R+1de	0.32	2.57	0.73	0.22	0.58
	3R+2de	0.10	3.86	1.00	0.05	0.64
	Total	0.42	6.43	1.73	0.27	1.22
Efficiency from 3R (%)	3R+1de	16.76	13.02	2.20	4.33	5.52
	3R+2de	5.17	19.56	3.01	1.05	6.05
	Total	21.93	32.58	5.21	5.38	11.05

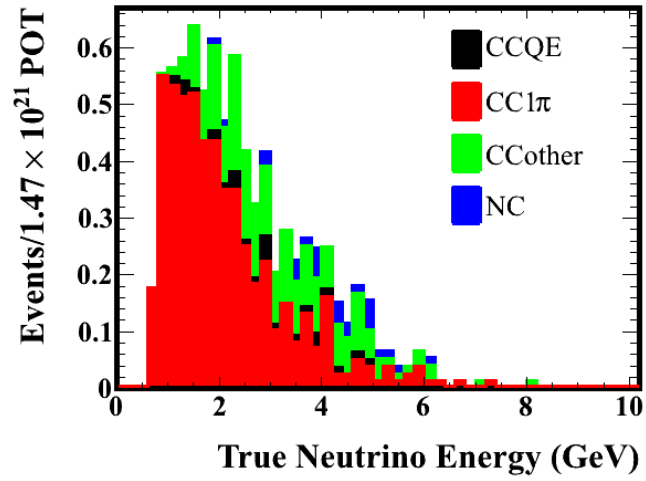


(a) True neutrino energy.

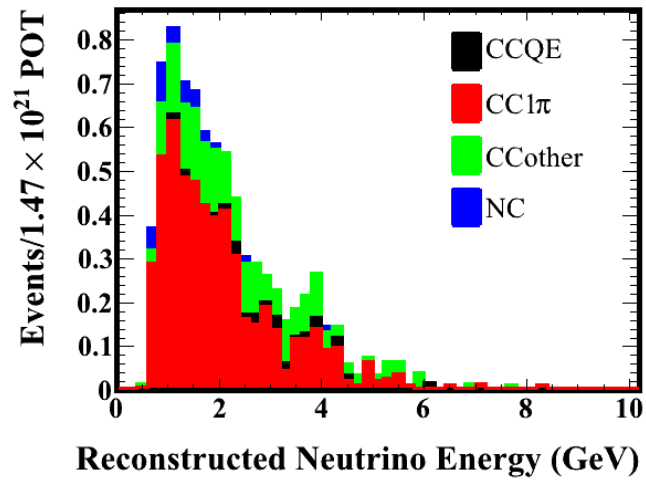


(b) Reconstructed neutrino energy.

Figure 5.19: Three ring one decay electron π^+ -like events.



(a) True neutrino energy.



(b) Reconstructed neutrino energy.

Figure 5.20: Three ring two decay electron π^+ -like events.

Table 5.10: Percent of sample, 3 ring events, after each selection cut

	Cut	CCQE	CC1 π^+	CCother	NC	Total
All Events	FCFV	22.52	11.06	16.55	49.87	100.00
	evis>30	31.72	16.88	25.85	25.55	100.00
	3R Events	4.05	20.61	51.87	23.47	100.00
	3R π Events	7.54	51.86	27.32	13.28	100.00
	3R+1de	12.30	48.62	20.69	18.39	100.00
	3R+2de	3.47	66.65	25.81	4.08	100.00
True Sub-GeV Events	FCFV	26.21	6.25	1.95	65.59	100.00
	evis>30	53.21	13.68	4.48	28.63	100.00
	3R Events	4.14	26.90	41.75	27.22	100.00
	3 R π Events	8.85	76.30	3.64	11.21	100.00
	3R+1de	17.29	59.64	3.32	19.75	100.00
	3R+2de	2.15	95.46	2.39	0.00	100.00

5.4 Summary of $\text{CC1}\pi^+$ Samples

There are five $\text{CC1}\pi^+$ samples defined in the earlier sections: one ring with two decay electrons (1R+2de), two rings with one decay electron(2R+1de), two rings with two decay electrons(2R+2de), three rings with one decay electron (3R+1de) and three rings with two decay electrons (3R+2de). The MC expectation is 28.90 events in the 1R+2de sample, 26.20 events in the 2R+1de sample, 22.25 events in the 2R+2de sample, 7.54 events in the 3R+1de sample, and 8.26 events in the 3R+2de sample. These range in purity from 48-85%. These final samples, along with the relative event fraction of each type of visible neutrino interaction, are summarized in Table 5.12. Two additional summary samples are also defined here, the multi-ring sum (MR sum), which is the sum of the two and three ring events, and the total sample which is the sum of all five samples. The multi-ring sum MC expectation is 64 events with 60% purity. The MC expectation for the total $\text{CC1}\pi^+$ sample, including all the events from the five previously discussed samples, is 93 events with 70% purity, which is similar to the purity of the current T2K CCQE signal samples. The purity below 1.33 GeV increases to 82% across all samples, and 90-95% for the two decay electron samples, which means that these samples are especially pure in the region where neutrino oscillations are the most important. The multi-ring sample is 28.38% efficient for selecting $\text{CC1}\pi^+$ events from the FCFV, and the total sample is 45.71% efficient for selecting $\text{CC1}\pi^+$ events from the FCFV.

There are currently 240 CCQE-like ν_μ events in the beam data used in the T2K analysis [45]. According to the MC prediction the addition of these five $\text{CC1}\pi^+$ samples will increase the number of ν_μ signal events by approximately 40%.

5.5 Background from $\bar{\nu}_\mu$, ν_e and $\bar{\nu}_e$ Interactions

There are also additional backgrounds to these muon neutrino $\text{CC1}\pi^+$ samples that come from beam neutrinos of other flavors interacting at SK. The possible backgrounds are $\bar{\nu}_\mu$, ν_e and $\bar{\nu}_e$ interactions. These backgrounds are compared to the ν_μ $\text{CC1}\pi^+$ samples in Table 5.13. The $\bar{\nu}_\mu$ come from the

Table 5.11: Number of events in each of the $CC1\pi^+$ samples.

Event Category	CCQE	$CC1\pi^+$	CCother	NC	Total
1R+2de	1.86	24.73	1.98	0.33	28.90
2R+1de	6.06	13.53	2.72	3.88	26.20
2R+2de	0.84	17.93	2.88	0.60	22.25
3R+1de	0.93	3.66	1.56	1.39	7.54
3R+2de	0.29	5.50	2.13	0.34	8.26
MR sum	8.12	40.62	9.29	6.21	64.25
Total	9.98	65.35	11.27	6.54	93.15
MR sum efficiency from FCFV(%)	2.80	28.38	4.36	0.96	4.97
Total efficiency from FCFV(%)	3.44	45.71	5.29	1.01	7.21

Table 5.12: Number of events in each of the $CC1\pi^+$ samples below 1.33 GeV in true neutrino energy.

Event Category	CCQE	$CC1\pi^+$	CCother	NC	Total
1R+2de	0.89	12.52	0.21	0.11	13.74
2R+1de	2.24	4.31	0.19	1.10	7.87
2R+2de	0.16	7.70	0.17	0.01	8.04
3R+1de	0.18	0.61	0.03	0.20	1.03
3R+2de	0.03	1.55	0.04	0.00	1.62
MR sum	2.61	14.17	0.43	1.31	18.56
Total	3.50	26.69	0.64	1.42	32.30

wrong sign background of π^- in the beam. The beam ν_e and beam $\bar{\nu}_e$ come from the small components of the T2K beam that are not muon neutrinos. The signal ν_e come from muon neutrino oscillations into electron neutrinos. This background is 4.54 events in the multi-ring samples, and 5.25 events in the total sample, mostly coming from the $\bar{\nu}_\mu$ events. This is about a 6% background on the sum of the four multi-ring samples, and 5% on the sum of all five $CC1\pi^+$ samples.

5.6 Neutrino Energy Calculation Resolution

There are two possible ways to calculate neutrino energy for $CC1\pi^+$ events. One assumes that the pion is created in the nucleus by the decay of a Δ , and

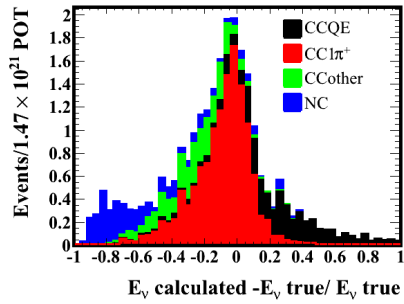
Table 5.13: Background from non- ν_μ beam neutrino interactions.

	ν_μ	$\bar{\nu}_\mu$	Beam ν_e	Beam $\bar{\nu}_e$	Signal ν_e	Signal $\bar{\nu}_e$
1R+2de	28.90	0.69	0.008	0.002	0.001	0.012
2R+1de	26.19	2.78	0.136	0.018	0.014	0.251
2R+2de	22.24	0.37	0.023	0.000	0.002	0.025
3R+1de	7.53	0.58	0.047	0.006	0.005	0.066
3R+2de	8.25	0.19	0.010	0.001	0.001	0.015
MR sum	64.23	3.92	0.215	0.025	0.021	0.356
Total	93.14	4.61	0.223	0.027	0.022	0.368

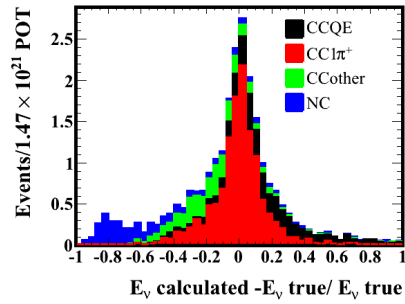
therefore assumes that the recoiling hadronic system has the Δ mass, along with the reconstructed muon kinematics to calculate neutrino energy as in Eq 5.4. The second uses both the muon and the pion reconstructed kinematics to calculate neutrino energy. In the case of the one ring $CC1\pi^+$ sample only the Δ formula may be used because the pion is below Cherenkov threshold and its kinematics cannot be reconstructed. To decide between use of the Δ reconstruction formula or the muon and pion kinematics formula for the multi-ring events, comparisons of the energy resolution are made for all of the two and three ring selected samples, shown in Fig. 5.21 and 5.22 respectively. The energy resolution is defined as $(E_{\text{calculated}} - E_{\text{true}})/E_{\text{true}}$. These results are quantified by calculating the standard deviation and mean for both the total sample distribution and the signal $CC1\pi^+$ events individually. From the results in Table 5.14, the mean appears to be better when the $CC1\pi^+$ formula is used for both the signal alone, and the signal plus background distributions. The standard deviation is about the same in both cases. This means that it would be best to use the $CC1\pi^+$ formula with the muon and pion kinematics to reconstruct neutrino energy because the neutrino energy measurement will be better.

Table 5.14: Mean and standard deviations of the neutrino energy resolution when the Δ formula is used compared to when the $CC1\pi^+$ formula is used to calculate neutrino energy.

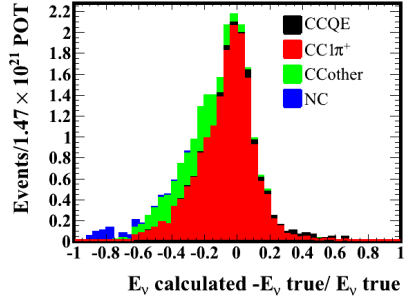
		Mean		Standard Deviation	
		Δ	$CC1\pi^+$	Δ	$CC1\pi^+$
	Sample	Formula	Formula	Formula	Formula
Signal $CC1\pi^+$	2R+1de	-0.093	0.00035	0.19	0.19
	2R+2de	-0.067	0.026	0.18	0.20
	3R+1de	-0.16	0.0082	0.22	0.22
	3R+2de	-0.14	0.0077	0.22	0.22
Signal $CC1\pi^+$ + Background	2R+1de	0.12	-0.062	0.34	0.33
	2R+2de	-0.11	-0.035	0.23	0.25
	3R+1de	-0.25	-0.13	0.32	0.34
	3R+2de	-0.23	-0.11	0.26	0.27



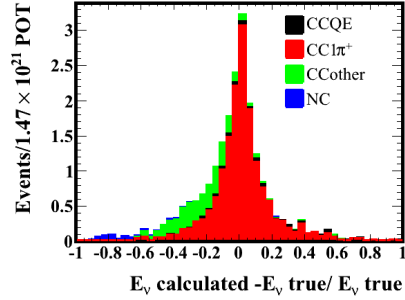
(a) 2R+1de sample with neutrino energy calculated using Delta formula.



(b) 2R+1de sample with neutrino energy calculated using $CC1\pi^+$ formula.

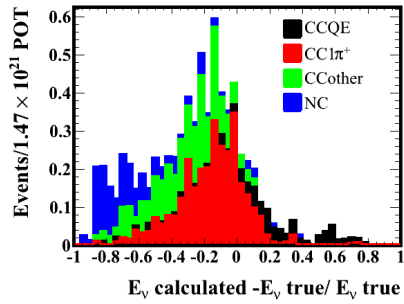


(c) 2R+2de sample with neutrino energy calculated using Delta formula.

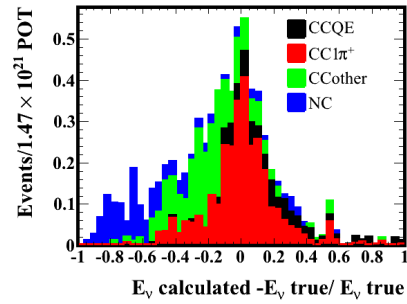


(d) 2R+2de sample with neutrino energy calculated using $CC1\pi^+$ formula.

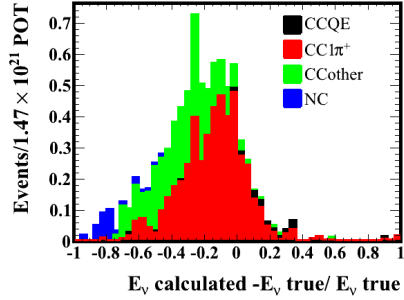
Figure 5.21: Energy resolution using Δ formula and $CC1\pi^+$ formula for selected two ring samples.



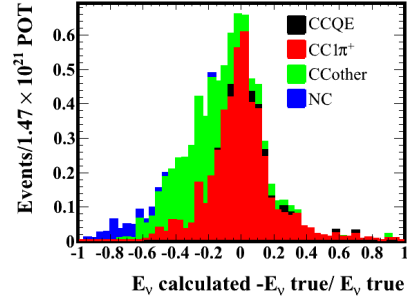
(a) 3R+1de sample with neutrino energy calculated using Delta formula.



(b) 3R+1de sample with neutrino energy calculated using $CC1\pi^+$ formula.



(c) 3R+2de sample with neutrino energy calculated using Delta formula.



(d) 3R+2de sample with neutrino energy calculated using $CC1\pi^+$ formula.

Figure 5.22: Energy resolution using Δ formula and $CC1\pi^+$ formula for selected three ring samples.

5.7 Oscillation Variations

All of the initial sample studies done and presented until this point have assumed the default oscillation parameters built into the T2K-SK MC as shown in Table 5.1. The $\text{CC1}\pi^+$ samples were also studied under a larger variety of oscillation parameters, as defined by a grid of muon neutrino oscillation parameters: $\sin^2 \theta_{23} = \{0.4, 0.5, 0.6\}$ and $\Delta m_{32}^2 \text{ (eV}^2\text{)} = \{0.0020, 0.0024, 0.0025, 0.0030\}$. The focus here is on $\sin^2 \theta_{23}$ and Δm_{32}^2 because this is a sample of additional muon neutrino events. The oscillation probability was calculated on an event by event basis for the T2K-SK MC. This is a function of the neutrino energy once the oscillation parameters are specified. These weights are applied to scale to these additional oscillation possibilities.

This will demonstrate that these selected $\text{CC1}\pi^+$ samples are sensitive to the neutrino oscillation parameters.

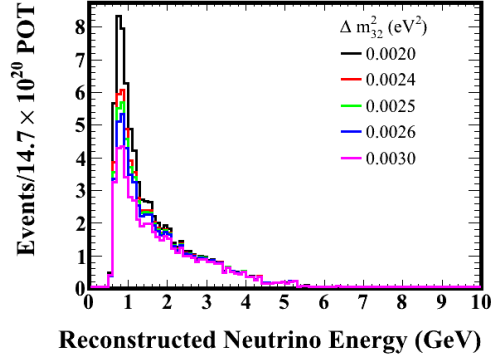
The variation in the number of events in the sum of the four multi-ring samples as a function of reconstructed neutrino energy are illustrated in Fig. 5.23. The same variations for the total $\text{CC1}\pi^+$ sample are shown in Fig. 5.24. There is almost no dependence on the oscillation parameters above 1.33 GeV in reconstructed neutrino energy because the neutrino oscillation probability is much smaller at these higher energies for the T2K baseline.

To help illustrate these variations the total number of events in each of these samples is plotted in Fig. 5.26. It is of note that there is a degeneracy in the oscillation probability at $\sin^2 \theta_{23} \approx 0.511$ which means that points on either side of this value have nearly the same oscillation probability, which results in the same number of events. This comes from the fact that the disappearance probability increases to a maximum at $\sin^2 \theta_{23} \approx 0.511$ and then decreases again.

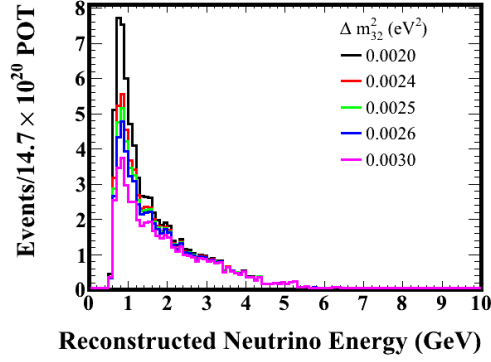
The number of events varies about 20% from the nominal oscillation parameters in Δm_{32}^2 , with more events at lower values and fewer events at higher values. This is relatively consistent for both the multi-ring samples alone and the one ring and multi-ring samples combined.

The $\text{CC1}\pi^+$ efficiency was also calculated as a function of these different oscillation parameters and is shown in Fig. 5.28. Here the efficiency is defined

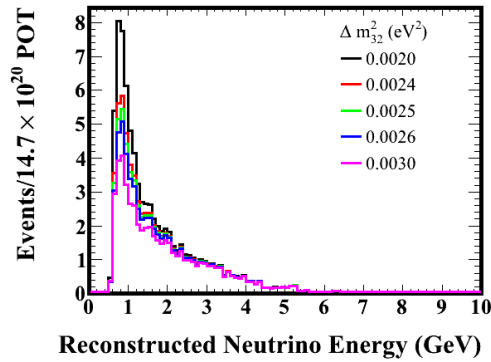
as the total number of true visible $\text{CC}1\pi^+$ events in the sample divided by the total number of events in the sample. The efficiency is relatively flat in $\sin^2 \theta_{23}$. Depending on the value of Δm_{32}^2 the purity of the multi-ring sample varies from 59-67%, while the total sample varies from 66-74%. In the region below 1.33 GeV in true neutrino energy where neutrino oscillations occur the purity of the multi-ring sample is 66-80%, and for the total sample is 76-86%. The efficiency is better for higher values of Δm_{32}^2 .



(a) $\sin^2 \theta_{23} = 0.4$.

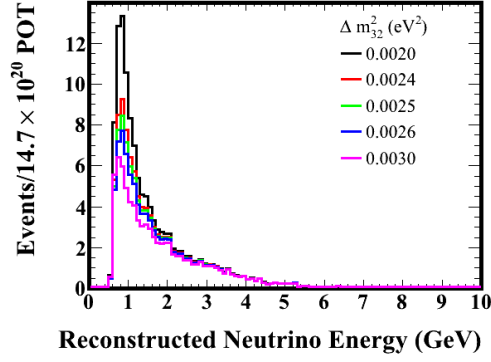


(b) $\sin^2 \theta_{23} = 0.5$.

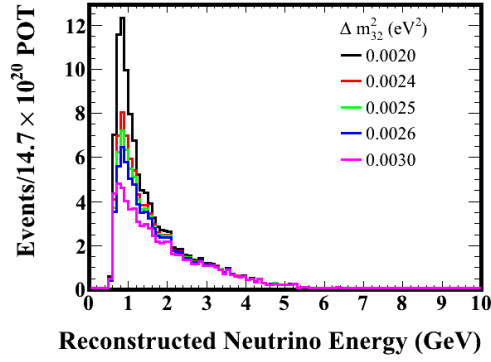


(c) $\sin^2 \theta_{23} = 0.6$.

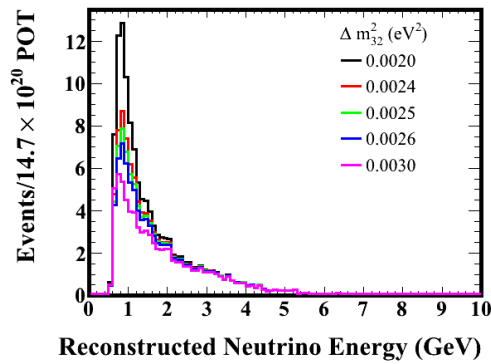
Figure 5.23: Number of events in the four multi-ring samples as a function of reconstructed neutrino energy. Each plot is at a fixed value of $\sin^2 \theta_{23}$, and illustrates each of the Δm_{32}^2 variations.



(a) $\sin^2 \theta_{23} = 0.4$.

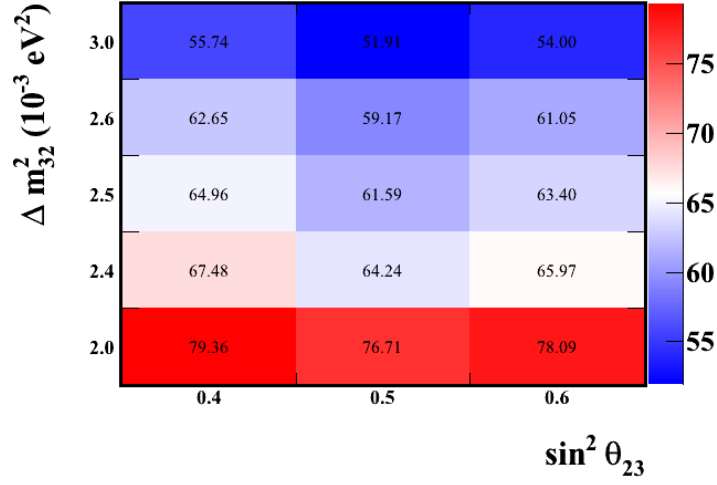


(b) $\sin^2 \theta_{23} = 0.5$.

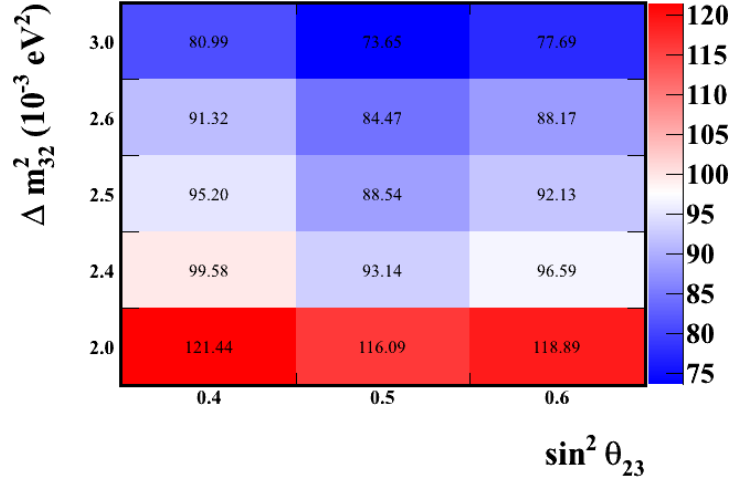


(c) $\sin^2 \theta_{23} = 0.6$.

Figure 5.24: Number of events in all five ν_μ CC1 π^+ samples as a function of reconstructed neutrino energy. Each plot is at a fixed value of $\sin^2 \theta_{23}$, and illustrates each of the Δm_{32}^2 variations.

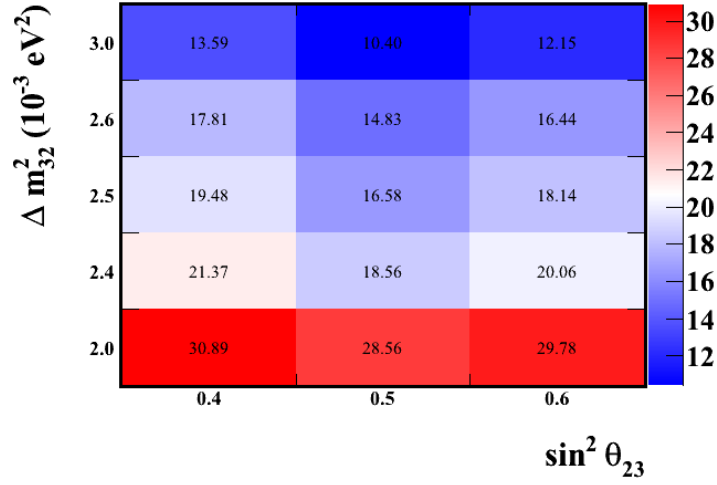


(a) Sum of the four multi-ring $\text{CC1}\pi^+$ samples.

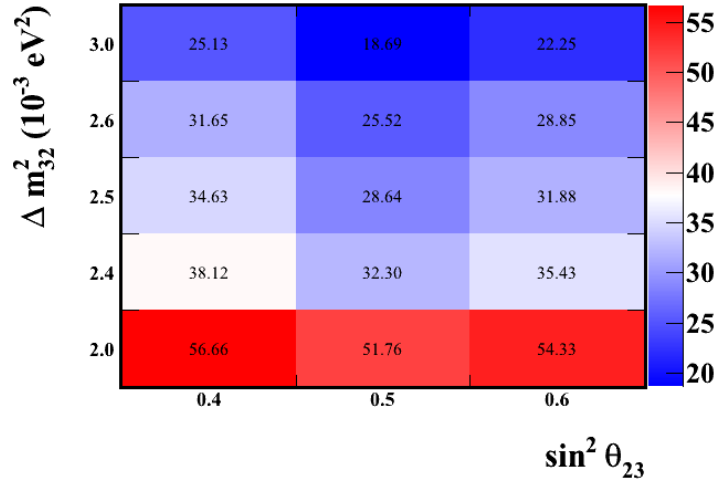


(b) Sum of the one ring and multi-ring $\text{CC1}\pi^+$ samples.

Figure 5.25: Number of events in the multi-ring samples and all samples illustrated in the grid of calculated oscillation parameters.

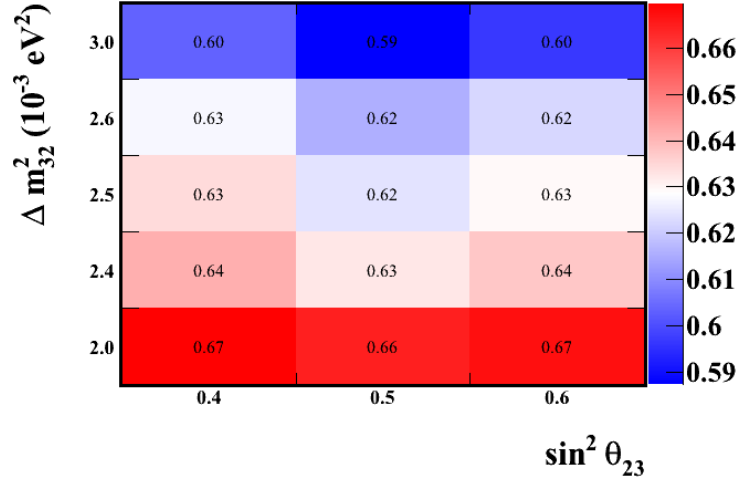


(a) Sum of four multi-ring $\text{CC}1\pi^+$ samples.

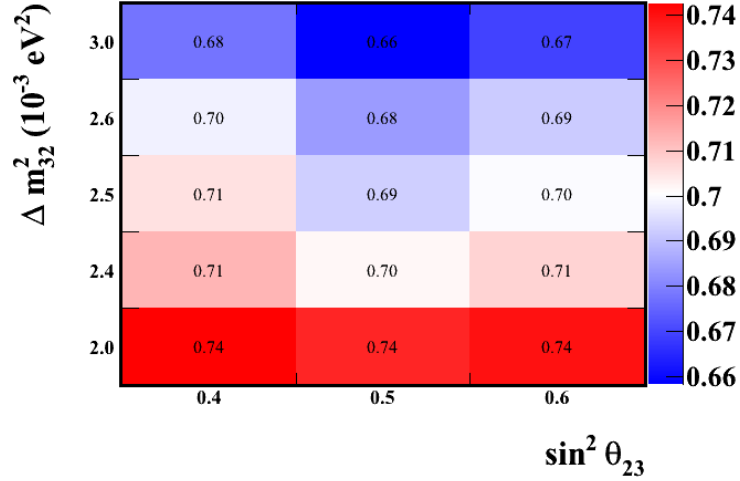


(b) Sum of one ring and multi-ring $\text{CC}1\pi^+$ samples.

Figure 5.26: Number of events in the multi-ring samples and all samples illustrated in the grid of calculated oscillation parameters for events with true neutrino energy below 1.33 GeV.

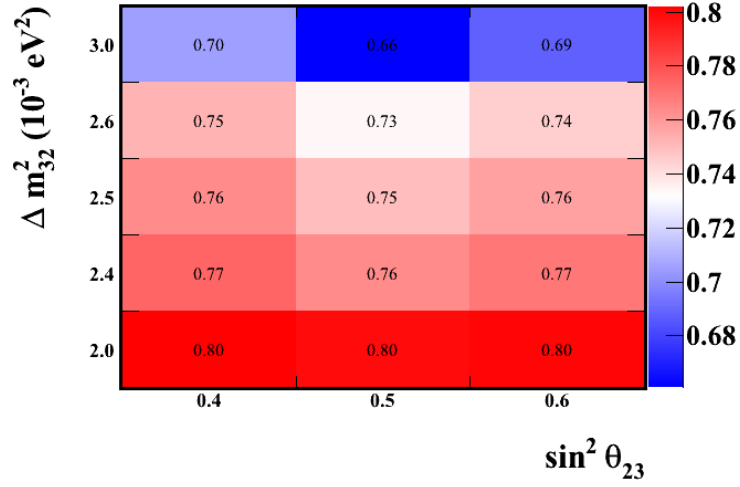


(a) Sum of four multi-ring $\text{CC1}\pi^+$ samples.

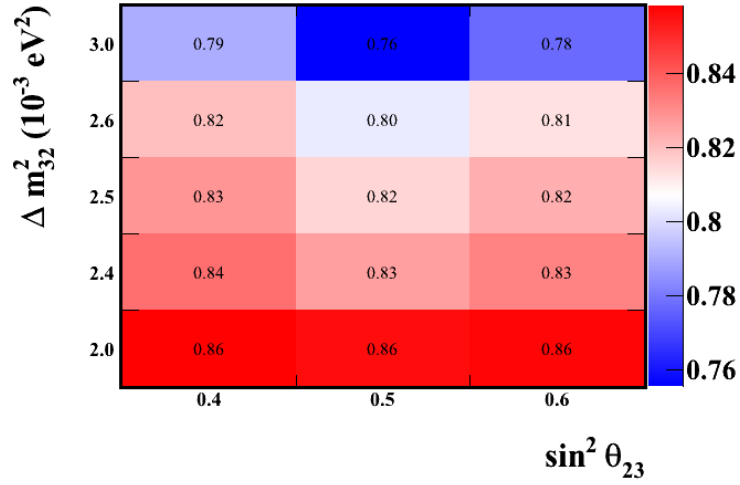


(b) Sum of one ring and multi-ring $\text{CC1}\pi^+$ samples.

Figure 5.27: $\text{CC1}\pi^+$ efficiency in the multi-ring samples and all samples illustrated in the grid of calculated oscillation parameters.



(a) Sum of four multi-ring $\text{CC1}\pi^+$ samples.



(b) Sum of one ring and multi-ring $\text{CC1}\pi^+$ samples.

Figure 5.28: $\text{CC1}\pi^+$ efficiency in the multi-ring samples and all samples illustrated in the grid of calculated oscillation parameters for events with true neutrino energy below 1.33 GeV.

Chapter 6

Charged Pion Systematic Error Evaluation

It is necessary to evaluate the systematic errors associated with the samples presented in Chapter 5. The main errors can be grouped into three categories: those associated with the neutrino interaction on water, those associated with the pion interactions in the target nucleus and detector, and those associated with the detector response.

6.1 Neutrino Interaction Uncertainties

The error associated with the neutrino interaction addresses how sensitive the selection is to the properties of the neutrino interaction. In particular we are interested in how the number of particles produced in a neutrino interaction and their kinematics affect what is visible in the SK detector. This comes in two parts: the properties of the particles directly produced by the neutrino interaction, and any re-interaction these particles undergo before exiting the nucleus.

The error associated with the properties of the particles directly produced by the neutrino interaction can be evaluated before any re-interaction in the nucleus or the detector when there is just a muon and a pion. Different neutrino interaction models predict different pion momentum spectra

from $CC1\pi^+$ interactions which may affect whether or not a pion is above Cherenkov threshold, and will change the overall detection efficiency. This effect can also result in migrations between the one ring and multi-ring samples. Similarly, different neutrino interaction models also predict different pion multiplicities will be produced by neutrino interactions. The momentum of these pions, and whether they produce decay electrons could change the size of the backgrounds in the $CC1\pi^+$ samples.

Pions produced in the nucleus by neutrino interactions may also undergo FSI in the nucleus. FSI may also affect the total number of visible positively charged pions produced, because if a pion absorbs or charge exchanges inside the nucleus then there will be no positively charged pion to detect. Similarly a pion that was initially produced above Cherenkov threshold may scatter below threshold by the time it exits the nucleus. These effects will be discussed along with pion re-interactions in the SK water in Section 6.2, as a similar methodology is used to evaluate them both.

6.1.1 Generator Comparisons of Visible $CC1\pi^+$ Signal

The output of different neutrino interaction generators are compared to understand how the properties of the particles produced may vary when different pion production models are used.

NEUT is the nominal neutrino interaction generator used to generate the T2K-SK MC [67]. The pion production model in NEUT, as described in Chapter 2, is compared to two different pion production models within the GENIE generator, referred to as the default and the alternate GENIE models, as well as to the NUWRO pion production model. The default GENIE model is an implementation of the Rhein-Sehgal model which uses only 16 of the resonances and does not take into account the lepton mass term [68]. The alternate GENIE model is an implementation of the Berger Seghal model which is similar to the default GENIE model except that it takes the lepton mass term into account [82]. The NUWRO model only includes an implementation of the $\Delta(1232)$ resonance, and then extrapolates the DIS model down to cover pion production from higher resonances [83].

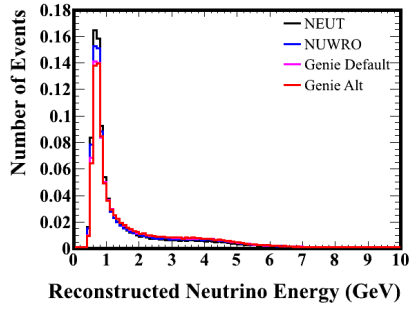
Events were generated with each of these neutrino interaction generators using the T2K beam flux at SK. True visible $CC1\pi^+$ signal events are selected by looking for events with exactly one true muon and true pion after the neutrino interaction, but before any final state or secondary re-interaction. Any number of nucleons are allowed, but no other types of particles. These signal events can be characterized by six kinematic parameters: neutrino energy, the momentum of the muon and the pion, and the angles between the neutrino and muon, neutrino and pion, and muon and pion. The kinematics from each generator are compared in Fig. 6.1. These kinematics are of interest because the Cherenkov threshold at SK affects what events have muons and pions with visible rings. If the muon and pion rings are overlapping because the angle between the direction of the two particles is very small then it is also more difficult to well reconstruct the particles and this introduces a systematic error.

6.1.2 Reweighting to Different Signal Models

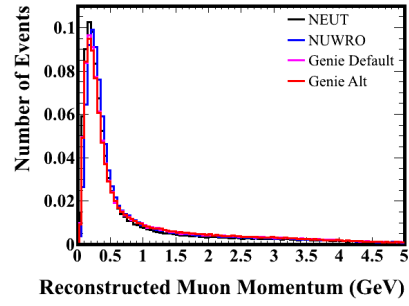
Using these comparisons between generators it is possible to study how much the selected $CC1\pi^+$ samples will vary if the underlying signal distribution were those of the other generators instead of that of the NEUT generated T2K-SK MC. Instead of regenerating the full MC with each of these generators, which is very computationally intensive, it is possible to weight the signal events in the selected samples to these underlying kinematic distributions to see the effect on the size of the sample.

One Dimensional Reweighting

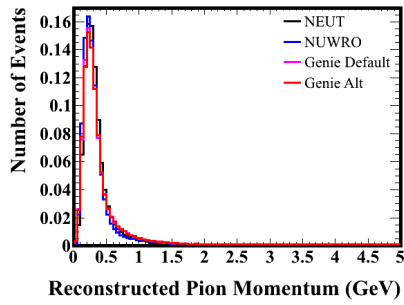
The simplest way to do the reweighting is to take the ratio of the different generator models to the NEUT default in each of the kinematic variables shown in Fig. 6.1. These ratios are one dimensional weights as a function of each of kinematic variable and are illustrated in Fig. 6.2. These weights can then be applied to the selected signal events to see a general indication of how the models differ. The result of applying these weights is shown in Table 6.1 for the sum of all multi-ring events. This table illustrates that



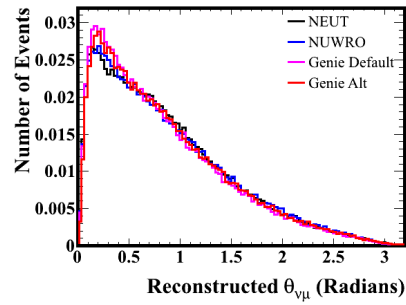
(a) Neutrino energy.



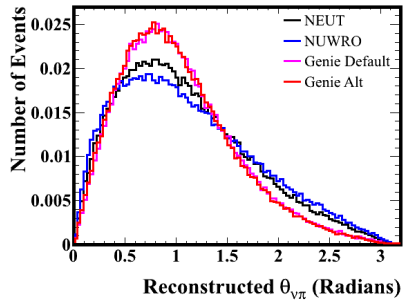
(b) Muon momentum.



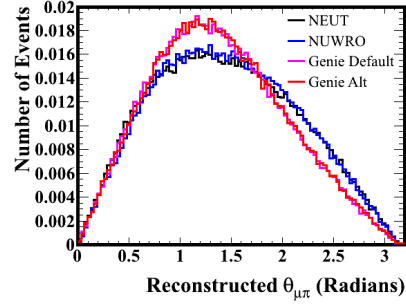
(c) Pion momentum.



(d) Angle between neutrino and muon.



(e) Angle between neutrino and pion.



(f) Angle between muon and pion.

Figure 6.1: Comparisons between different generators in muon and pion kinematics for signal events with one muon and one pion.

Table 6.1: Number of events when the total multi-ring signal sample is reweighted in one dimension for each kinematic variable separately.

	E_ν	p_μ	p_π	$\theta_{\nu\mu}$	$\theta_{\nu\pi}$	$\theta_{\mu\pi}$
NEUT	17.94	17.94	17.94	17.94	17.94	17.94
NuWRO	18.50	19.83	16.23	17.96	18.10	17.64
Genie Default	21.08	20.07	18.81	18.49	17.89	18.42
Genie Alt	21.29	20.25	18.95	18.30	17.91	18.37

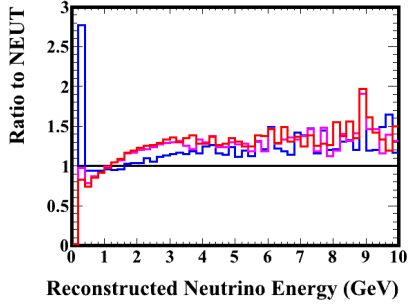
the largest variations are about 23%, and happen in neutrino energy in the GENIE models.

Multi-Dimensional Reweighting

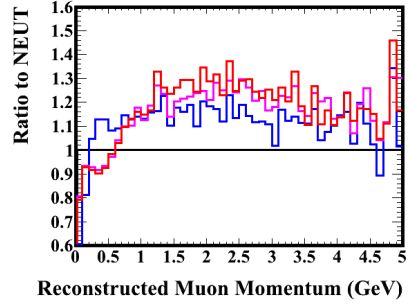
The kinematic variables presented earlier are all very correlated, so it is possible to make the size of the variations more realistic by looking at correlated weights. Weights that correlated the six kinematic variables illustrated above were generated event by event for the signal events with exactly one true muon and pion in the T2K-SK MC using a gradient boosted decision tree reweighting tool from `hep_ml` [84].

These weights were applied to the selected samples, and the size of the variations are shown for each of the six kinematic variables for the multi-ring samples and the total $\text{CC1}\pi^+$ sample in Fig. 6.3 and 6.4 respectively.

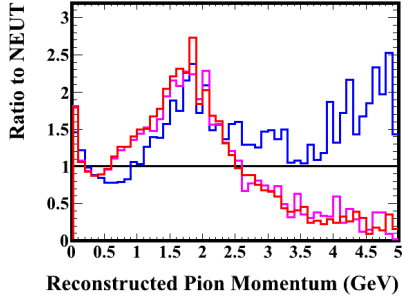
These variations across these three generators can be turned into a covariance matrix binned in three bins of reconstructed neutrino energy. These bins are defined as: 0-1 GeV, 1-2 GeV and 2-30 GeV to more finely span lower neutrino energies where there are the most events. This also more finely spans the region in which the neutrino oscillation probability is the largest, and the entire tail region at higher energies where there are few events and a small probability of oscillation can be treated together. The covariance matrix and fractional error for the sum of the multi-ring samples, and the total $\text{CC1}\pi^+$ sample are shown in Fig. 6.5. These variations look the same with and without oscillation, as well as for each sample individually so



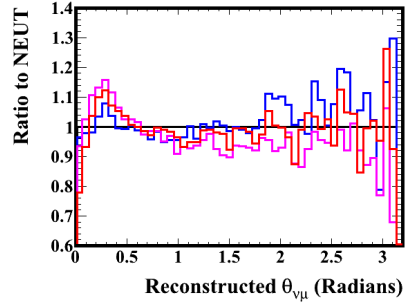
(a) Neutrino energy.



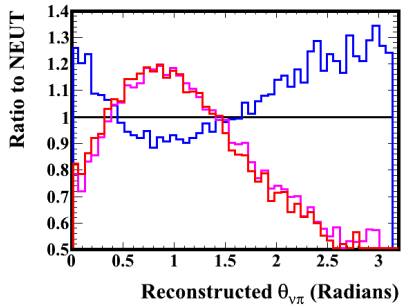
(b) Muon momentum.



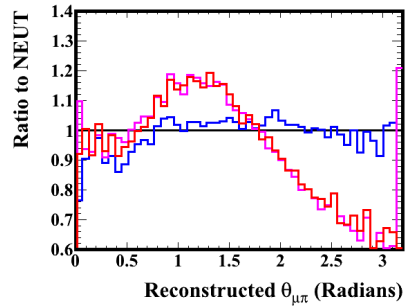
(c) Pion momentum.



(d) Angle between neutrino and muon.

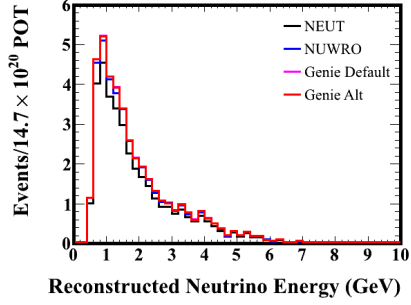


(e) Angle between neutrino and pion.

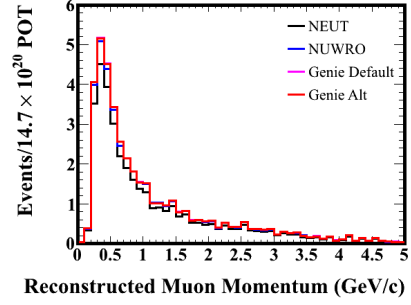


(f) Angle between muon and pion.

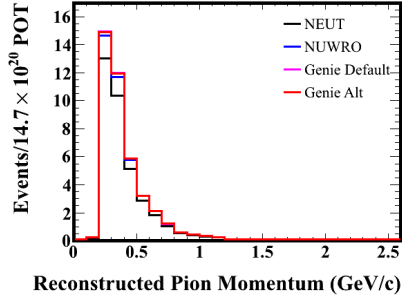
Figure 6.2: Ratio of different generators in muon and pion kinematics for signal events with one muon and one pion to the default NEUT. NEUT is black, Genie default is pink, Genie alternate is red and NUWRO is blue.



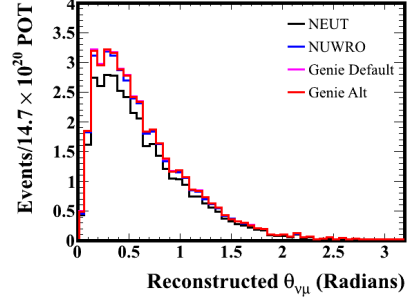
(a) Neutrino energy.



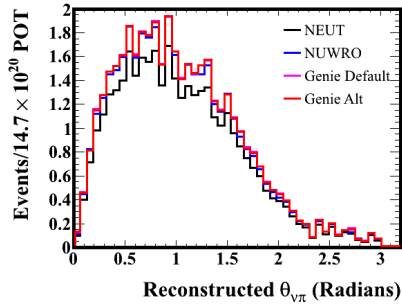
(b) Muon momentum.



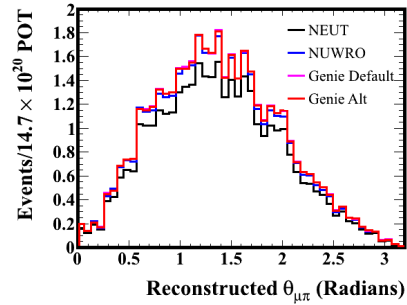
(c) Pion momentum.



(d) Angle between neutrino and muon.

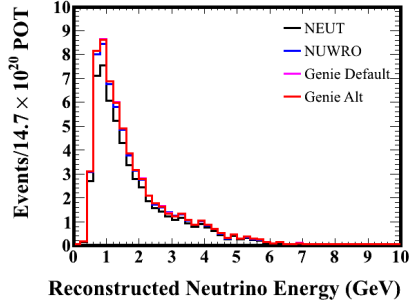


(e) Angle between neutrino and pion.

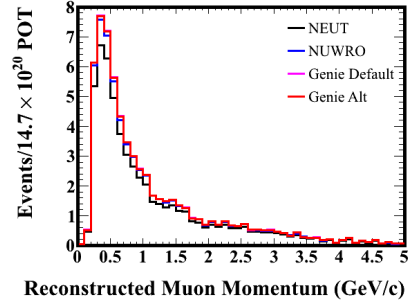


(f) Angle between muon and pion.

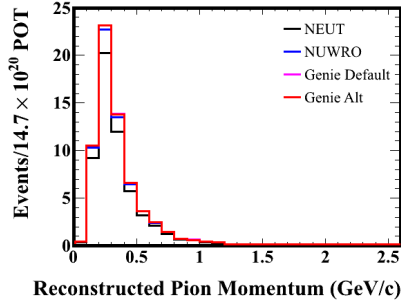
Figure 6.3: Sum of true signal events in the four multi-ring samples varied to match the kinematics of other neutrino interaction generators. NEUT is black, NUWRO is blue, Genie Default is red and Genie Alternate is pink.



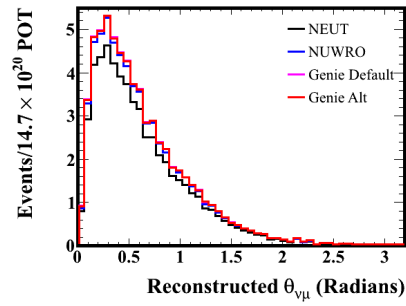
(a) Neutrino energy.



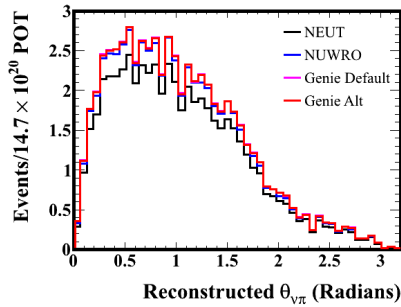
(b) Muon momentum.



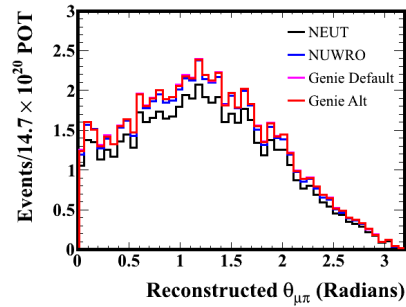
(c) Pion momentum.



(d) Angle between neutrino and muon.

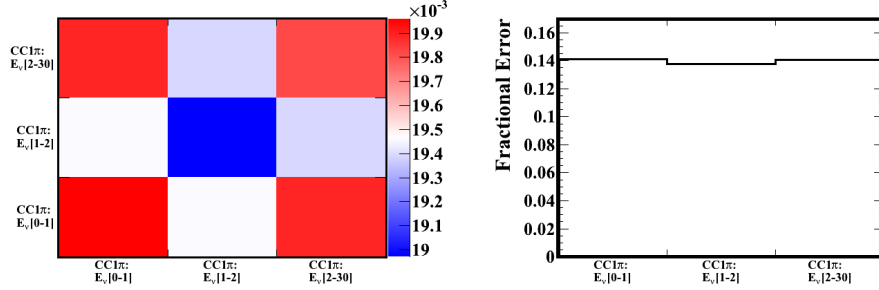


(e) Angle between neutrino and pion.



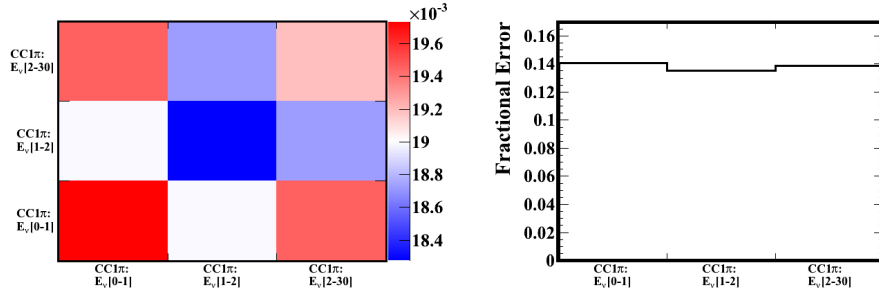
(f) Angle between muon and pion.

Figure 6.4: Sum of true signal events in the total $CC1\pi^+$ sample varied to match the kinematics of other neutrino interaction generators. NEUT is black, NUWRO is blue, Genie default is red and Genie alternate is pink.



(a) Covariance matrix for sum of four multiring samples.

(b) Fractional error for sum of four multiring samples.



(c) Covariance matrix for all samples.

(d) Covariance matrix for all samples.

Figure 6.5: Error from neutrino interaction variations.

it is possible to apply a flat 14% error to the signal due to the uncertainty of the kinematics of the neutrino interaction. The error from each of the Genie models individually is at the 15% level, and at the 13% level for NuWro.

6.1.3 Multi-Pion Variations

One of the larger backgrounds of the CC1 π^+ samples described in Chapter 5 comes from events with multiple pions, and similarly to the signal events these may change depending on the model used in the simulation. There are known issues in the implementation of the deep inelastic cross section model that is used in the current T2K-SK MC production of NEUT, and these impacted the calculation of the cross section. Now fixed, these model

changes have an effect on the total DIS cross section as well as the properties of the events, and may therefore impact the $CC1\pi^+$ samples [21]. In particular, the number of DIS and multi-pion events will affect the size of the backgrounds in the $CC1\pi^+$ samples. For example, an event with multiple π^+ exiting the nucleus may appear to have only one π^+ if only one of them is above Cherenkov threshold. The updated NEUT model is referred to as M0. Two additional models have also been added to NEUT as alternative ways to model events that produce multiple pions. One is based on deuterium bubble chamber data [85], and one is the AGKY model which is used in GENIE [86]. These will be referred to as M1 and M2 respectively.

These different models may produce different total cross sections as a function of neutrino energy, and the particle production from each of these models is different. These effects will be discussed separately below.

Reweighting in Total DIS Cross Section

The effect of the different model cross sections on the $CC1\pi^+$ samples can be studied by reweighting to the difference in the total cross section as a function of neutrino energy. This is done by taking the ratio of these different models to the default NEUT model. This is done separately depending if the target nucleon is a neutron or proton. An example of these weights is shown in Fig. 6.6 for neutrino interactions on neutrons [21].

The effect of this reweighting on the multi-ring and total $CC1\pi^+$ samples is illustrated in Fig. 6.7. As shown in Table 6.3, the largest variations in each sample are 5-8%, and typically come from M1, the model from fitting to deuterium bubble chamber data. It is also of note that changing to the updated NEUT model, M0, has very little effect on the overall sample.

Reweighting in W and Leading Pion Momentum

Changes to the multi-pion production models can also change the kinematics of the pions produced by multi-pion production neutrino interactions. These effects are studied by reweighting to the invariant hadronic mass of the system, W , and the true momentum of the most energetic charged pion

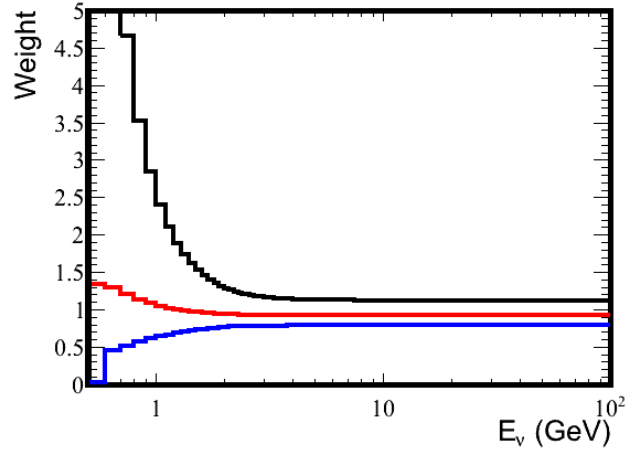


Figure 6.6: Weights applied to total multipion cross section. M0 is red, M1 is black and M2 is blue [21]. The plot is zoomed in so that the differences between M0 and M2 are visible.

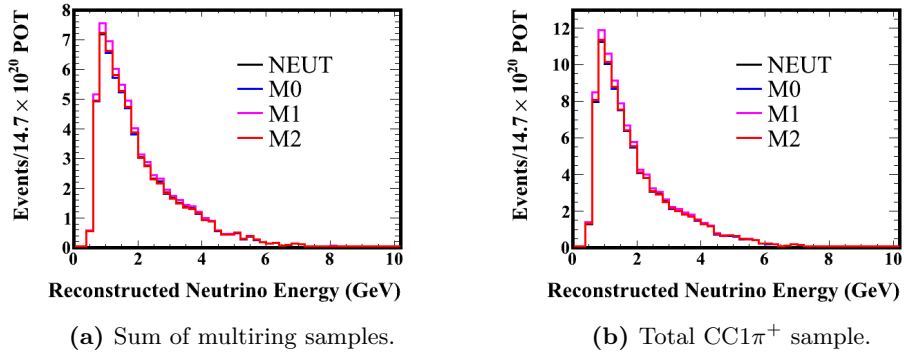


Figure 6.7: Variations in $CC1\pi^+$ samples when the different multipion cross section models are applied.

Table 6.2: Variations in the number of events as a result of changing the multi-pion DIS cross section to that of new models.

	NEUT	M0	M1	M2
1R+2de	28.79	28.87	30.46	29.08
2R+1de	26.11	26.06	26.95	26.00
2R+2de	22.16	22.20	23.55	22.59
3R+1de	7.48	7.45	7.95	7.46
3R+2de	8.18	8.17	8.87	8.34
Multi-ring sum	63.93	63.89	67.33	64.39
Total	92.72	92.75	97.79	93.46

after final state interactions. The invariant hadronic mass of the system is calculated as:

$$W^2 = (p_\nu + p_{p/n} - p_l)^2 \quad (6.1)$$

where p_ν , $p_{p/n}$, p_l are respectively the four momentum of the neutrino, the target nucleon and the outgoing lepton.

The weights were calculated by looking at the model output for W and pion momentum in each of the models described earlier (M0, M1 and M2) for interactions on water and assuming the T2K beam flux at SK. They were generated separately for proton and neutron target nucleons. An example of the weights for muon neutrino interactions for M0 on neutrons in water is shown in Fig. 6.8.

The results of applying these weights to the multi-ring $CC1\pi^+$ sample and the total $CC1\pi^+$ sample are shown in Fig. 6.9. As with the cross section variations the largest variations come from M1 deuterium fits, and these range from 3-11%. The large effect on the one ring two decay electron sample may come from the larger pion multiplicities predicted at low hadronic masses in M1. In this case there is less momentum to give to each pion individually. As there are lower momentum pions that come from these higher multiplicity events the reweighting generally results in lower momentum pions. This means that events are more likely to migrate into the one ring sample which does not require that the pions be visible. As with the cross

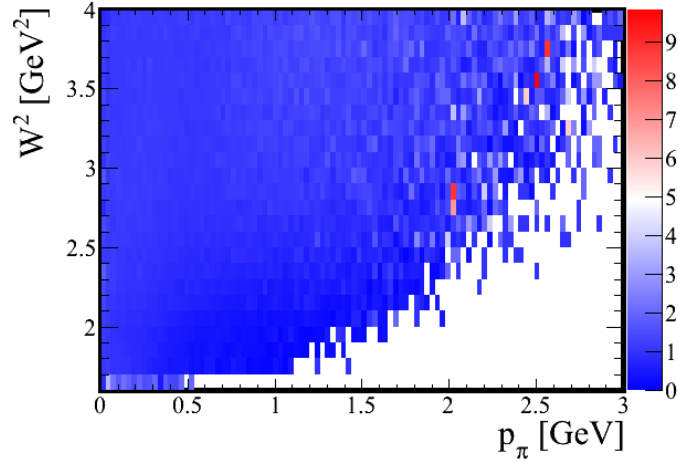
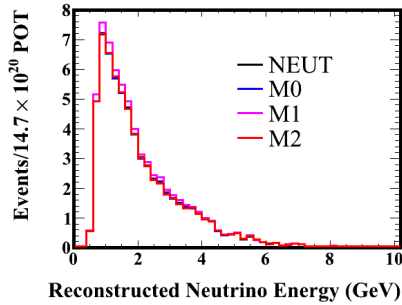
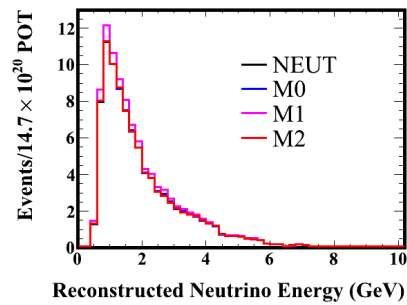


Figure 6.8: Weights applied to leading pion momentum and invariant hadronic mass for M0 [21].



(a) Sum of multiring samples.



(b) One ring and multiring samples.

Figure 6.9: Variations in $CC1\pi^+$ samples when the different multipion models are applied.

section variations, the differences between the current NEUT model and the fixed model are minor.

Table 6.3: Variations in the number of events as a result of changing the multi-pion DIS kinematics to that of new models.

	NEUT	M0	M1	M2
1R+2de	28.79	28.99	31.91	28.91
2R+1de	26.11	26.12	26.99	25.88
2R+2de	22.16	22.22	23.69	22.47
3R+1de	7.48	7.43	7.79	7.39
3R+2de	8.18	8.14	8.71	8.26
Multi-ring sum	63.93	63.91	67.17	64.00
Total	92.72	92.89	99.09	92.91

6.2 Pion Hadronic Interactions

As described in Chapter 4, fitQun relies on the hadronic interactions pions undergo in the SK water to reconstruct pions. This is explicit in the pion hypothesis which assumes that a pion may produce a thin sharp ring from absorption or scattering below Cherenkov threshold, as well as in the CC1 π^+ fitter which reconstructs the pion before and after a scatter. As there is no relatively pure sample of charged pions at SK, external measurements of pion hadronic interactions are used to evaluate the systematic errors associated with charged pion interactions in the nucleus, FSI, and SI in the SK water. The external data give us an idea of the uncertainties in the NEUT cascade model parameters, and these are then propagated through the analysis.

6.2.1 Fit to World Data

A fit to the world pion scattering data was done to tune the NEUT cascade model to match the data [22]. The result of this fit is a best fit central value for the FSI parameters, and a correlation matrix of FSI uncertainties that can be used to calculate the systematic error associated with the CC1 π^+ samples.

As described in Chapter 2, the NEUT cascade model propagates the particles produced in a neutrino interaction from their production point to the point at which they exit the nucleus, assuming a Woods-Saxon nuclear

density. The interaction probability is calculated for the particle at each step it takes towards exiting the nucleus.

The model is parameterized by the following FSI parameters which scale the interaction probabilities for the pion as it exits the nucleus:

- FEFABS: Absorption, for pions with momentum below 500 MeV/ c .
- FEFQE: Quasi-elastic scattering, for pions with momentum below 500 MeV/ c .
- FEFCX: Single charge exchange, for pions with momentum below 500 MeV/ c .
- FEFQEH: Quasi-elastic scattering, for pions with momentum above 400 MeV/ c .
- FEFCXH: Single charge exchange, for pions with momentum above 400 MeV/ c .
- FEFINEL: Hadron production in which nucleons and multiple pions are produced, for pions with momentum above 400 MeV/ c .

The momentum overlap is done to transition between low and high momentum region models in NEUT.

The fit was done to absorption, quasi-elastic scattering, charge exchange, absorption + charge exchange and reactive channel total cross section data. The reactive channel is a sum of all interactions except elastic scattering. It uses data of pion cross sections measured on carbon, oxygen, aluminum, iron, copper and lead to span light and heavy nuclei.

The best fit parameters were found by minimizing a χ^2 of the difference between the NEUT cross section predictions and the cross section measurements. The NEUT cross section was determined by performing simulations of pions at set energies from the edge of a target nucleus and using the NEUT cascade model to propagate the pion through the nucleus. The cross section could then be calculated as proportional to the ratio between the number

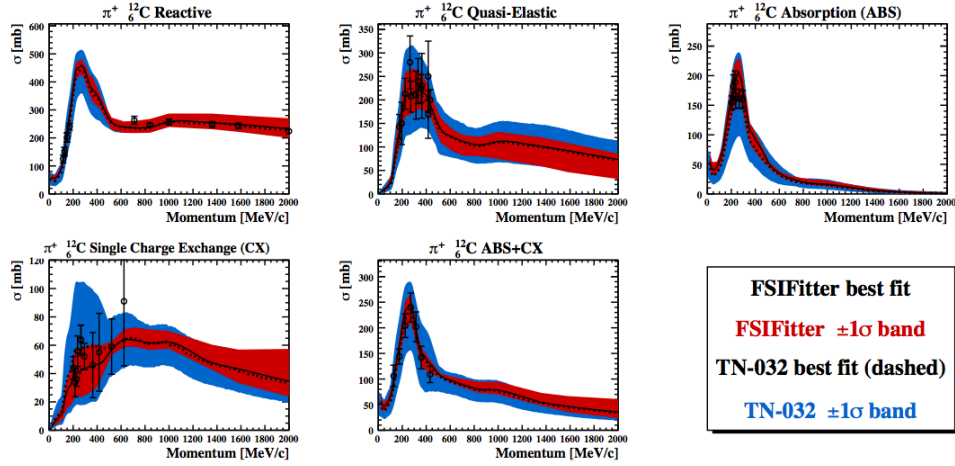


Figure 6.10: Comparison of FSI fit results to π^+ -C external cross section measurements as a function of pion momentum. FSI fit best fit is indicated by the black line, and the 1σ error band is indicated in red. The dashed line and the blue error band are the result of an earlier fit to the external pion cross section data. Figure from [22].

of events in a given interaction channel to the total number of incident pions. These were tabulated to minimize computation time during the fit, and values were interpolated to compare to the cross section measurements.

Fig. 6.10 shows the existing measurements of π^+ -carbon cross sections for each interaction type compared to the best fit and 1σ fit error band from the FSI fit.

The resulting best fit values of the FSI fit parameters and covariance matrix for all of the data sets are displayed in Table 6.4 and Fig. 6.11 respectively.

6.3 Pion FSI and SI Cross Section Variations

In order to calculate a systematic error from the effect of FSI the microscopic interaction probability for different hadronic interaction modes are varied separately. At low energy, below 500 MeV/ c in pion momentum, the interaction probabilities are varied in absorption, charge exchange and

Table 6.4: Best fit values of for the parameters in the FSI fit.

Parameter	Best fit $\pm 1\sigma$
FEFQE	1.07 ± 0.31
FEFABS	1.40 ± 0.43
FEFCX	0.70 ± 0.30
FEFINEL	1.00 ± 1.10
FEFQEH	1.82 ± 0.86
FEFCX	1.8 (Fixed)



Figure 6.11: Covariance matrix between the parameters in the FSI fit. Figure from [22].

elastic scattering. At high energy, above 500 MeV/ c in pion momentum the cross section is parameterized in terms of elastic scattering, charge exchange and other inelastic interactions including inelastic scattering and production of multiple pions.

6.3.1 Covariance Matrix Throws

Using the result of the FSI fit it is possible to use the Cholesky decomposition method to take correlated throws of possible FSI parameter set values to calculate a FSI and SI error on the $CC1\pi^+$ samples. For secondary interactions each of these variations can be turned into a constraint on the total cross section by interpolating the cross section tables as a function of FSI parameters that were used in the FSI fit while keeping the total pion

interaction cross section constant. Then just the pion interaction model within the water is rerun assuming these new secondary interaction cross section, $\sigma_i^{\text{throw}}(p_i, f_{FSI})$, which is a function of the pion momentum and the FSI parameter. This method makes it possible to calculate a weight as:

$$w_{SI} = \prod_i \frac{\sigma_i^{\text{throw}}(p_i, f_{FSI})}{\sigma_i^{\text{nom}}(p_i)} \quad (6.2)$$

The selected $\text{CC}1\pi^+$ samples are reweighted for each of the covariance matrix throws in both FSI and SI simultaneously.

1000 throws were made from the FSI covariance matrix. Results of these variations are shown in Fig. 6.12.

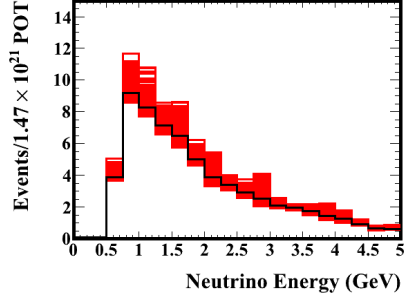
From these variations it is possible to calculate a covariance matrix for each of the samples. The covariance is calculated as:

$$V_{ij} = \frac{1}{n} \sum_{k=0}^n \frac{(N_{ik} - N_{i \text{ nom}})(N_{jk} - N_{j \text{ nom}})}{N_{i \text{ nom}} N_{j \text{ nom}}} \quad (6.3)$$

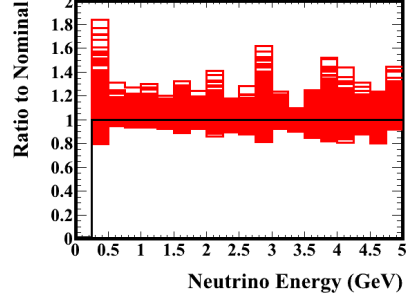
where n is the number of parameter set variations. The covariance matrix binning is defined by i and j with N_{ik} events in the i th bin for the k th variation. The nominal values are denoted with “nom”.

The covariance and fractional error for the sum of the four multi-ring samples, and all of the samples are shown in Fig. 6.13. The fractional error is defined as $\sqrt{V_{ij}}$. The covariance is binned in true neutrino mode from the interaction generator. The backgrounds: CCQE, CCothers and NC each have one bin. The signal $\text{CC}1\pi^+$ is broken into three reconstructed neutrino energy bins: 0-1 GeV, 1-2 GeV and 2-30 GeV. The largest errors are about 12% on the neutral current background events. The error on the signal is about 7% across all energy bins.

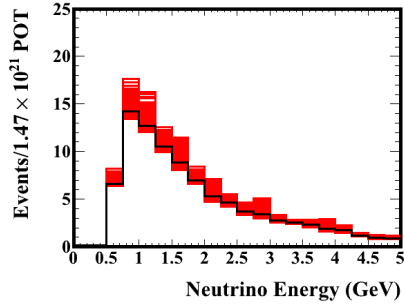
The relationship between these five samples can also be calculated as the fractional RMS between the number of events in these samples, and the correlation between the events in the samples. The fractional RMS is shown in Table 6.5, and is about the same for most of the samples. The correlation between these samples is shown in Fig. 6.14.



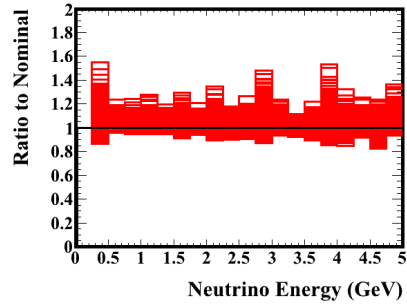
(a) Variations on the reconstructed neutrino energy distribution for the sum of the multi-ring samples.



(b) Visualization of error envelope as ratio to nominal parameter set for sum of the multiring samples.



(c) Variations on the reconstructed neutrino energy distribution for the sum of all samples.

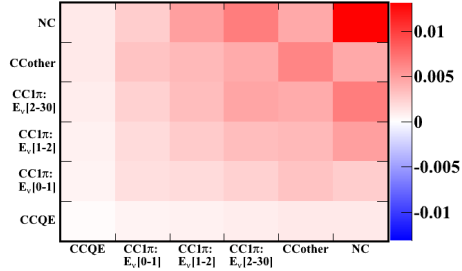


(d) Visualization of error envelope as ratio to nominal parameter set for total event sample.

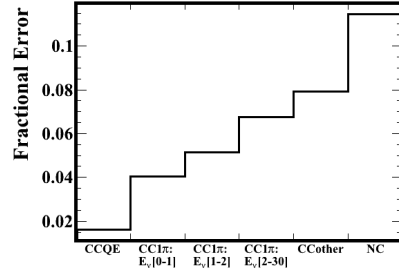
Figure 6.12: Visualization of 1000 covariance matrix throw variations of FSI and SI parameters.

Table 6.5: Fractional RMS of each of the samples from covariance matrix throw variations.

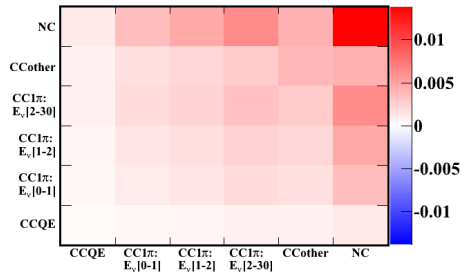
Sample	Number of Events	Fractional RMS (%)
1R+2de	29.31	3.73
2R+1de	27.51	6.07
2R+2de	22.81	8.98
3R+1de	8.14	9.02
3R+2de	8.65	11.27
MR Sum	67.11	5.54
Total	96.42	4.67



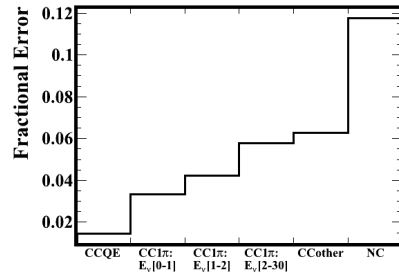
(a) Covariance matrix for sum of four multiring samples.



(b) Fractional error for sum of four multiring samples.

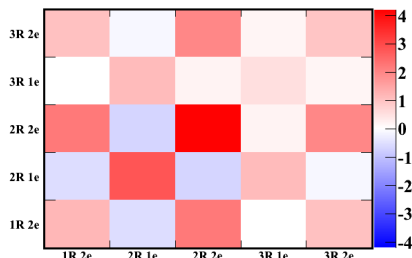


(c) Covariance matrix for all samples.

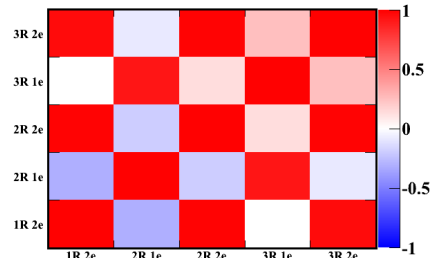


(d) Fractional error for all samples.

Figure 6.13: Error from FSI and SI covariance matrix throws.



(a) Covariance between the five $CC1\pi^+$ samples.



(b) Correlation between the five $CC1\pi^+$ samples.

Figure 6.14: Relation between the five $CC1\pi^+$ samples in terms of the FSI and SI variations.

6.4 Detector Response Uncertainties

Detector systematic errors also need to be evaluated to determine the difference between the MC detector simulation and the actual detector response. There are existing methods used to evaluate the systematic errors associated with electrons and muons at T2K using control samples. Cosmic muons are used to constrain the kinematic reconstruction of muons and electron/muon particle identification. Decay electrons are used to constrain the kinematic reconstruction of electrons and electron/muon particle identification. Atmospheric neutrinos, which produce electrons and muons in the same energy range as those produced by the T2K beam neutrinos are also used. There is no relatively pure pion only control sample of SK data, however, unlike for electrons and muons.

6.4.1 Hybrid $CC1\pi^+$ Sample

It is possible to address the detector uncertainties for charged pions through use of a hybrid sample. This is a technique that has been used to evaluate errors associated with π^0 in previous T2K analyses. In the hybrid π^0 sample one atmospheric data electron-like ring is combined with a MC photon to constrain the efficiency of the π^0 background rejection. A similar technique of combining an atmospheric neutrino data muon with a MC pion can be used to evaluate detector uncertainties for $CC1\pi^+$ events, and in particular to address the question of how charged pions are reconstructed in the presence of a muon.

Development

There are two parts to the hybrid sample, the MC and the data sample. The MC sample contains a MC muon matched with a MC pion. The data sample contains an atmospheric data muon matched with a MC pion.

The data sample is constructed by first selecting single ring muons from CCQE atmospheric neutrino interactions. Then the true muon kinematics and vertex position are extracted from each T2K $CC1\pi^+$ event in the MC. The muon momentum of the atmospheric neutrino data is matched to the

Table 6.6: Systematic error summary for sum of multi-ring samples and total CC1 π^+ samples as a fraction of the nominal number of events.

		MR Sum (%)	Total (%)
Neutrino	CC1 π^+ Signal	14	14
Interaction	DIS in E_ν	5	5
Error	DIS in $p_\pi - W$	5	6
	CCQE	2	2
	CC1 π^+ E_ν [0-1 GeV]	4	3
FSI/SI	CC1 π^+ E_ν [1-2 GeV]	5	4
Error	CC1 π^+ E_ν [2-30 GeV]	7	6
	CCother	8	6
	NC	12	12

true muon momentum of the T2K CC1 π^+ MC events. The data muon is rotated to the direction of the MC muon so that the muon kinematics match exactly. Next a charged pion ring is generated based on the true T2K-SK MC pion information with dark noise turned off. Finally the muon and the pion rings are merged.

The MC sample is generated in the same way except that the single ring muon is selected from true CCQE events in the atmospheric MC instead of from the atmospheric data.

The event reconstruction can then be run on both of these samples, and differences in the detector response between data and MC can be determined by comparing the data and MC hybrid CC1 π^+ samples. The sample construction is largely complete, but a systematic has not yet been evaluated.

6.5 Systematic Error Summary

The systematic errors associated with the neutrino interaction on water as well as those associated with pion interactions in the target nucleus and detector have been evaluated. These are summarized for the sum of the multi-ring samples and the total CC1 π^+ sample in Table 6.6.

The neutrino interaction error associated with the properties of neutrino

pion production were found to be 14% across all five $CC1\pi^+$ samples and in the sum of the multi-ring samples and the total $CC1\pi^+$ sample. This error is also constant in neutrino energy.

The systematic associated with the uncertainty in the amount of multi-pion and DIS background in the selected $CC1\pi^+$ samples was found to range from 5-8% across each of the five $CC1\pi^+$ samples and to be 5% in both the sum of the multi-ring samples and the total $CC1\pi^+$ sample when evaluated by varying the total multi-pion and DIS cross section. This error was found to range from 3-11% across the five $CC1\pi^+$ samples and to be 5% in the sum of the multi-ring samples and 6% in the total $CC1\pi^+$ sample when evaluated in W and leading pion momentum.

The error associated with pion FSI and SI was found to be 2-12% across all five $CC1\pi^+$ samples and in the sum of the multi-ring samples and the total $CC1\pi^+$ sample depending on the true neutrino interaction mode.

These neutrino interaction and pion interaction systematics will be further constrained by a fit to the T2K near detector data.

Chapter 7

Conclusions

This thesis presents a method for reconstructing and selecting charged pions at SK. It applies these methods to the $CC1\pi^+$ interaction to look for events in the T2K neutrino beam. This is the first multi-ring sample of neutrino events that will be used at T2K, and the first time that pion kinematics have been explicitly reconstructed and used in a SK analysis. The MC predicts that there will be 93 additional T2K ν_μ events with 70% purity, and these will increase the T2K ν_μ statistics by approximately 40%. These events are sensitive to oscillations as illustrated in Chapter 5, which means that they will provide an additional constraint on the neutrino oscillation parameters when included in a T2K analysis. This thesis also examines the systematic errors necessary to include this new sample in a T2K oscillation analysis. The systematic error uncertainty on the total number of predicted events is expected to be about 14 % from the neutrino-nucleus interaction and 2-12% depending on the true neutrino interaction mode and reconstructed energy for FSI and SI. These will be constrained by a fit to the T2K near detector data which may reduce these uncertainties.

There are many possible extensions to this work. The first is to complete a T2K oscillation analysis with this sample that uses the full reconstructed neutrino energy spectrum information as opposed to simply looking at the variation of the number of events as a function of the oscillation parameters as presented in Chapter 5. These samples will include information about

pions above and below Cherenkov threshold in the T2K neutrino oscillation analysis. Events may migrate between the above and below threshold samples depending on the true momentum spectrum of charged pions produced by neutrino interactions, and on the effect of FSI and SI interactions on the pion momentum spectrum. With events that are sensitive to both above and below threshold samples these migration issues will be mitigated. This is not yet the case at T2K, such as in the current T2K result which includes a one ring ν_e CC1 π^+ sample where the pion is below Cherenkov threshold and the number of measured events is much higher than the expectation [45]. This work can also be easily extended to fit for an electron and a charged pion simultaneously which will make it possible to have explicit above and below Cherenkov samples of ν_e events.

Nucleon decay is one of the only measurements that can currently constrain grand unified theories, as most of these theories include proton decay. The CC1 π^+ fitter described in Chapter 4 can also be used at SK to search for new nucleon decay modes, such as:

$$n \rightarrow e/\mu + \pi^+ \quad (7.1)$$

$$p \rightarrow \nu_e/\nu_\mu + \pi^+. \quad (7.2)$$

This fitter may make it possible to improve the SK sensitivity to these modes with an improved selection.

The scattered charged pion fitter could also be used in the future to make a NC1 π^+ measurement at SK.

These analysis techniques can also be applied to the future proposed water Cherenkov experiment Hyper-Kamiokande (HK) [49]. Identification of CC1 π^+ events will be even more important for the HK experiment if a detector is placed at a longer baseline in Korea to measure the first oscillation maximum. A smaller off axis angle, about 1.5 degrees, is chosen in this case so that the neutrino flux covers both the first and second oscillation maxima. As the off-axis angle will be such that the neutrinos will have typically larger energies than those at the Japanese HK detector the fraction of CC1 π^+ events will be higher [87].

In conclusion, the methods developed in this thesis will not only directly benefit the sensitivity of the T2K experiment, but also open the door to a new set of measurements that involve explicit identification of charged pions, which can be used by the T2K and SK collaborations as well as in future water Cherenkov experiments.

Bibliography

- [1] P. de Perio, Ph.D. thesis, University of Toronto (2014).
- [2] P. de Perio, S. Berkman, H. A. Tanaka, and S. Tobayama, T2K-TN 105: “Pion Hadronic Secondary Interactions in Super-Kamiokande” (2012).
- [3] R. B. Patterson, E. M. Laird, Y. Liu, P. D. Meyers, I. Stancu, and H. A. Tanaka, Nuclear Inst. and Methods in Physics Research A (2009).
- [4] S. Berkman, P. de Perio, A. Konaka, A. Missert, H. Tanaka, S. Tobayama, M. J. Wilking, and E. D. Zimmerman, T2K-TN 146: “fitQun: A New Reconstruction Algorithm for Super-K” (2013).
- [5] A. A. Aguilar-Arevalo et al. (MiniBooNE), Phys. Rev. **D83**, 052007 (2011).
- [6] K. Abe et al. (T2K), Phys. Rev. **D88**, 032002 (2013).
- [7] S. Berkman, H. A. Tanaka, S. Tobayama, R. Tacik, P. de Perio, A. Konaka, and M. J. Wilking, T2K-TN 153: “Data/Monte Carlo Simulation Comparisons with fitQun v3r1” (2013).
- [8] E. S. P. Guerra, Ph.D. thesis, York University (2018).
- [9] G. Yang, S. Mine, T. Mueller, and M. Wilking, T2K-TN342: “Construction of new hybrid CC1 π^+ sample for the SK detector error estimation” (2017).
- [10] C. Patrignani et al. (Particle Data Group), Chin. Phys. **C40**, 100001 (2016), and 2017 update.
- [11] T. Araki et al. (KamLAND), Phys. Rev. Lett. **94**, 081801 (2005).

- [12] A. Gando et al. (KamLAND), Phys. Rev. **D83**, 052002 (2011).
- [13] K. Abe et al. (T2K), Phys. Rev. Lett. **118**, 151801 (2017).
- [14] P. Adamson et al. (NOvA), Phys. Rev. Lett. **118**, 151802 (2017).
- [15] K. Abe et al. (Super-Kamiokande), arXiv:hep-ex/1710.09126 (2017).
- [16] P. Adamson et al. (MINOS), Phys. Rev. Lett. **112**, 191801 (2014).
- [17] M. G. Aartsen et al., Nucl. Phys. **B908**, 161 (2016).
- [18] K. Abe et al. (T2K), Nucl. Instrum. Meth. **A659**, 106 (2011).
- [19] K. Abe et al., Nucl. Instrum. Meth. **A737**, 253 (2014).
- [20] J. A. Formaggio and G. P. Zeller, Rev. Mod. Phys. **84**, 1307 (2012).
- [21] S. Bolognesi, C. Bronner, A. Cudd, M. Dunkman, et al., T2K-TN 315: “NIWG model and uncertainties for 2017 oscillation analysis” (2017).
- [22] T. Feusels, A. Fiorentini, E. S. P. Guerra, C. Wilkinson, and M. Yu, T2K-TN 325: “Tuning of the NEUT Cascade Model using π^\pm -A Scattering External Data to Improve Final State Interaction and Secondary Interaction Systematic Uncertainties” (2017).
- [23] D. Griffiths, *Introduction to Elementary Particles* (Wiley VCH Verlag GmbH, 2008), ISBN 3527406018.
- [24] J. Chadwick, Verh. Phys. Gesell. **16**, 383 (1914).
- [25] W. Pauli, Phys. Today **31N9**, 27 (1978), letter sent December 4, 1930. Reprinted translation into English.
- [26] E. Fermi, Z. Phys. **88**, 161 (1934).
- [27] C. L. Cowan, F. Reines, F. B. Harrison, H. W. Kruse, and A. D. McGuire, Science **124**, 103 (1956).
- [28] G. Danby, J. M. Gaillard, K. A. Goulianos, L. M. Lederman, N. B. Mistry, M. Schwartz, and J. Steinberger, Phys. Rev. Lett. **9**, 36 (1962).
- [29] K. Kodama et al. (DONUT), Phys. Lett. **B504**, 218 (2001).
- [30] R. Davis, D. S. Harmer, and K. C. Hoffman, Phys. Rev. Lett. **20**, 1205 (1968).

- [31] W. Hampel et al. (GALLEX), Phys. Lett. **B447**, 127 (1999).
- [32] J. N. Abdurashitov et al. (SAGE), J. Exp. Theor. Phys. **95**, 181 (2002), [Zh. Eksp. Teor. Fiz.122,211(2002)].
- [33] K. S. Hirata et al. (Kamiokande-II), Phys. Rev. Lett. **63**, 16 (1989).
- [34] K. S. Hirata et al. (Kamiokande-II), Phys. Rev. **D44**, 2241 (1991), [Erratum: Phys. Rev.D45,2170(1992)].
- [35] Q. R. Ahmad et al. (SNO), Phys. Rev. Lett. **89**, 011301 (2002).
- [36] Y. Fukuda et al. (Super-Kamiokande), Phys. Rev. Lett. **81**, 1562 (1998).
- [37] L. Wolfenstein, Phys. Rev. **D17**, 2369 (1978).
- [38] S. P. Mikheev and A. Yu. Smirnov, Sov. J. Nucl. Phys. **42**, 913 (1985), [Yad. Fiz.42,1441(1985)].
- [39] B. Aharmim et al. (SNO), Phys. Rev. **C88**, 025501 (2013).
- [40] K. Abe et al. (Super-Kamiokande), Phys. Rev. **D94**, 052010 (2016).
- [41] G. Bellini et al. (Borexino), Phys. Rev. **D89**, 112007 (2014).
- [42] F. P. An et al. (Daya Bay), Phys. Rev. Lett. **115**, 111802 (2015).
- [43] Y. Abe et al. (Double Chooz), JHEP **10**, 086 (2014), [Erratum: JHEP02,074(2015)].
- [44] J. H. Choi et al. (RENO), Phys. Rev. Lett. **116**, 211801 (2016).
- [45] M. Hartz, KEK Colloquium: “T2K Neutrino Oscillation Results with Data up to 2017 Summer” (2017), URL <https://kds.kek.jp/indico/event/25337/>[Accessed:01/22/2018].
- [46] K. Abe et al., arXiv:1609.04111 [hep-ex] (2016).
- [47] R. Acciarri et al. (DUNE), arXiv:1601.05471 [physics.ins-det] (2016).
- [48] R. Acciarri et al. (DUNE), arXiv:1601.05823 [physics.ins-det] (2016).
- [49] K. Abe et al., arXiv:1109.3262 [hep-ex] (2011).
- [50] P. A. R. Ade et al. (Planck), Astron. Astrophys. **594**, A13 (2016).

- [51] B. G. Robert N. Cahn, Gerson (University of California, *The Experimental Foundations of Particle Physics* (Cambridge University Press, 2009), 2nd ed., ISBN 0521521475).
- [52] D. Beavis et al., techreport BNL-52459, Brookhaven National Lab, NY (1995).
- [53] K. Abe et al. (T2K), Nucl. Instrum. Meth. **A694**, 211 (2012).
- [54] P. A. Amaudruz et al. (T2K ND280 FGD), Nucl. Instrum. Meth. **A696**, 1 (2012).
- [55] N. Abgrall et al. (T2K ND280 TPC), Nucl. Instrum. Meth. **A637**, 25 (2011).
- [56] S. Assylbekov et al., Nucl. Instrum. Meth. **A686**, 48 (2012).
- [57] D. Allan et al. (T2K UK), JINST **8**, P10019 (2013).
- [58] S. Aoki et al., Nucl. Instrum. Meth. **A698**, 135 (2013).
- [59] Y. Fukuda et al. (Super-Kamiokande), Nucl. Instrum. Meth. **A501**, 418 (2003).
- [60] P. A. Cherenkov, Doklady Akad. Nauk SSSR **2**, 451 (1934).
- [61] J. D. Jackson, *Classical Electrodynamics* (Wiley, 2nd Edition, 1975).
- [62] A. Ferrari, P. R. Sala, A. Fassò, and J. Ranft, *FLUKA: A Multi-Particle Transport Code (Program Version 2005)*, CERN Yellow Reports: Monographs (CERN, Geneva, 2005).
- [63] R. Brun, F. Bruyant, M. Maire, A. C. McPherson, and P. Zancarini, Tech. Rep., CERN (1987).
- [64] N. Abgrall et al. (NA61/SHINE), Eur. Phys. J. **C76**, 84 (2016).
- [65] C. Zeitnitz and T. A. Gabriel, Nucl. Instrum. Meth. **A349**, 106 (1994).
- [66] K. Abe et al. (T2K), Phys. Rev. **D87**, 012001 (2013), [Addendum: Phys. Rev.D87,no.1,019902(2013)].
- [67] Y. Hayato, Nucl. Phys. Proc. Suppl. **112**, 171 (2002).
- [68] C. Andreopoulos et al., arXiv:1510.05494 [hep-ph] (2015).

- [69] T. Golan, C. Juszczak, and J. T. Sobczyk, Phys. Rev. C **86**, 015505 (2012).
- [70] C. H. Llewellyn Smith, Phys. Rept. **3**, 261 (1972).
- [71] J. Nieves, I. R. Simo, and M. J. V. Vacas, Phys. Rev. C **83**, 045501 (2011).
- [72] D. Rein and L. M. Sehgal, Annals Phys. **133**, 79 (1981).
- [73] Y. Hayato, Acta Phys. Polon. **B40**, 2477 (2009).
- [74] D. Rein and L. M. Sehgal, Nucl. Phys. **B223**, 29 (1983).
- [75] T. Sjostrand, Comput. Phys. Commun. **82**, 74 (1994).
- [76] L. L. Salcedo, E. Oset, M. J. Vicente-Vacas, and C. Garcia-Recio, Nucl. Phys. **A484**, 557 (1988).
- [77] S. Bhadra et al. (NuPRISM), “Proposal for the NuPRISM Experiment in the J-PARC Neutrino Beamline” (2016), URL http://j-parc.jp/researcher/Hadron/en/pac_1607/pdf/P61_2016-17.pdf[Accessed:04/12/2018].
- [78] F. James, CERN-D506 (1994).
- [79] D. E. Groom, N. V. Mokhov, and S. I. Striganov, Atom. Data Nucl. Data Tabl. **78**, 183 (2001).
- [80] X. Li and M. Wilking, T2K-TN 319: “fitQun Event Selection Optimization” (2017).
- [81] K. Abe et al. (T2K), Phys. Rev. **D96**, 092006 (2017).
- [82] M. Alam et al., arXiv:1512.06882 [hep-ph] (2015).
- [83] J. Zmuda, K. M. Graczyk, C. Juszczak, and J. T. Sobczyk, Acta Phys. Polon. **B46**, 2329 (2015).
- [84] A. Rogozhnikov and contributors, URL https://github.com/arogozhnikov/hep_ml[Accessed:01/22/2018].
- [85] T. Yang, C. Andreopoulos, H. Gallagher, K. Hoffmann, and P. Kehayias, Eur.Phys.J.C **63:1-10,2009** (2009).
- [86] A. Cooper-Sarkar, P. Mertsch, and S. Sarkar, JHEP **08**, 042 (2011).

- [87] K. Abe et al. (Hyper-Kamiokande proto-Collaboration),
arXiv:1611.06118[hep-ex] (2016).